# A Model for Gas Dynamics and Chemical Evolution of the Fornax Dwarf Spheroidal Galaxy

**A THESIS**

**SUBMITTED TO THE FACULTY OF THE GRADUATE SCHOOL**

**OF THE UNIVERSITY OF MINNESOTA**

**BY**

**Zhen Yuan**

**IN PARTIAL FULFILLMENT OF THE REQUIREMENTS**

**FOR THE DEGREE OF**

**Doctor of Philosophy**

**Professor Yong-Zhong Qian, Advisor**

**September, 2015**

# Acknowledgements

I would like to express my sincere gratitude to many people who helped and supported me during my graduate study.

Firstly, I would like to thank my advisor Prof. Yong-Zhong Qian for all the patience and encouragement he gave me. He inspired me to build my own road in this research field, and guided me through all the difficulties on the way. I learned a lot from his method of understanding physics and the comprehensive world.

I am very grateful to Dr. Thomas deBoer, Prof. Evan Kirby and Dr. Andreas Koch, for providing the data on dwarf spheroidal galaxies and all the insights they gave from observational aspect. I would like to thank Prof. Alexander Heger and Conrad Chan for help with the quadratic-spline fit and providing the supernovae yield table. My sincere thanks also goes to my collaborators, Prof. Jing-Yi Peng, Dr. Dong-Hai Zhao and Zhao-Zhou Li, who shared me with the firsthand experience in the cosmological simulations and provided me with the dark matter halo model in my thesis work.

I am very appreciated to belong to the nuclear astrophysics group in University of Minnesota. I would like to thank Dr. Projjwal Banerjee, Dr. Meng-Ru Wu, Cheng-Hsien Li, and Zhu Li for discussing various topics in physics. I would also like to thank Prof. Joe Kapusta, Prof. Keith Olive, and Prof. Evan Skillman for being my committee members.

I would like to thank to Boyi Yang, for all his love and support. I would give my deepest gratitude to all of my friends, who have made my life in Minnesota memorable.

Lastly I would like to thank my parents for all the spiritual and physical support they gave me during these years.

# Dedication

To my parents Yu-Lan Yuan and Jia-Hong Chen

## Abstract

We present an empirical model for the halo evolution, global gas dynamics and chemical evolution of Fornax, the brightest Milky Way (MW) dwarf spheroidal galaxy (dSph). Assuming a global star formation rate $\psi(t) = \lambda_*(t)[M_g(t)/M_\odot]^\alpha$ consistent with observations of star formation in nearby galaxies and using the data on Fornax's $\psi(t)$, we derive the evolution of the total mass $M_g(t)$ and the rate $\Delta F(t)$ of net gas flow for cold gas in a growing star-forming disk with a time variable $\lambda_*(t)$. We identify the onset of the transition in $\Delta F(t)$ from a net inflow to a net outflow as the time $t_{\rm sat}$ at which the Fornax halo became an MW satellite and estimate the evolution of its total mass $M_h(t)$ at $t \leq t_{\rm sat}$ using the median halo growth history in the ΛCDM cosmology and its present mass within the half-light radius derived from observations. We find that the Fornax halo grew to $M_h(t_{\rm sat}) \approx 1.8 \times 10^9\, M_\odot$ at $t_{\rm sat} \approx 4.8$ Gyr and that its subsequent global gas dynamics was dominated by ram-pressure stripping and tidal interaction with the MW. Then we build a chemical evolution model on a 2-D mass grid, using supernovae as the enrichment source of the gaseous system. We find that the key parameter of controlling the element abundances pattern is the supernovae mixing mass. It is set differently between two types of supernovae and between two phases, before and after $t_{\rm sat}$ in our model. The choice is determined based on the supernovae remnant evolution as well as the global gas dynamics. We also find the metal loss in the outflow dominated phase ($t > t_{\rm sat}$) is severe, which is empirically implemented in our model. The data generated from the standard case can explain the observational data very well, e.g., abundance ratio of $\alpha$ element to Fe as a function of metallicity [$\alpha$/Fe] vs. [Fe/H], metallicity evolution as a function of time [E/H] vs. t and metallicity distribution function (MDF) for Mg, Ca and Fe.

# Contents

# List of Figures

# Chapter 1

# Introduction

In the recent decade, equipped with large telescopes and supercomputers, we have stepped into a brand new era of galaxy formation and evolution studies. At the same time, hallmarks on stellar nucleosysnthesis has been well established in the past few years. And one of the linkages between the galactic and stellar scale physics is the chemical abundance information of stars. Served as archaeological fossils, stars record the galactic environmental information of their birth sites. Therefore, by studying the chemical information of stars with different ages in a particular galaxy would give you some hints of its formation and evolution history. Here, we choose to look into nearby dwarf spheroidal galaxies (dSphs).

Dwarf galaxies are believed to be the building blocks of larger galaxies, like spirals and ellipticals based on the hierarchical structure formation theory. Therefore, understanding how dwarf galaxies evolve is crucial to unraveling the formation and evolution of bigger galaxies such as the Milky Way. And unlike large galaxies, there is no major merger event happened on dwarfs so far. Thus, they almost keep intact from outside throughout their histories, which makes them the perfect laboratory to track all kinds of physical mechanism in galactic scales. Whereas in large galaxies, all these information has been washed out during frequent merger events.

Extensive studies have been done on local dSphs both from observations and simulations. Star formation histories (SFHs) have been derived from comparison of observed and synthetic color-magnitude diagrams. Individual stars have been resolved by spectroscopy with large-aperture telescopes. Deep photometric and high-resolution spectroscopic studies have produced abundances of e.g., Mg, Si, Ca, Ti, and Fe along with ages for individual stars in nearby dSphs. In the meantime, there has been remarkable progress in simulations of galaxy formation, with more and more sophisticated numerical implementation to follow dark matter and baryons simultaneously. A large amount of effort has been directed towards incorporating star formation and various channels of its feedback. With all the new data and tools, we are nonetheless still at the first stage to understand chemical evolution of dwarf galaxies.

We use the brightest satellite galaxy, Fornax dSph as our target system. In order to construct a realistic chemical evolution history, we need to understand its galaxy formation and evolution history using simulatonal tools, as we mentioned above. Specifically, an in-depth study of the halo evolution and the associated gas dynamics of a dSph would require simulations that incorporate hierarchical structure formation in the $\Lambda$CDM cosmology and treat a wide range of physical processes, such as gas accretion by the hosting halo before and after reionization of the universe, cooling and condensation of gas to form stars, conversion of cold into hot gas by radiation and supernova (SN) explosion, and gas expulsion from the halo. Our approach here is empirical and phenomenological. We infer the gas dynamics directly from the observed SFH of Fornax.

Based on the gas dynamics of Fornax, We build its chemical evolution model and compare with the elemental abundance data. Observations strongly indicate that the chemical enrichment in Fornax dSphs remains inhomogeneous until the end of its SFH despite of the small size. Using supernova nucleosyntheis yields as input, we numerically simulated stochastic and inhomogeneous mixing of newly-synthesized elements by supernovae on a 2-D disk system. By comparing with the abundance pattern in Fornax, we found that the mixing depends on large-scale gas flows, the clumpy structure of the

ISM, and the differences between environments of core-collapse and Type Ia supernovae.

In this thesis, We will discuss how we achieve all above goals step by step. This paper is organized as follows:

- Chapter 2, We gives a brief review on theoretical and empirical SFLs and then discuss the SFL in Fornax dSph.
- Chapter 3, Based on the SFL from §2, we infer the gas mass and gas flow from SFH in Fornax dSph.
- Chapter 4, We find a candidate halo model for Fornax dSph, according to its gas dynamics from §3.
- Chapter 5, We describe the global gas dynamics in the satellite phase of Fornax.
- Chapter 6, We explore SNe yields table and illustrate SNe remnants evolution.
- Chapter 7, We describe how the chemical evolution model of Fornax dSph is constrcuted.
- Chapter 8, Our conclusion is given .

# Chapter 2

# Star Formation Laws

The central role to our empirical approach of constructing the gas dynamics for dSphs is the SFL relating the SFR to gas properties. Therefore, we start with a brief discussion of theoretical and empirical SFLs (see e.g., [1, 2] for comprehensive reviews).

## 2.1 Theoretical SFLs

Star formation is most directly associated with molecular gas from observations [3] [4] using variety of molecular tracers. Theoretically, there are two approaches to interpret this relation [5]. One is called the Schmidt law picture. For a cloud with a total mass $M_{\rm mol}$ of molecular gas (predominantly consisting of $H_2$ molecules and the associated He atoms), a theoretical estimate of the SFR (e.g., [6]) is

$$\frac{dM_*}{dt} = \epsilon_{\rm ff} \frac{M_{\rm mol}}{t_{\rm ff}}, \tag{2.1}$$

where $M_*$ is the mass of stars formed,

$$t_{\rm ff} \equiv \sqrt{\frac{3\pi}{32 G \rho_{\rm mol}}} \tag{2.2}$$

is the free-fall time (see derivation in Appendix C) at the density $\rho_{\rm mol}$ of the molecular gas, $G$ is the gravitational constant, and $\epsilon_{\rm ff}$ is the fraction of the molecular gas turned

into stars during one free-fall time. From observations, we can only directly measure the surface SFR $\Sigma_{\rm SFR}$ as well as surface gas density $\Sigma_g$. In a disk-like galaxy with scale-hight $\mathcal{H}$, $\rho_{\rm g} \sim \Sigma_{\rm g}/\mathcal{H}$, we can rewrite Eq. (2.1) as

$$\Sigma_{\rm SFR} = \epsilon_{\rm ff}\sqrt{\frac{32G}{3\pi\mathcal{H}}}(f_{\rm H_2}\Sigma_g)^{1.5}, \tag{2.3}$$

where $f_{\rm H_2}$ is the fraction of H mass in $H_2$ molecules. In Schmidt law picture, high SFRs are purely the consequence of high gas densities of SF regions. In an alternative picture we discuss below, SFR linearly scales with the molecular gas density and the inverse of dynamic time scale.

$$\Sigma_{\rm SFR} = \epsilon_{\rm ff}\frac{f_{\rm H_2}\Sigma_g}{t_{\rm dyn}}. \tag{2.4}$$

Under this scenario, high SFRs are the results of the short dynamical timescales, which reflect the small physical scales of the SF regions. Both approaches offer equally valid parametrization of SFR from different studies shown in the next section. And $\epsilon_{\rm ff}$ is universally close to $10^{-2}$ from different observation studies, which can be understood by the analytic turbulence model proposed by [7] and the simulations of star forming galaxies considering stellar feedbacks §§2.4.

## 2.2 Empirical SFLs

Both Eqs. (2.3) and (2.4) can be applied to individual star-forming regions and in the disk-averaged form, to individual galaxies (see review by [2]). For illustration, we compare them with two observational results below.

Based on the observations of 61 normal spiral galaxies and 36 starburst galaxies, there is a tight correlation between $\Sigma_{\rm SFR}$ and $\Sigma_g$ found by [5], both of which are averaged over the disk of an individual galaxy. The data analyzed is obtained form the measurements of $H_\alpha$, $H_{\rm I}$ far-inferred and CO distributions. Here, we briefly summarize the physical mechanisms of these measurements [1].

H$\alpha$ emission line is emitted when hydrogen electron transit from high to low excited energy state n=3→2. Since the energy required to ionize H atom is almost the same as the energy to excite the atom n=1→3. Ionized H would recombine and decay to n=2 half of the time, which emits H$\alpha$ line. Thus H$\alpha$ line is the direct indicator of ionized H atoms. In a star forming region, massive yong stars are surrounded by the ionized gas. These lines can be served as the tracer of stars with masses greater than $\sim$15 $M_\odot$, with the peak contribution from stars in the range 30$\sim$40 $M_\odot$. Therefore H$\alpha$ luminosity is a nearly instantaneous measurement of the SFR. The major pitfall of H$\alpha$ measurement is dust attenuation, especially in high gas density galaxies. In those galaxies, the starburst ones can be measured using FIR, since the IR luminosity is also dominated by the young stars [1].

The gas tracer in this study is the commonly used 21 cm line for atomic $H_I$ and CO emission line for molecular H. 21 cm line comes from the splitting of hyperfine levels of hydrogen in the 1s ground state, which is due to the interaction between electron spin and proton spin. As for the molecular form of hydrogen, people usually can not detect $H_2$ directly. Because of the low mass of $H_2$, the rotational transitions requires quite high temperatures to excite, which makes the detection of $H_2$ impossible. Instead, CO is the most commonly used tracer to measure the mass of cloud. With some conversion factor, which differs as a factor of 3 in MW, we are able to estimate the number density of $H_2$ [1].

The observational results from [5] are straightforward, shown as the global SFL

$$\frac{\Sigma_{\rm SFR}}{M_\odot\ {\rm yr}^{-1}\ {\rm kpc}^{-2}} = (2.5 \pm 0.7) \times 10^{-4} \left( \frac{\Sigma_g}{M_\odot\ {\rm pc}^{-2}} \right)^{1.4\pm0.15}, \tag{2.5}$$

where $\Sigma_g$ ranges from $\sim$ 10 to $10^4$ $M_\odot$ pc$^{-2}$ for the galaxies used. Following the alternative prescription, they also got equally tight relationship between $\Sigma_{\rm SFR}$ and $\Sigma_{\rm gas}/\tau_{\rm dyn}$.

$$\frac{\Sigma_{\rm SFR}}{M_\odot\ {\rm yr}^{-1}\ {\rm kpc}^{-2}} = 1.7 \times 10^{-2} \left( \frac{\Sigma_g}{M_\odot\ {\rm pc}^{-2}} \right) \left( \frac{\rm yr}{\tau_{\rm dyn}} \right), \tag{2.6}$$

where $\tau_{\rm dyn}$ is the dynamic timescale taken to be the orbit time at half of the outer radius

of the star-forming disk, and ranges from $\sim 10^7$ to $\sim 10^8$ yr.

A more recent observational study with better resolution focusing on nearby galaxies give us similar results [8]. From their analysis, the estimation of $\Sigma_{\rm HI}$ uses the high-resolution, high-sensitivity $H_I$ data from THINGS. The derivation of $\Sigma_{\rm H2}$ come from two sources. HERACLES and BIMA SONG produces maps of CO J=2→1 and CO J=1→0 transition in defferent $\Sigma_{\rm H2}$ regimes, respectively. $\Sigma_{\rm SFR}$ is estimated by combining FUV data from NGS and 24 $\mu$m data from SINGS.

Based on observations of seven nearby spiral galaxies resolved to 750 pc, they found that over the range of $\Sigma_{\rm H} \sim 1$–$10^2\, M_\odot$ pc$^{-2}$ for the net surface mass density of H atoms and $H_2$ molecules in star-forming regions, $\Sigma_{\rm SFR}$ can be described by [8]

$$\frac{\Sigma_{\rm SFR}}{M_\odot\ {\rm yr}^{-1}\ {\rm kpc}^{-2}} = 10^{-2.39\pm0.28} \left( \frac{\Sigma_{\rm H}}{10\, M_\odot\ {\rm pc}^{-2}} \right)^{1.85\pm0.70}. \tag{2.7}$$

In the alternative picture,

$$\frac{\Sigma_{\rm SFR}}{M_\odot\ {\rm yr}^{-1}\ {\rm kpc}^{-2}} = 10^{-2.1\pm0.2} \left( \frac{\Sigma_{\rm H_2}}{10\, M_\odot\ {\rm pc}^{-2}} \right)^{1.0\pm0.2}, \tag{2.8}$$

The above SFL covers $\Sigma_{\rm H_2} \sim 3$–$50\, M_\odot$ pc$^{-2}$. Both parametrization methods shown as Eq. (2.5) and Eq. (2.6) offer us tools to describe SFR without the first principle calculation of star formation. Here we show how the empirical relation correlates to the theoreticle formulation. Consider the limit of $\Sigma_g \gtrsim 10^2\, M_\odot$ pc$^{-2}$, for which gas predominantly consists of $H_2$ molecules [7] and Eq. (2.3) can be applied to give

$$\frac{\Sigma_{\rm SFR}}{M_\odot\ {\rm yr}^{-1}\ {\rm kpc}^{-2}} \sim 1.2 \times 10^{-4} \left( \frac{\epsilon_{\rm ff}}{10^{-2}} \right) \left( \frac{100\ {\rm pc}}{\mathcal{H}} \right)^{0.5} \left( \frac{\Sigma_g}{M_\odot\ {\rm pc}^{-2}} \right)^{1.5}, \tag{2.9}$$

which is in good agreement with Eq. (2.5) for $\epsilon_{\rm ff} \sim 10^{-2}$ and disk scale-heights of $\mathcal{H} \sim 100$ pc. A similar argument was used by [5] to explain qualitatively the power-law form of Eq. (2.5).

## 2.3 SFL in Fornax dSph

As our goal is to gain some understanding of the overall picture for halo evolution and gas dynamics of Fornax, we are interested in the relation of its global SFR to its properties on the galactic scale. While we recognize the important role of molecular gas in star formation, our simple approach here will focus on the net cold gas in atomic and molecular forms, which dominates the total gas mass in the star-forming disk. [8] found that over the range of $\Sigma_{\rm H} \sim 1$–$10^2\ M_\odot\ {\rm pc}^{-2}$ for the net surface mass density of H atoms and $H_2$ molecules in star-forming regions, $\Sigma_{\rm SFR}$ can be described by 2.7. In addition, the Kennicutt-Schmidt law in Eq. (2.5) describes the global $\Sigma_{\rm SFR}$ for individual galaxies with $\Sigma_g \sim 10$–$10^4\ M_\odot\ {\rm pc}^{-2}$. This law and Eq. (2.7) cover a common range of $\Sigma_g \sim 10$–$10^2\ M_\odot\ {\rm pc}^{-2}$. Within their uncertainties, they are also in agreement over this range. Guided by the above empirical results, we assume that the global SFR $\psi(t)$ in Fornax is related to the total mass $M_g(t)$ of gas in its star-forming disk as

$$\psi(t) = \frac{{\rm d}M_*}{{\rm d}t} = \lambda_* \left[\frac{M_g(t)}{M_\odot}\right]^\alpha \tag{2.10}$$

where $\lambda_*$ is a rate constant. The underlying assumption is that the effective area $A_{\rm disc}$ of Fornax's star-forming disk stayed approximately constant over its SFH. I will consider the growth of disk in §4. Here, for the simplest case, I can interpret Eq. (2.10) in terms of the empirical SFLs in Eqs. (2.5) and (2.7) as

$$\frac{\Sigma_{\rm SFR}(t)}{M_\odot\ {\rm yr}^{-1}\ {\rm kpc}^{-2}} = \frac{\lambda_*}{10^{1-8\alpha}\, M_\odot\ {\rm yr}^{-1}} \left(\frac{A_{\rm disc}}{10\ {\rm kpc}^2}\right)^{\alpha-1} \left[\frac{\Sigma_g(t)}{10\, M_\odot\ {\rm pc}^{-2}}\right]^\alpha . \tag{2.11}$$

The above equation has the same form as Eqs. (2.5) and (2.7), which allows us to estimate $\alpha$ and $\lambda_*$. We will examine cases of $\alpha = 1.5$ and 2, which closely represent Eqs. (2.5) and (2.7), respectively. As the majority of stars in the present-day Fornax are distributed within a region of $r_* \sim 2$ kpc in radius [9], we take $A_{\rm disc} \sim \pi r_*^2 \sim 10\ {\rm kpc}^2$ and estimate $\lambda_* \sim 10^{-2-8\alpha}\, M_\odot\ {\rm yr}^{-1}$. We will provide another justification for the choice of $\lambda_*$ and examine the assumed approximate constancy of $A_{\rm disc}$ in §3. Uncertainties in Eq. (2.7) allow consideration of $\alpha = 1$, for which the estimate of $\lambda_* \sim 10^{-10}\, M_\odot\ {\rm yr}^{-1}$

does not depend on $A_{\rm disc}$ [see Eq. (2.11)]. In this case, $\lambda_*$ is simply the rate of gas consumption by star formation. We will examine this case as well.

## 2.4 Simulations of Star Forming Galaxies

In order to build a realistic star forming galaxy, we need to invsetgate each physical process and put them under the cosmological background. Unfortunately, almost every piece of these subgrid physics is unclear and lots of efforts have been put into the development the subgrid physics routine either from empirical semi analytic model or simulations based on some assumptions. In this section, we illustrated some commenly used approach of implementing star formation and stellar feedback as subgrid recipes.

One way to treat star formation in modeling galaxies is to use Eq. (2.1) or its equivalent, Eq. (2.3). In either case, estimates of $f_{\rm H_2}$ are required. For systems with sufficiently high SFRs, $f_{\rm H_2}$ depends on $\Sigma_g$, the metallicity, and the clumpiness of gas [10]. For systems with very low SFRs, $f_{\rm H_2}$ also depends on $\Sigma_{\rm SFR}$ [11]. Incorporating all the above dependences of $f_{\rm H_2}$, [11] showed that Eq. (2.3) provides a good description of the data on star formation for conditions ranging from poor to rich in molecular gas.

However, many simulations of galaxy formation do not evaluate $f_{\rm H_2}$ in implementing Eq. (2.1) or (2.3) for star formation (see e.g., the review by [12]). Instead, stars are assumed to form when gas has cooled below some temperature $T_{\rm max}$ and condensed to some threshold number density of atoms $n_{\rm min}$. For example, [13] chose $T_{\rm max} = 1.5 \times 10^4$ K and $n_{\rm min} = 0.1$ cm$^{-3}$. For a region with a total mass $M_g$ of the gas that satisfies the conditions and has a dynamic timescale $t_{\rm dyn} \propto (G\rho_g)^{-1/2}$, stars were assumed to form stochastically at a rate

$$\frac{dM_*}{dt} = 0.05\frac{M_g}{t_{\rm dyn}}. \tag{2.12}$$

In comparing the above equation with Eq. (2.1), $M_g$ is a proxy for $M_{\rm mol}$ while the numerical coefficient and $t_{\rm dyn}$ play the roles of $\epsilon_{\rm ff}$ and $t_{\rm ff}$, respectively. More recent

simulations of [14] adopted $T_{\max} = 10^4$ K, $n_{\min} = 10^2$ cm$^{-3}$, and an SFR per unit volume

$$\frac{d\rho_*}{dt} = 0.1\frac{\rho_g}{t_{\rm dyn}}, \tag{2.13}$$

where $\rho_*$ is the density of stars formed. The above SFL is qualitatively the same as Eq. (2.12).

After the first generation of stars were born, immediately, we need to consider all the influence they would bring to the system. Here, we only show one example about how different channels of stellar feedback mechanisms are treated reasonably and consistently in a galactic scale of system by [15] [16] [17], which can match with observations very well. Their model can explain the KS (Kenicutt-Schimdt) relation as well as the low SF efficiency $\epsilon_{\rm ff} \approx 10^{-2}$ [5] [8]. The high resolution $\sim$1pc of their simulations makes it possible to partially resolve the multi-phase ISM structure, which is highly inhomogeneous after considering stellar feedbacks. They devide the gas into three traditional phases: cold atomic+ molecular gas (T<2000K n>1 cm$^{-3}$), warm ionzed gas (2000K< T < $4\times10^5$K, n$\sim$ 0.01- 1 cm$^{-3}$) and hot gas (T> $4\times10^5$K, n<0.01 cm$^{-3}$) [16]. Gas gets cooled and collapse into Giant molecular clouds (GMCs), where star formation happens. And the subsequent stellar feedback would easily disperse GMCs. The formation and dispersal of GMCs reaches a dynamical steady state. And the consequence is that the amount of cold desnse gas which allow star formation is always limited. Star formation efficiency $\epsilon_{\rm ff}$ is very low, which naturally satisfies the KS laws. We follow this picture as the underlying assumptions of our gas dynamics and chemical evolution model for Fornax dSph.

In order to achieve this picture universally, they evaluate the effect of different feedback mechanism in different galaxy, where average gas density plays a key role. The cooling function $\Lambda(10^4K) \approx 10^{-23}$erg cm$^3$s$^{-1}$, thus the cooling timescale $\tau_{\rm cool} = kT/n\Lambda(T)$ $\approx$3000$(T/10^4{\rm K})$(1 cm$^{-3}$/n)yr varies in different density regions. In low density system $\langle n\rangle < 0.1cm^{-3}$, cooling time takes as long as the dynamical timescale $\sim$

Myr [15]. The energy deposited feedbacks are the most important source, which is the heating by photoionization, stellar winds and supernovae. Whereas in high density systems e.g. $n$ =100cm$^{-3}$, cooling takes much shorter time $\sim$yr, and the deposited energy is easily radiated away. In this case, the momentum deposition becomes the dominant stellar feedback echanism, which come from radiation pressure, supernovae and stellar winds. The momentum injected into the surrounding gas drives turbulence which is the key process to disrupt GMCs. From their results, all the feedback mechanisms contribute comparably to MW model, which makes it difficult to distringuish the effect of each. And dwarf galaxies fall into the low density systems, in which the energy deposited feeback plays the dominant role. And out of all, supernovae shock-heating is the key one. It is another advantage to study dwarf galaxy since they are sensitive to a specific feedback channel.

# Chapter 3

# Gas Mass and Net Gas Flow of Fornax

We now estimate $M_g(t)$ from the data on Fornax's $\psi(t)$ [9]. The data are binned across 13.75 Gyr and give the average SFR for each time bin. As discussed in Appendix B, we obtain a smooth $\psi(t)$ using a quadratic-spline fit that conserves the total number of stars formed in each bin and guarantees the continuity of $\psi(t)$ and $\mathrm{d}\psi/\mathrm{d}t$. The smooth $\psi(t)$ is shown along with the data in Fig. 3.1. By choosing an appropriate $\lambda_*$, we obtain from Eq. (2.10)

$$\frac{M_g(t)}{M_\odot} = \left[\frac{\psi(t)}{\lambda_*}\right]^{1/\alpha}. \tag{3.1}$$

As discussed in §2, comparison of our assumed SFL with empirical results gives an estimate of $\lambda_* \sim 10^{-2-8\alpha}\, M_\odot\ \mathrm{yr}^{-1}$. The choice of $\lambda_*$ is further justified by comparing the corresponding $M_g(t)$ with results from simulations of gas accretion by halos in a reionized universe. And then, in a more realistic picture, I treat $\lambda_*(t)$ as a function of time, considering the growth of star forming disk §4.

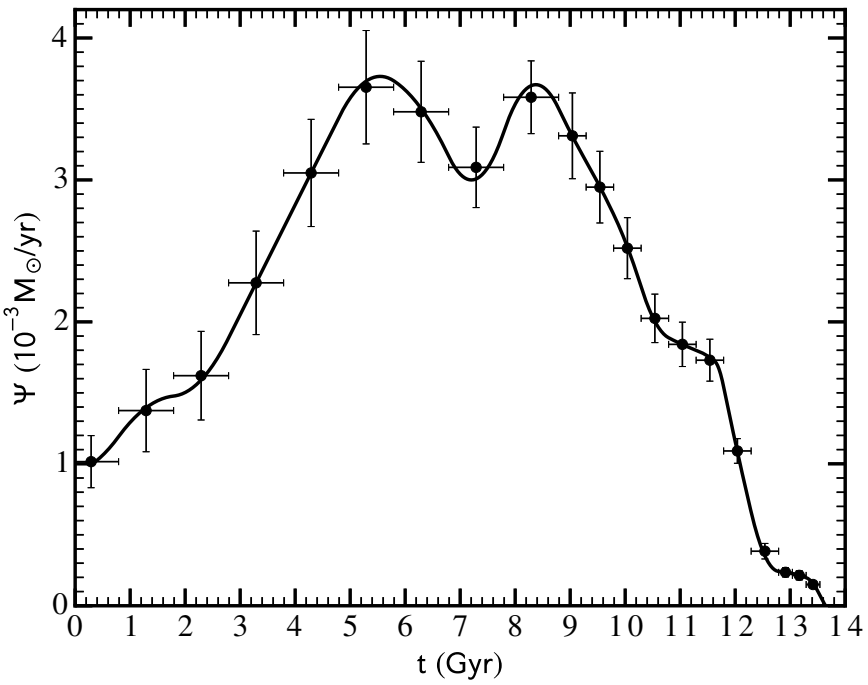


Figure 3.1: Data (filled circles with error bars) on Fornax's global star formation rate $\psi$ as a function of time $t$ since the big bang [9]. The data are binned according to time (converted from stellar age) and the horizontal error bar represents the size of each time bin. A quadratic-spline fit to the data (see Appendix B) is shown as the solid curve. We take the centroid of the first time bin at $t \approx 0.29$ Gyr as the onset and $t \approx 13.6$ Gyr given by the fit as the end of star formation in Fornax.

## 3.1 Baseline Case

We first discuss our baseline case of $\alpha = 1.5$ and $\lambda_* = 10^{-14}\, M_\odot\ \mathrm{yr}^{-1}$. The corresponding $M_g(t)$ calculated from Eq. (3.1) is shown as the solid curve in Fig. 3.2.

The evolution of $M_g(t)$ can be related to that of the halo hosting Fornax. and $M_g(t)$ increases all the way until t$\sim$ 5 Gyr, then begins to decrease towards the end of SFH. I suggest that it is around the time when Fornax stopped evolving independently and became a MW satellite. I seek to identify $t_{\rm sat}$ from the evolution of the net gas flow

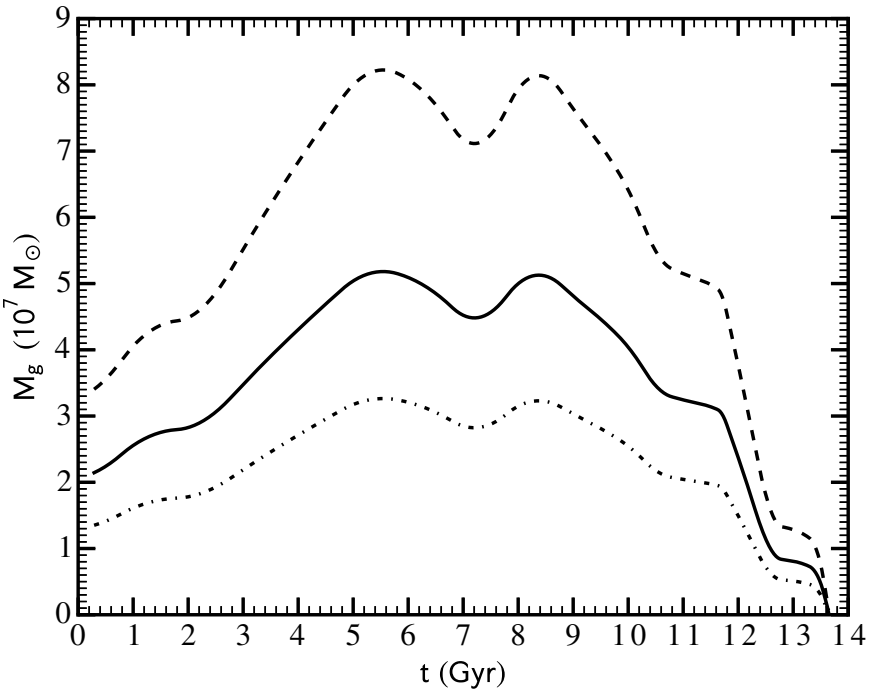


Figure 3.2: Total mass $M_g$ for cold gas in Fornax's star-forming disk as a function of time $t$ derived from Eq. (3.1) and the smooth $\psi(t)$ shown in Fig. 3.1. The solid curve is for the baseline case of $\alpha = 1.5$ and $\lambda_* = 10^{-14}\,M_\odot$ yr$^{-1}$. The dashed and dot-dashed curves are for the same $\alpha$ but different values of $\lambda_* = 5 \times 10^{-15}$ and $2 \times 10^{-14}\,M_\odot$ yr$^{-1}$, respectively. Note that all curves reach $M_g = 0$ at $t \approx 13.6$ Gyr, the end of star formation in Fornax.

rate

$$\Delta F(t) \equiv \frac{dM_g}{dt} + \psi(t). \tag{3.2}$$

A net inflow onto or outflow from the star-forming disk of Fornax corresponds to $\Delta F(t) > 0$ or $\Delta F(t) < 0$, respectively. I expect that the net gas inflow would stop at $t \sim t_{\rm sat}$.

I show the $\Delta F(t)$ calculated from Eq. (3.2) for the baseline case as the solid curve in Fig. 3.3. It can be seen that $\Delta F(t) > 0$ for $t < 6$ Gyr. The accretion of gas was expected from the rapid early growth typical of a halo. When the halo became an MW satellite,

its hot gas was lost through ram-pressure stripping and tidal interaction [18]; see also §5. The diminishing source for gas inflow caused the decline of $\Delta F$ from $t \approx 4.8$ Gyr to 6 Gyr. Based on the above discussion, I take the onset of the decline of $\Delta F$ at $t \approx 4.8$ Gyr as the time at which Fornax became an MW satellite, i.e., $t_{\rm sat} \approx 4.8$ Gyr.

## 3.2 Other Cases

For other cases of $\alpha = 1.5$, we vary $\lambda_*$ by a factor of 2 from the value for the baseline case and show the results on $M_g(t)$, $\Delta F(t)$ as the dashed ($\lambda_* = 5 \times 10^{-15}\, M_\odot\ {\rm yr}^{-1}$) and dot-dashed ($\lambda_* = 2 \times 10^{-14}\, M_\odot\ {\rm yr}^{-1}$) curves in Figs. 3.2, 3.3, and 4.1, respectively.It can be seen from Fig. 3.3 that the onset of the decline of $\Delta F$ at $t \approx 4.8$ Gyr are not affected by this variation of $\lambda_*$. Therefore, we again obtain $t_{\rm sat} \approx 4.8$ Gyr,

For cases of $\alpha = 1$ and 2, we choose $\lambda_*$ to obtain the same $M_g$ at $t \approx 4.8$ Gyr as the baseline case. This gives $\lambda_* = 7 \times 10^{-11}$ and $1.4 \times 10^{-18}\, M_\odot\ {\rm yr}^{-1}$ for $\alpha = 1$ and 2, respectively. These values are consistent with estimates based on empirical SFLs as discussed in §2. For convenience, we refer to the above cases of $\alpha = 1$ and 2 as cases 1 and 2, respectively. The corresponding results on $M_g(t)$, $\Delta F(t)$ are shown as the dashed (case 1) and dot-dashed (case 2) curves in Figs. 3.4, 3.5, respectively. The solid curves in these figures show the baseline case for comparison. It can be seen that the results for all three cases are rather similar. In particular, for all these cases, $t_{\rm sat} \approx 4.8$ Gyr (see Fig. 3.5), Therefore, we consider that our results on $M_g(t)$, $\Delta F(t)$, $t_{\rm sat}$ are insensitive to the exact form of our assumed SFL so long as it is consistent with the empirical SFLs discussed in §2.

## 3.3 Effects of Uncertainties in Fornax's SFH

Fornax's SFH as derived from observations [9] is affected by uncertainties in both the stellar age and the SFR. The age uncertainties are approximately taken into account by using appropriate time bins, the widths of which range from 0.25 Gyr for the youngest

stars to 1 Gyr for the oldest. The $1\sigma$ uncertainty in the average SFR for each bin is shown in Fig. 3.1. Our quadratic-spline fit of $\psi(t)$ conserves the total number of stars formed in each bin, and therefore, is affected by uncertainties in the average SFR. The results presented in §§3.1 and 3.2 are calculated from $\psi(t)$ fitted to the mean of the average SFR in each bin (filled circles in Fig. 3.1). Below we estimate how these results are affected by the uncertainties in the average SFR.

We assume that the average SFR for each time bin follows a Gaussian distribution with the standard deviation specified by the corresponding $1\sigma$ uncertainty. We make a Monte Carlo realization of the data by sampling the average SFR for each bin according to the relevant Gaussian distribution. We then obtain a quadratic-spline fit to the realization (see Appendix B) and use the fitted $\psi(t)$ to calculate $M_g(t)$ and $\Delta F(t)$ from Eqs. (3.1) and (3.2), respectively, for the baseline case and cases 1 and 2. A total of $10^3$ Monte Carlo realizations are carried out for each case. The 68% confidence interval for $\Delta F(t)$ in each case is shown in Fig. 3.6 along with the corresponding $\Delta F(t)$ presented in §3.1 or 3.2. It can be seen that the mean trend of $\Delta F(t)$ is rather well defined and similar for all of the three cases. In particular, for the baseline case, the 68% confidence interval for $\Delta F(t)$ resembles the range due to variation of $\lambda_*$ by a factor of 2 (see Fig. 3.3). Therefore, we do not consider that uncertainties in Fornax's SFH affect our results significantly.

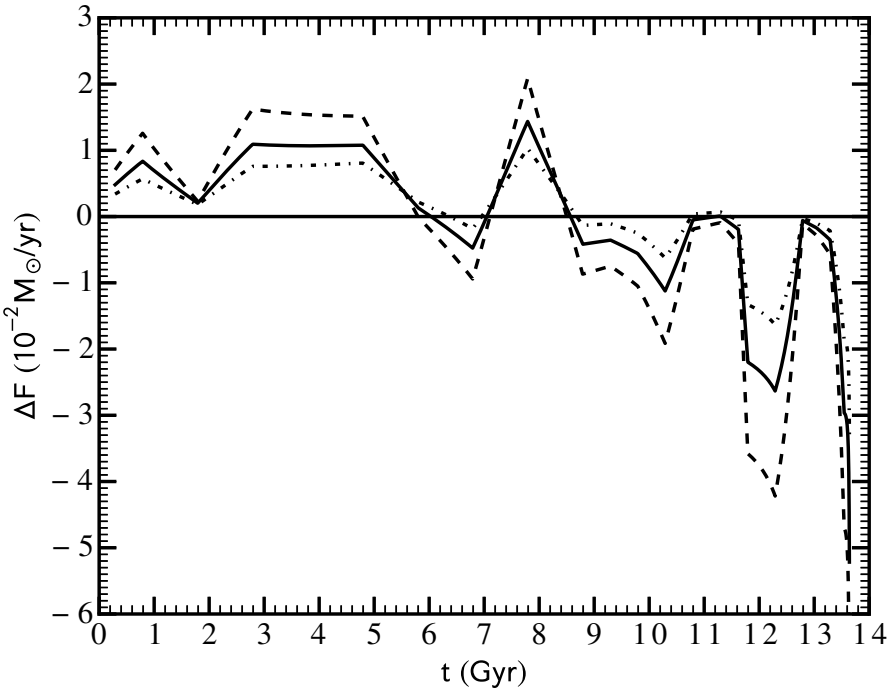


Figure 3.3: Rate $\Delta F$ of net gas flow to or from Fornax's star-forming disk as a function of time $t$ estimated from Eq. (3.2) and the results shown in Figs. 3.1 and 3.2. A net inflow or outflow corresponds to $\Delta F > 0$ and $< 0$, respectively. The solid curve is for the baseline case of $\alpha = 1.5$ and $\lambda_* = 10^{-14}\, M_\odot\ \mathrm{yr}^{-1}$. The dashed and dot-dashed curves are for the same $\alpha$ but different values of $\lambda_* = 5 \times 10^{-15}$ and $2 \times 10^{-14}\, M_\odot\ \mathrm{yr}^{-1}$, respectively. Note that all curves show similar features. Specifically, they have the same dip at $t \approx 1.8$ Gyr, which indicates the effect of reionization, and the same onset at $t \approx 4.8$ Gyr for transition from a net inflow to a net outflow, which indicates effects from Fornax's becoming an MW satellite. See text for details.

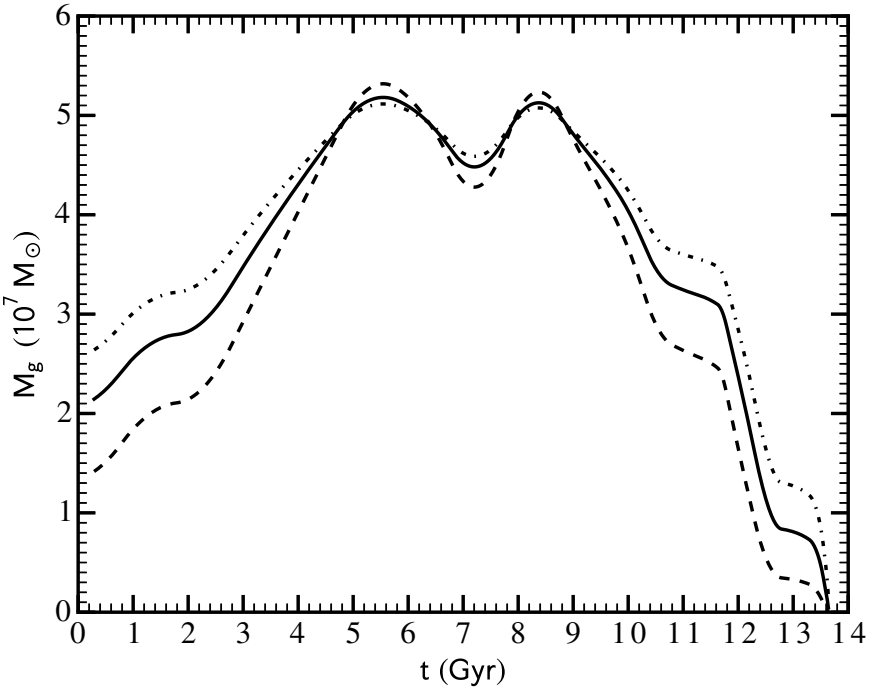


Figure 3.4: Same as Fig. 3.2 but for comparison of the baseline case ($\alpha = 1.5$ and $\lambda_* = 10^{-14}\,M_\odot$ yr$^{-1}$; solid curve) with cases 1 ($\alpha = 1$ and $\lambda_* = 7 \times 10^{-11}\,M_\odot$ yr$^{-1}$; dashed curve) and 2 ($\alpha = 2$ and $\lambda_* = 1.4 \times 10^{-18}\,M_\odot$ yr$^{-1}$; dot-dashed curve). Note that values of $\lambda_*$ for cases 1 and 2 are chosen to give the same $M_g(t_{\rm sat})$ at $t_{\rm sat} \approx 4.8$ Gyr as in the baseline case.

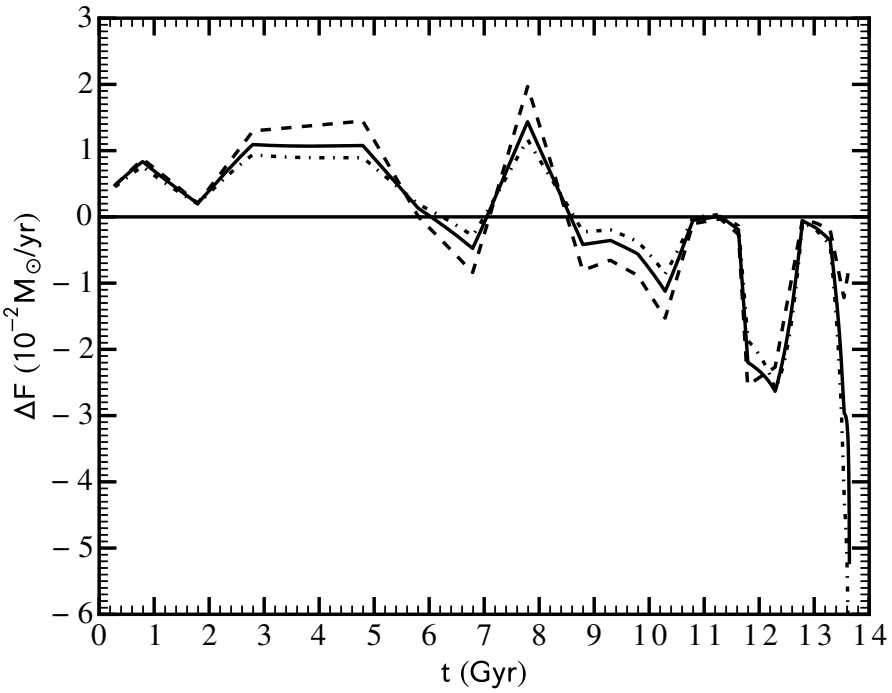


Figure 3.5: Same as Fig. 3.3 but for comparison of the baseline case ($\alpha = 1.5$ and $\lambda_* = 10^{-14}\,M_\odot$ yr$^{-1}$; solid curve) with cases 1 ($\alpha = 1$ and $\lambda_* = 7 \times 10^{-11}\,M_\odot$ yr$^{-1}$; dashed curve) and 2 ($\alpha = 2$ and $\lambda_* = 1.4 \times 10^{-18}\,M_\odot$ yr$^{-1}$; dot-dashed curve). Note that all curves show similar features with the same dip at $t \approx 1.8$ Gyr and the same onset at $t \approx 4.8$ Gyr for transition from a net inflow to a net outflow.

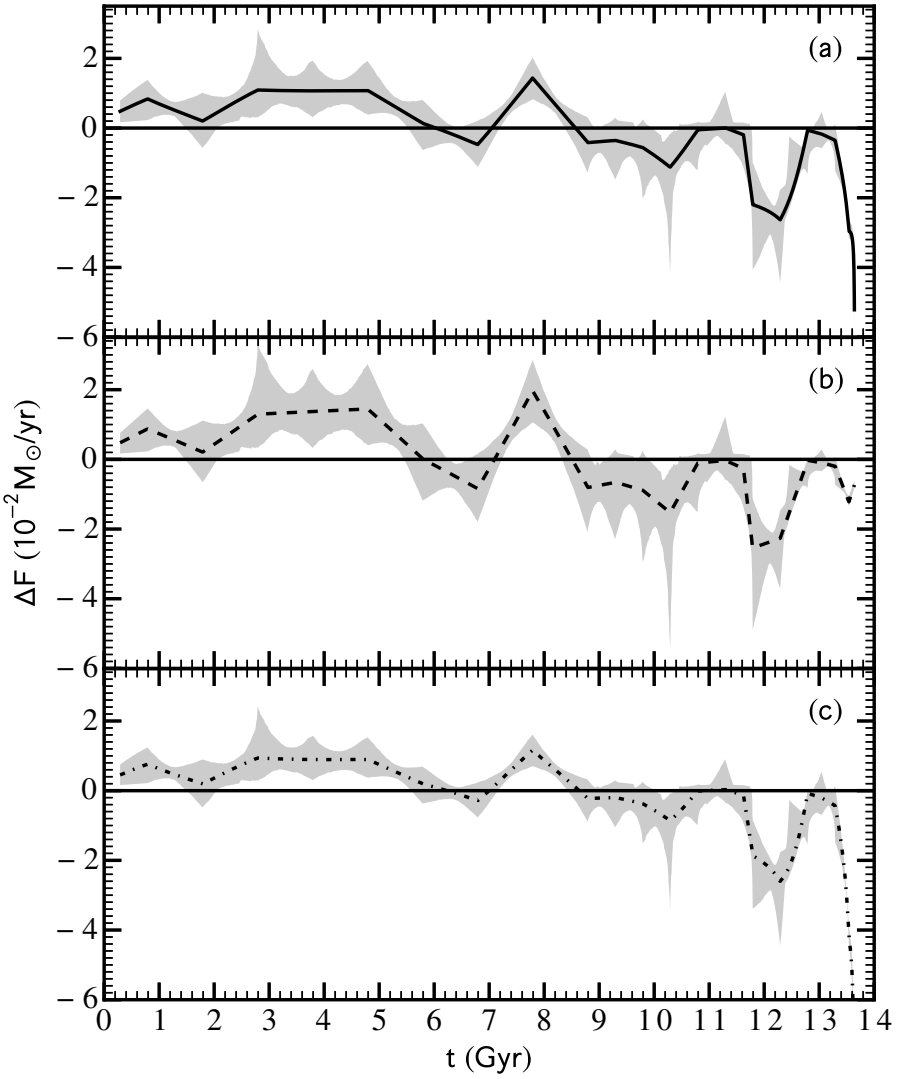


Figure 3.6: Uncertainties in the rate of net gas flow $\Delta F(t)$ in (a) the baseline case ($\alpha = 1.5$ and $\lambda_* = 10^{-14}\, M_\odot\ \mathrm{yr}^{-1}$), (b) case 1 ($\alpha = 1$ and $\lambda_* = 7 \times 10^{-11}\, M_\odot\ \mathrm{yr}^{-1}$), and (c) case 2 ($\alpha = 2$ and $\lambda_* = 1.4 \times 10^{-18}\, M_\odot\ \mathrm{yr}^{-1}$). For each case, the shaded region indicates the 95% confidence interval for $\Delta F(t)$ based on $10^3$ Monte Carlo realizations of the data on $\psi(t)$ shown in Fig. 3.1. The curves are the same as those shown in Fig. 3.5, and are calculated from the mean values of $\psi(t)$ shown as filled circles in Fig. 3.1. Note that the overall trend of $\Delta F(t)$ is rather robust and similar in all cases.

# Chapter 4

# Dark Matter Halo Evolution and Gas Content from Simulations

In this chapter, our goal is to find a candidate halo which is suitable to host Fornax dSph based on the gas dynamics discussed in §3. Combining the gas mass evolution and the mean dark matter halo growth history [19] of the candidate halo, the baryonic to dark matter ratio can be tracked and compared with simulations [20], which puts another constrains on the choice of $\lambda_*$. Beyond that, we build a more realistic picture of the galaxy formation of Fornax dSph, assuming a growing star forming disk according to its halo growth history.

## 4.1 Candidate Halo for Fornax dSph

From last chapter, we infer $M_g$ and $\Delta F$ from SFR, and obtain generic features of both curves, using variety forms of Schmidt law with constant $\lambda_*$. We will validate the choice of $\lambda_*$ from the point of view based on the host halo growth history [19] in this section. We try to find a halo candidate for Fornax which can match with the half light mass observations [21]. And then we use cosmological simulation results [20] to estimate the gas content according to its evolution history.

In the first step, the hint from the gas dynamics of Fornax is the key to identify the host halo. We already suggest that the infall time is $t_{sat} \approx 4.8$ Gyr. Our strategy is tracking the mean growth history of halos with different masses collapsing at $t_{\rm sat}$. Out of all the halo profiles, we are aiming to find a candidate, which can satisfies the half light mass criteria.

The major tool we used here is the mean halo growth histories of different halos [19]. They are extracted from ΛCDM simulations and demonstrated to be a realistic simplification of halo evolution. Zhao et al [19] found that $\delta_{\rm c}(z)$, the critical overdensity for spherical collapse is an equivalent parameter of time; and $\sigma_M$, the rms of the linear density filed on mass scale M can be used as the parameter of the halo mass. A universal relation can be found between these two quantities, using a large set of N-body simulations of various structure formation models. And then they are able to statistically obtain the mean growth history of a halo with certain mass collapsing at a specific time.

Since the mean mass accretion model depends on the cosmological settings. we need to specify the parameters of the cosmology and of the initial density fluctuation spectrum. Throughout this paper, we adopt $h = 0.69$, $\Omega_m = 0.29$ ($\Omega_{\rm CDM} = 0.243$, $\Omega_b = 0.047$), and $\Omega_\Lambda = 0.71$. In calculating the growth of a halo, we use a primordial power spectrum with a spectral index $n_s = 0.96$ and the transfer function of [22] with a present temperature of 2.726 K for the cosmic microwave background to obtain the linear power spectrum, the amplitude of which is fixed by $\sigma_8 = 0.82$. The above cosmological parameters are consistent with the final analysis of the WMAP experiment [23].

For our purpose of finding a reasonable halo mass evolution history for Fornax, we need to specify its mass at certain redshift. As discussed in Appendix C, we made variety of trials of different dark matter halo mass $M_h(t_{\rm sat})$ at $t_{\rm sat}$, and select the appropriate one to obtain a mass $M(< r_{1/2}) = 7.39^{+0.41}_{-0.36} \times 10^7\, M_\odot$ enclosed within the half-light radius $r_{1/2} = 944 \pm 53$ pc as derived from observations [21]. We find the halo with $M_h(t_{\rm sat}) \approx 1.8 \times 10^9\, M_\odot$ satisfies the condition.

## 4.2 Gas Content in the Candidate Halo

After fixing the candidate halo for Fornax, we are able to move onto the next step: Estimation the gas content as a function of time in the halo, which is characterized by the parameter $f_b(t) = M_g(t)/M_h(t)$. Extensive studies have been done on the prediction of $f_b(t)$ from ΛCDM simulations combined with variety of gas physics. The main feedback process we need to consider in pre-satellite epoch is reionization. We need to address that we do not consider the effect of SN feedback in this phase. More specifically, we assume that it has negligible influence on the gas budget although it very possibly brings lots of turbulence into the ISM. Because the system is dominated by inflow gas $\Delta F > 0$, it is hard to find outlet for gas outflows. Whereas reionization is the controlling factor of the gas amount in the host halo in this phase. Basically, it is an UV background produced by the first bunch of quasars and stars in the universe. And the consequence is suppression or quenching SF in small galaxies by photoheating their gas, which gets too hot to be contained in their shallow potential wells. Such process happened very early and completed z $\sim$ 10 in MW. After the local group is fully ionized, nearby small galaxies are harder to accrete gas. Busha et al [24] use the high-resolution Lactea II simulations combined with the LasDamas Collaboration to obtain the reionization history of MW and its satellites halos. They find that halos with $T_{\rm vir}$ larger than $8 \times 10^3$ K can cool gas efficiently before reionization begins. After that, gas is heated to a few times $10^4$ K, which quenches SF. Only these halos have sufficient large mass, corresponding to $T_{\rm vir} = 10^5$K are able to accrete the photoionized gas, at which temperature these gas could be viralized and eventually cooled through variety of channels. By varying reionization time in the reasonable range of MW, they are able to match the satellite number with the observations which solves the missing satellite problem, as well as matching their $v_{max}$ distribution, radial distribution, and etc.

Busha et al's work shows the importance of reionization in building a realistic galaxy formation picture. Beyond that, Okamoto et al similarly reconstructed the reionized

universe and predict baryonic to dark matter ratio for different halos at any given redshift [20]. Using more sophisticated gas accretion model, halos below the mass limit set by [24] may also be able to accrete some gas. It is widely accepted that an universal criteria of gas accretion is that $T > T_{\rm vir}$, where T, as the temperature of IGM, depends on $\rho$. It remains to be an important question that at which density we should evaluate T. From previous studies, the two common choices are (i) $\rho = \langle\rho\rangle$ and (ii) $\rho = 1000\langle\rho\rangle$. Okamoto et al calculated the gas density roughly as $\rho_{\rm vir}/3$ at the edge of the halo (at $R_{\rm vir}$) from simulations. The criteria that gas will be prevented from accretion is $T_{\rm eq}(\rho_{\rm vir}/3) > T_{\rm vir}$. Therefore, $T_{\rm vir}$ is calculated from halo growth history, which depends on halo mass and redshift. They also consider gas evaporation process in the model: After relaxation, the system gets thermal equilibrium, and each particle has the same temperature. Thus, the speed of some low mass members can be greater than the escape velocity of the cluster $v = \sqrt{2kT/m}$, which results in these members being lost to the cluster. Therefore, the gas content within the galaxy at the current timestep is the sum of the newly accreted gas and the gas from last timestep after taking out the amount which gets evaporated. From their simulation results, they showed that at $t > t_{\rm reion}$, the baryonic mass fractions for halos of mass $M$ are distributed around the mean value

$$\bar{f_b}(M,t) = \langle f_b\rangle\{1 + (2^{2/3} - 1)[M_c(t)/M]^2\}^{-3/2}, \tag{4.1}$$

where $M_c(t)$ is a characteristic halo mass determined from their simulations and is shown as the dashed curve in fig. $\langle f_b\rangle \equiv \Omega_b/(\Omega_{\rm CDM} + \Omega_b) \approx 0.16$ is the cosmic mean mass fraction of baryons, and $\Omega_{\rm CDM} = 0.243$ and $\Omega_b = 0.047$ are the fractional contributions to the critical density of the present universe from CDM and baryons, respectively. The above equation gives $\bar{f_b} = \langle f_b\rangle/2$ for $M = M_c(t)$ and $\bar{f_b} = \langle f_b\rangle$ in the limit $M \gg M_c(t)$. We now compare our results on $M_g(t)$ and $M_h(t)$ at $t < t_{\rm sat}$ with simulations of gas accretion by halos in a reionized universe. Fig. 4.1 shows that compared to this case, the agreement between $f_g$ and $\bar{f_b}$ for $1.8 \lesssim t \lesssim 4.8$ Gyr is slightly improved to within a factor of $\sim 1.5$ for $\lambda_* = 2 \times 10^{-14}\, M_\odot\ {\rm yr}^{-1}$ and somewhat worsened to within a

factor of $\sim 3$ for $\lambda_* = 5 \times 10^{-15}\, M_\odot\ \mathrm{yr}^{-1}$. Based on the above results, we consider that $\lambda_* = (0.5\text{–}2) \times 10^{-14}\, M_\odot\ \mathrm{yr}^{-1}$ is reasonable for $\alpha = 1.5$ with the baseline case being representative.

In comparing the $f_g(t)$ and $\bar{f}_b(t)$ shown in Fig. 4.1, we note that [20] assumed a reionization redshift of $z = 9$ corresponding to $t = 0.55$ Gyr. A more careful comparison needs us to fix the reionization redshift in Fornax dSph. We also note that this agreement between $f_g$ and $\bar{f}_b$ is not affected by adding the contribution of stars to $f_g$ as the mass of stars is always significantly smaller than that of gas for $t \lesssim 4.8$ Gyr. Therefore, we consider that our choice of $\lambda_* = 10^{-14}\, M_\odot\ \mathrm{yr}^{-1}$ for the baseline case is reasonable.

## 4.3 Growth of Star Forming Disk

After the evaluation of $\lambda_*$ from the comparisons of $f_b$ from simulations, We are able to move on to a more realistic picture by taking account in the growth of star forming disk. Before Fornax becomes the satellite of MW, its halo keeps growing as well as the star forming disk.

We use the disk growth model by [25] , they studied the formation of galactic disks based on several simple assumptions, and the results can match observations from many aspects naturally. The key assumption is that all discs have masses and angular momenta with fixed fractions of those of their halos, which is characterized by two parameters, $m_\mathrm{d}$, $j_\mathrm{d}$ respectively. In a singular isothermal sphere model, the disk size can be represented as

$$r_\mathrm{d} = \frac{1}{\sqrt{2}} \left( \frac{j_\mathrm{d}}{m_\mathrm{d}} \right) \lambda r_\mathrm{vir}, \tag{4.2}$$

$\lambda$ is the spin parameter of the halo. As we can tell, for a halo with fixed $m_\mathrm{d}$, $j_\mathrm{d}$ and $\lambda$, the disc size simply scales with the viral radius. (see detail derivation is in AppendixC). As for NFW profile,

$$r_\mathrm{d} = \frac{1}{\sqrt{2}} \left( \frac{j_\mathrm{d}}{m_\mathrm{d}} \right) \lambda r_\mathrm{h} f_\mathrm{c}^{-1/2} f_\mathrm{R}(\lambda, c, m_\mathrm{d}, j_\mathrm{d}) \tag{4.3}$$

where both $f_{\rm c}$ and $f_{\rm R}$ weakly depends on c, which changes with time (AppendixC). Thus, we reach the conclusion that in NFW density profile, the growth of disc also approximately scales with the virial radius.

We study the case of $\alpha = 1.5$. According to Eq. (2.11), $\lambda_* \propto A_{\rm disc}^{-0.5} \propto r_{\rm d}^{-1}$. We set $\lambda_*(t_{\rm sat}) = \lambda_{*,0} = 10^{-14}\, M_\odot\ {\rm yr}^{-1}$, thus before $t_{\rm sat}$, $\lambda_*(t)$ evolves as

$$\lambda_*(t) = \lambda_{*,0} \frac{r_{\rm d}(t_{\rm sat})}{r_{\rm d}(t)} = \lambda_{*,0} \frac{r_{\rm vir}(t_{\rm sat})}{r_{\rm vir}(t)} \tag{4.4}$$

After $t_{\rm sat}$, Fornax falls into MW potential well. The halo outskirt loses dark matter to MW, whereas the inner part almost keeps intact. Thus I assume that the star forming region remains the same afterwards. Now we are able to recalculate $M_g$, $\Delta F$ and $f_g$ as a function of time. The major difference is the suppression of the gas mass before $t_{\rm sat}$, due to a larger time dependent $\lambda_*(t)$. It is a more reasonable scenario as we see a growing curve of gas mass from $M_g(t_s) \approx 0$ in the upper panel of Fig.4.3 rather than $M_g(t_{\rm ini}) \approx 2 \times 10^7 M_\odot$ with the constant $\lambda_*$ case in Fig.3.2. Similarly, $f_g$ is closer to the predicted $\bar{f}_b$ from Fig. 4.4. In order to build a more realistic gas model, we fixed $f_g = 0.16$ if it shoots over the cosmic mean value at the very beginning, shown in the lower panel of Fig.4.3. Such treatment produced a small spike around $t \approx$0.5 Gyr in $\Delta F$, as shown in the lower panel of4.4. This feature is artificial and only changes $\Delta F$ at the very early time of SFH, when the age resolution is coarse (1 Gyr). Thus it causes negligible effect on our model.

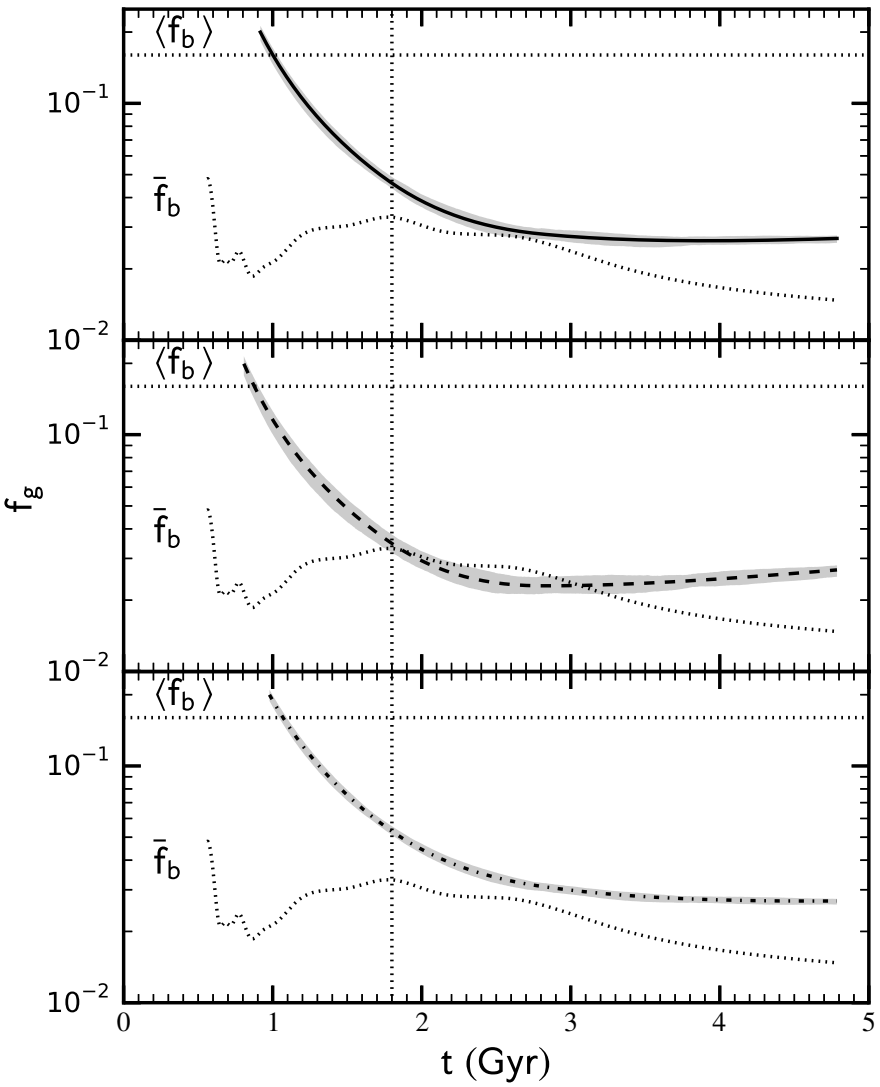


Figure 4.1: Fornax's gas mass fraction $f_g = M_g/M_h$ as a function of time $t$ before it became an MW satellite at $t_{\rm sat} \approx 4.8$ Gyr [dashed, solid, and dot-dashed curves for $\alpha = 1.5$ and $\lambda_* = 5 \times 10^{-15}$, $10^{-14}$ (baseline case), and $2 \times 10^{-14}\, M_\odot\ {\rm yr}^{-1}$, respectively]. For each case, the shaded region indicates the 95% confidence interval for $\Delta F(t)$ based on $10^3$ Monte Carlo realizations of the data on $\psi(t)$ shown in Fig. 3.1. The dotted curve shows the mean baryon mass fraction $\bar{f}_b(t)$ calculated from Eq. (4.1) for Fornax-like halos in a universe reionized at $z = 9$ ($t \approx 0.55$ Gyr). The vertical dotted line indicates the upper bound on the approximated reionization time $t_{\rm reion} \approx 1.8$ Gyr in the local group. The agreement to within a factor of $\sim 3$ between $f_g(t)$ and $\bar{f}_b(t)$ for $t \approx 1.8$–4.8 Gyr justifies the range of $\lambda_*$ for $\alpha = 1.5$. The horizontal dotted line indicates the cosmic mean mass fraction of baryons $\langle f_b \rangle$.

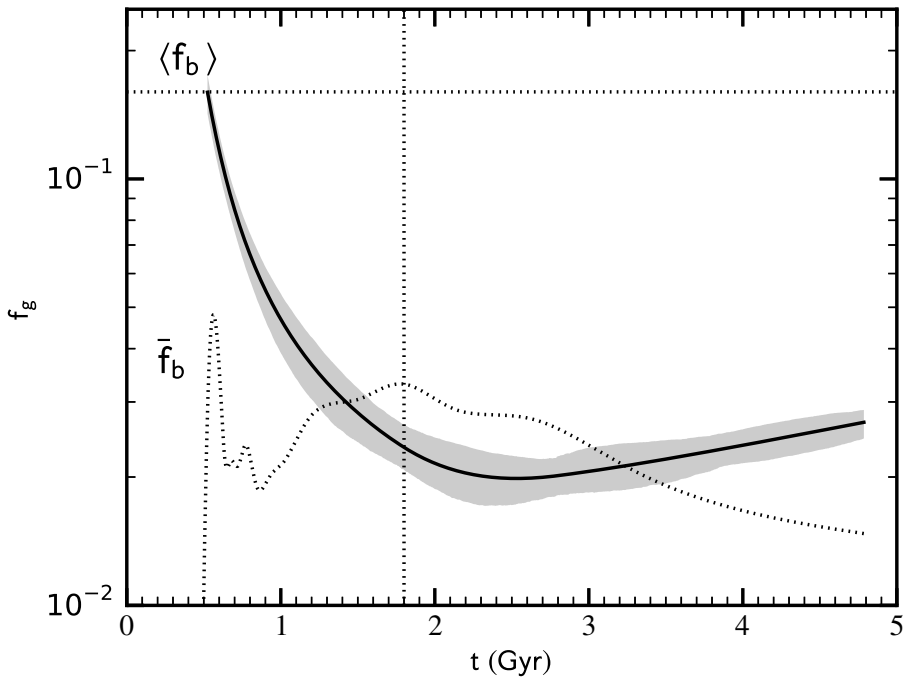


Figure 4.2: The same notation as Fig. 4.1. Fornax's gas mass fraction $f_g = M_g/M_h$ as a function of $t$ in a growing star-forming disk model with SFH uncertainty.

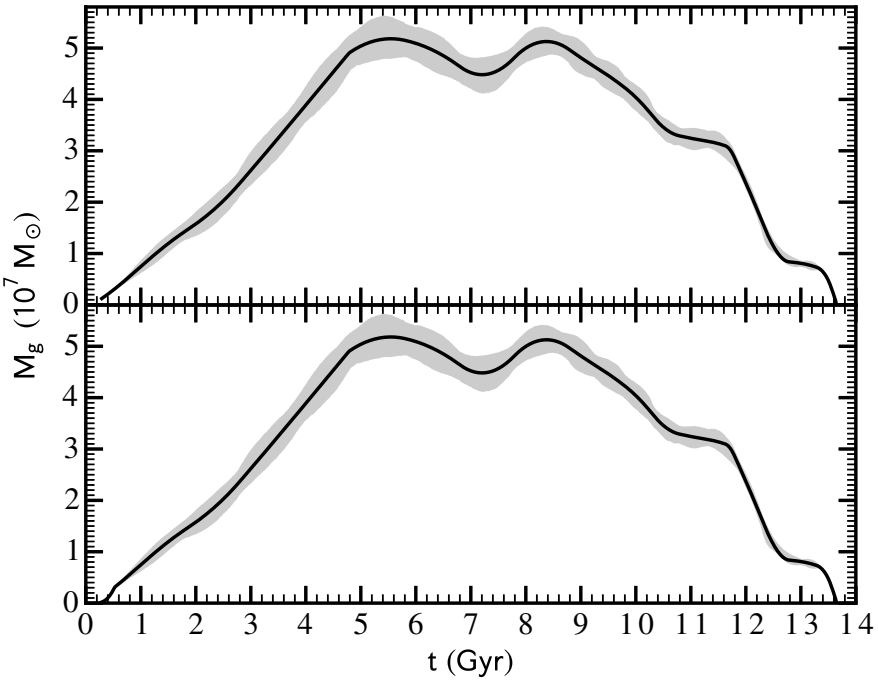


Figure 4.3: Fornax's gas mass $M_g$ as a function of $t$ in a growing star-forming disk model with SFH uncertainty. The upper panel shows the direct derivation of $M_g$ from Eq. 3.1.The lower panel shows the case with artificial cut of $f_b = 0.16$, see detail in text.

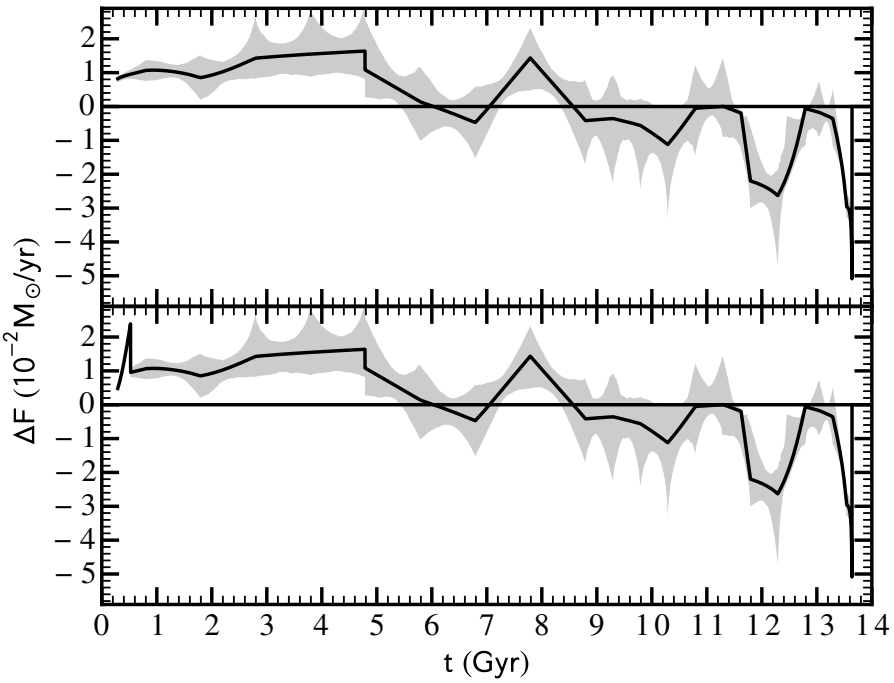


Figure 4.4: The same notation as Fig. 4.3. Fornax's net gas flow $\Delta F$ as a function of $t$ in a growing star-forming disk model with SFH uncertainty and artificial cut of $f_b = 0.16$.

# Chapter 5

# Global Gas Dynamics and Evolution of Fornax as an MW Satellite

Based on the discussions in §3, we consider that the growing disk case with $\lambda_{*,0} = 10^{-14}\,M_\odot\ \mathrm{yr}^{-1}$ gives representative results on the general evolution of Fornax. In this chapter, we focus on this case to discuss the global gas dynamics and evolution of Fornax as an MW Satellite. We note that it the same as the baseline case after $t_{\rm sat}$. As mentioned in §3, we take the onset of the decline in $\Delta F$ at $t_{\rm sat} \approx 4.8$ Gyr as the time at which Fornax was accreted by the MW. Fig. 5.1 shows that $\Delta F$ dropped to zero at $t \approx 6$ Gyr and the first net outflow ($\Delta F < 0$) occurred for $t \approx 6$–7 Gyr. This was followed by the final round of net inflow ($\Delta F > 0$) for $t \approx 7$–8.6 Gyr, and then by several episodes of net outflow until star formation ended in Fornax. As we discuss below, the episodic gas flows at $t > 4.8$ Gyr shown in Fig. 5.1 were driven by Fornax's orbital motion and its tidal interaction with the MW.

## 5.1 Orbital Motion and Tidal Interaction

Observations show that Fornax currently moves in an elliptical orbit with a period of $\sim 3.2$ Gyr. Its distance from the MW center is $R_p \sim 118$ kpc at the perigalacticon and $R_a \sim 152$ kpc at the apogalacticon [26]. Using the median halo growth history and the corresponding halo structure given by the model of [19], we find that for a present-day MW halo mass in the range of (1–2) $\times 10^{12}\, M_\odot$, the MW mass enclosed by Fornax's present-day orbit is $\sim 1.5$ times the MW halo massat $t_{\rm sat} \approx 4.8$ Gyr when Fornax became a satellite. In view of this moderate change, we assume that Fornax's orbit for $t \gtrsim 4.8$ Gyr can be approximately described by the present-day parameters. For estimates, we take the MW mass enclosed within Fornax's orbit to be $M_{\rm MW}^{\rm encl} \sim 7.5 \times 10^{11}\, M_\odot$ on average. This gives an average orbital velocity of $v_{\rm For} \sim (GM_{\rm MW}^{\rm encl}/a)^{1/2} \sim 150$ km/s for Fornax, where $a = (R_p + R_a)/2 \sim 135$ kpc. For comparison, the circular velocity characterizing matter motion inside the Fornax halo at $t_{\rm sat} \approx 4.8$ Gyr is $v_{\rm circ} = (GM_h/r_{\rm vir})^{1/2} \approx 21$ km/s with $M_h \approx 1.8 \times 10^9\, M_\odot$ and $r_{\rm vir} \approx 17$ kpc

The effects of tidal interaction between the MW and Fornax can be estimated from the radii $r_{{\rm RS},p}$ and $r_{{\rm RS},a}$ of the instantaneous Roche spheres [27] at the perigalacticon and apogalacticon, respectively. Ignoring the small eccentricity of $\sim 0.13$ for Fornax's orbit [26], we have

$$\frac{r_{{\rm RS},p}}{R_p} \approx \frac{r_{{\rm RS},a}}{R_a} \approx \left(\frac{M_{\rm For}}{3M_{\rm MW}^{\rm encl}}\right)^{1/3}, \tag{5.1}$$

where $M_{\rm For}$ is the total mass of Fornax and generally differs from $M_h$ at $t_{\rm sat} \approx 4.8$ Gyr due to tidal interaction. The CDM and gas outside the Roche sphere would be lost from Fornax. However, because the Roche sphere would expand as Fornax moved from the perigalacticon to the apogalacticon, some of the CDM and gas lost earlier could be reaccreted. Guided by the simulations of [28] and our derived $\Delta F$, we assume that reaccretion occurred only once. Subsequently, $M_{\rm For}$ settled down to a value set by the mass enclosed within $r_{{\rm RS},p}$. For estimates, we use the density profile given by the model of [19] for a halo with $M_h \approx 1.8 \times 10^9\, M_\odot$ at $t_{\rm sat} \approx 4.8$ Gyr. Assuming that Fornax

was at the apogalacticon at $t_{\rm sat} \approx 4.8$ Gyr with $M_{\rm For} \approx 1.8 \times 10^9\,M_\odot$, we estimate that its total mass was quickly reduced to $\sim 1.6 \times 10^9\,M_\odot$, which corresponds to the mass enclosed within the Roche sphere at this time. The mass of the Fornax halo was further reduced to $\sim 1.3 \times 10^9\,M_\odot$ at $t \sim 6.4$ Gyr when it was at the perigalacticon with a smaller Roche sphere. It then reaccreted some of the CDM (and gas) lost earlier to obtain $M_{\rm For} \sim 1.5 \times 10^9\,M_\odot$ at $t \sim 8$ Gyr when it was at the apogalacticon again. After that $M_{\rm For}$ settled down to $\sim 1.2 \times 10^9\,M_\odot$, which is enclosed within $r_{{\rm RS},p}$ estimated from Eq. (5.1) for this value of $M_{\rm For}$. During the above evolution of the Fornax halo, $r_{{\rm RS},a}$ started at $\sim 14$ kpc and settled down to $\sim 12$ kpc while $r_{{\rm RS},p}$ decreased from $\sim 11$ kpc to $\sim 10$ kpc. The evolution of $M_{\rm For}$, $r_{{\rm RS},a}$, and $r_{{\rm RS},p}$ is sketched in Fig. 5.1.

Based on the above discussion, we estimate that Fornax lost $\sim 1/3$ of its CDM through tidal interaction. However, this loss occurred in the outermostregion of the halo and had little effect on the structure of its interior. For example, because $r_{1/2} \approx 944$ pc was well within the Roche sphere at all times, the mass $M(< r_{1/2})$ enclosed within $r_{1/2}$, which is used to determine $M_h$ at $t_{\rm sat} \approx 4.8$ Gyr (see Appendix C), would not have been affected by tidal interaction. Similarly, with a radius of $\sim 2$ kpc, the star-forming disk would have remained largely intact as Fornax orbited the MW so long as there was a sufficient supply of cold gas.

## 5.2 Gas Inflow and Outflow

Over Fornax's SFH, the star-forming disk was surrounded by hot gas either accreted from the IGM or expelled from the disk due to feedback from star formation, which includes SN explosions and heating by stellar radiation. Cooling of this hot gas gave rise to an inflow onto the disk while stellar feedback produced an outflow from it. The net gas flow rate $\Delta F$ represents the difference between the two. At $t < 4.8$ Gyr, accretion of the IGM by the growing Fornax halo dominated its global gas dynamics and supplied hot gas that cooled to provide a net inflow. In general, reducing the amount of hot

gas would suppress the inflow, thereby causing $\Delta F$ to decrease. This accounts for the decline of $\Delta F$ for $t \approx 4.8$–6 Gyr (see Fig. 5.1) as accretion of the IGM was disrupted and the initial tidal interaction between Fornax and the MW resulted in loss of hot gas along with CDM. This gas loss was also aided by ram-pressure stripping as discussed in §5.3. The corresponding suppression of the inflow allowed the brief first occurrence of a net outflow for $t \approx 6$–7 Gyr as hot gas escaped from the star-forming disk. This outflow carried only $\sim 2 \times 10^6\, M_\odot$ and was soon quenched when $\sim 10^7\, M_\odot$ of the hot gas lost earlier was reaccreted and cooled to produce an inflow for $t \approx 7$–8.6 Gyr (see Fig. 5.1).

As mentioned in §5.1, some of the gas and CDM lost earlier was reaccreted because the Roche sphere expanded at the apogalacticon (see Fig. 5.1). This reaccretion was discussed for gas by [29] and seen for CDM in simulations by [28]. However, our derived $\Delta F$ indicates that there was only one episode of significant reaccretion for Fornax. This is in line with its smooth SFH, which does not match the scenario of episodic starbursts with repeated gas expulsion and reaccretion discussed by [29]. In the absence of further reaccretion, several episodes of net outflow occurred in Fornax for $t \approx 8.6$–13.6 Gyr (see Fig. 5.1). We consider that the episodic nature of these outflows is mainly due to Fornax's orbital motion and is very different from the episodic behavior purely driven by stellar feedback as discussed for example, by [13]. Specifically, we argue that although stellar feedback initiated the escape of hot gas from the star-forming disk, the loss of such gas from the Fornax halo at $t \approx 8.6$–13.6 Gyr was driven by tidal interaction and ram-pressure stripping.

## 5.3 Ram-Pressure Stripping

We consider that the gas subject to ram-pressure stripping was dispersed outside Fornax's star-forming disk but within its Roche sphere of $\sim 10$ kpc in radius. From the $\Delta F$ shown in Fig 5.1, we estimate that $\sim 10^7\, M_\odot$ of gas were stripped for each episode.

So this gas had a density of $n \sim 10^{-4}$ cm$^{-3}$ while inside Fornax. Its internal pressure was $P \sim nkT \sim m_p n v_{\rm th}^2$, with $T$ being its temperature, $v_{\rm th} \sim (kT/m_p)^{1/2} \sim 29(T/10^5\ {\rm K})^{1/2}$ km/s its thermal velocity, and $k$ the Boltzmann constant. The ram pressure can be estimated as

$$P_{\rm ram} \sim m_p n_{\rm med} v_{\rm For}^2, \tag{5.2}$$

where $n_{\rm med}$ is the density of the gaseous medium through which Fornax moved. Ram-pressure stripping occurred when $P_{\rm ram}$ exceeded $P$, i.e.,

$$n_{\rm med} v_{\rm For}^2 > n v_{\rm th}^2. \tag{5.3}$$

For the hot gas accreted from the reionized IGM right before Fornax became an MW satellite, we estimate $v_{\rm th} \sim v_{\rm circ} \sim 21$ km/s. This gas would be stripped for $n_{\rm med} \gtrsim 2 \times 10^{-6}$ cm$^{-3}$.

The majority of the gas stripped from Fornax first escaped from its star-forming disk due to stellar feedback. For a crude estimate, we assume that the gas in this disk consisted of three components [30]: cold gas with a density of $n_{\rm cold} \sim 40$ cm$^{-3}$ and a temperature of $T_{\rm cold} \sim 80$ K, warm partially-ionized gas with $n_{\rm warm} \sim 0.3$ cm$^{-3}$ and $T_{\rm warm} \sim 8000$ K, and hot ionized gas with $n_{\rm hot} \sim 4 \times 10^{-3}$ cm$^{-3}$ and $T_{\rm hot} \sim 5 \times 10^5$ K. The total gas mass was dominated by the cold component that fed star formation. Cold gas was also converted by stellar feedback to maintain the hot component as hot gas escaped from the disk in an outflow. Assuming adiabatic cooling during its escape, we estimate an upper limit of $T \sim T_{\rm hot}(n/n_{\rm hot})^{2/3} \sim 4 \times 10^4$ K corresponding to $v_{\rm th} \sim 18$ km/s for the hot gas when it was dispersed inside the Roche sphere. Its stripping requires $n_{\rm med} \gtrsim 10^{-6}$ cm$^{-3}$.

Based on the above discussion, with $n_{\rm med} \gtrsim 2 \times 10^{-6}$ cm$^{-3}$ for the gaseous medium around Fornax's orbit at $\sim$ 118–152 kpc from the MW center, ram-pressure stripping would have occurred to both accreted hot gas for $t \approx 4.8$–6 Gyr and gas heated by stellar feedback for $t \approx 8.6$–13.6 Gyr in Fornax. The gas density in the present MW halo can only be estimated by indirect means and its time evolution over the MW's history

can only be estimated by simulations of galaxy formation. Simulations of [31] give $n_{\rm med} \sim 10^{-5}$–$10^{-4}$ cm$^{-3}$ at $\sim$ 100–200 kpc from the galactic center with no significant changes over a period of 10 Gyr. These results are consistent with estimates based on observations of MW halo clouds (e.g., [32]). However, [33] derived a present limit of $n_{\rm med} < 10^{-5}$ cm$^{-3}$ at 50 kpc from the MW center by considering effects on the Magellanic Stream. For comparison, the cosmic mean baryon density at $t_{\rm sat} \approx 4.8$ Gyr ($z_{\rm sat} \approx 1.33$) was $\langle n_b \rangle \approx 3 \times 10^{-6}$ cm$^{-3}$. We consider $n_{\rm med} \sim 3 \times 10^{-6}$–$10^{-5}$ cm$^{-3}$ as reasonable around Fornax's orbit for $t \gtrsim 4.8$ Gyr. Therefore, ram-pressure stripping would have been effective in removing gas from Fornax.

For the three gas components in Fornax's star-forming disk with densities and temperatures assumed above, they were in pressure equilibrium and their internal pressure was $\gtrsim 10^2$ times the ram pressure. Consequently, for those conditions the ram pressure would have had little impact on the disk. However, when a sufficient amount of gas had been removed, the three-component structure would be disrupted and gas density in the disk would drop, eventually allowing gas to be ram-pressure stripped directly from the disk. This might account for the sharp increase in the net outflow at the end ($t \sim 12.8$–$13.6$ Gyr, see Fig 5.1).

## 5.4 Gas Loss from Fornax

In summary, we propose the following outline for gas dynamics in Fornax as it orbited the MW. Tidal interaction was responsible for removing $\sim 1/3$ of its original CDM. Because collisionless CDM does not suffer ram pressure, the CDM lost during Fornax's first orbital period appeared to have stayed close to the orbit and kept the simultaneously-lost gas from dispersing. This was crucial to the reaccretion of some of the lost CDM and gas as the Roche sphere expanded near the end of this period. Subsequently, there was no significant clustering of CDM near the orbit and once ram-pressure-stripped gas moved outside the largest Roche sphere of $\sim$ 12 kpc in radius, it was lost from

Fornax. We note that although the change in the Roche-sphere radius from $\sim 10$ kpc at the perigalacticon to $\sim 12$ kpc at the apogalacticon appeared small, the corresponding change in the Roche-sphere volume was by a significant factor of $\sim 1.7$. The non-monotonic evolution of net gas outflow for $t \approx 8.6$–$13.6$ Gyr might have resulted because an expanding Roche sphere would oppose while a shrinking one would enhance the effect of ram pressure. This would explain the coincidence of $\Delta F \sim 0$ at $t \sim 11.2$ Gyr with the transition from an expanding Roche sphere to a shrinking one (Fig. 5.1).

Gas loss from satellites through ram-pressure stripping and tidal interaction was studied in detail by simulations of [18], who emphasized the importance of the UV background in keeping the gas widely distributed inside the satellites. Gas depletion in Local Group dwarfs was studied analytically by [34], who emphasized heating of gas by stellar feedback. In general accord with these detailed studies, we propose that gas in the star-forming disk was first heated by SNe to $T_{\rm hot} \sim 5 \times 10^5$ K, and then escaped to be dispersed outside the disk before getting removed from Fornax. It is also possible that heating by both SNe and the UV background was needed, but we focus on SN heating below.

Using the same initial mass function as adopted by [9] in deriving the SFR and assuming that stars of 8–120 $M_\odot$ result in SNe, we obtain an SN rate of $R_{\rm SN}(t) \approx 10^{-2}\psi(t)/M_\odot$. For SNe to heat a total mass $\Delta M_{\rm hot}$ of gas that escaped during an episode of outflow, the required efficiency per SN is

$$\epsilon_{\rm SN} \sim \frac{(\Delta M_{\rm hot}/m_p)kT_{\rm hot}}{\Delta N_{\rm SN} E_{\rm expl}} \sim 0.083 \left(\frac{\Delta M_{\rm hot}}{10^7\,M_\odot}\right) \left(\frac{T_{\rm hot}}{5\times 10^5\ {\rm K}}\right) \left(\frac{10^4}{\Delta N_{\rm SN}}\right) \left(\frac{10^{51}\ {\rm ergs}}{E_{\rm expl}}\right), \tag{5.4}$$

where $\Delta N_{\rm SN}$ is the total number of SNe occurring in this episode and $E_{\rm expl}$ is the average explosion energy per SN. From the $\psi$ and $\Delta F$ shown in Figs. 3.1 and 5.1, respectively, we estimate that $\Delta M_{\rm hot} \sim 1.2\times 10^7\ M_\odot$ ($2.2\times 10^7\ M_\odot$) and $\Delta N_{\rm SN} \approx 6\times 10^4$ ($1.4\times 10^4$) for the episode of $t \approx 8.6$–$11.2$ Gyr (11.2–12.8 Gyr), which correspond to $\epsilon_{\rm SN} \sim 1.7\%$ (13%) for $T_{\rm hot} \sim 5\times 10^5$ K and $E_{\rm expl} \sim 10^{51}$ ergs. For the last episode of $t \approx 12.8$–13.6 Gyr, there was a sharp increase in the net outflow and $\Delta M_{\rm hot} \sim 8\times 10^6\,M_\odot$,

which would have required $\epsilon_{\rm SN} \sim 51\%$ with $\Delta N_{\rm SN} \approx 1.3 \times 10^3$. As noted in §5.3, for this terminal episode, gas could have been ram-pressure stripped directly from the star-forming disk due to the decrease in density. So a lower SN-heating efficiency could have been sufficient. Heating by Type Ia SNe, which is ignored in the above discussion, could also reduce the required $\epsilon_{\rm SN}$. Therefore, it appears that SN-heating coupled with ram-pressure stripping and tidal interaction for a few orbital periods was responsible for removing gas and terminating star formation in Fornax.

## 5.5 Simulations of Outflow in Dwarf Galaxies

Based on the SFH of Fornax dSph and guided by its proper motion, We constructed the tailored outflow dominated gas dynamics history for Fornax dSph in its satellite phase. Here we briefly reviewed some of the current simulation results on gas outflow in a more general settings of dwarf galaxies [17] [35] [36].

First of all, let us define Using the mass-loading efficiency (the ratio between wind mass loss rate and SFR) as

$$\eta_{\rm w} = \frac{\dot{M}_{\rm w}}{\Psi}. \tag{5.5}$$

Generally, there are two approaches to estimate $\eta_{\rm w}$, both of which takes the assumption that the wind speed $v_{\rm w}$ scales with the one-dimensional velocity dispersion $\sigma$. And one approach is based on the momentum observation of the driven wind [35] [17]. The momentum of the winds is the same as the input momentum

$$\dot{p} = \dot{M}_{\rm w} v_{\rm w}. \tag{5.6}$$

The input momentum come from the same models of stellar feedback as we shown in §2 including radiation pressure in the UV through IR, supernovae, stellar winds, and HII photoionization. Thus $\dot{p} \propto \Psi$, which leads to

$$\eta_{\rm w} = \frac{1}{\sigma} \tag{5.7}$$

$\eta_{\rm w}$ is as high as $\sim$ 10-20 from [17]. This number is also obtained in simulations of large dwarf galaxies$M_* \approx 10^8 M_\odot$, in which supernovae shock-heated gas dominate the production of large-scale outflows [17]. And it is consistent with our estimation during most of the time in the outflow dominated phase $\lesssim 20$. A detail picture of momentum driven wind is as followings: Momentum from UV photons, stellar winds and warm gas pressure from HII region stirs up star-forming regions, where SNe bubbles expand and overlap with each other. It results in a patchy star-forming regions and hot SNe bubbles. These bubbles ultimately push cold shells into super-wind as they overlap, which makes a warm/hot phase wind.

The second approach is called energy-conserving wind model [36]. The energy rate ejected by SNe is $\dot{E_{\rm SN}} \propto \Psi$ is used to drive the outflow, thus

$$\dot{E}_{SN} = \frac{1}{2}\dot{M}_{\rm w} v_{\rm w}^2. \tag{5.8}$$

Therefore, the mass-loading efficiency is

$$\eta_{\rm w} \propto \frac{1}{\sigma^2}, \tag{5.9}$$

which is more sensitive about the size of the system compared with the momentum driven wind model. It is consistent with the sensitivity evaluation of feedback mechanisms in different system as we discussed in §2. In small dwarf galaxies, the energy deposit feedback is the key process, thus the energy-conserving wind model suits better. Consequently, the results show that the star formation in small satellites has generic episodic feature as well as a relatively long time scale due to the reaccretion of gas. The second feature causes some problem in reproducing the elemental abundance data [36]. However, in a realistic MW system, the interaction between satellite galaxies and MW may suppress or even quench the reaccretion. Thus the chemical evolution problem may be solved automatically after taking this factor into account.

As in our case, the size of Fornax dSph may fall closer to valid range of the energy-conserving wind model. And the gas phase of Fornax dSph would be influenced by MW

potential after it becomes the satellite galaxy. Ram pressure stripping will make the gas loss more easily, and the tidal force suppresses and enhances the process periodically, which has been discussed in the last section. Thus, the reconstruction of individual satellite dwarf galaxy as Fornax ultimately needs to put the subgrid physics model in a realistic simulation of its host galaxy.

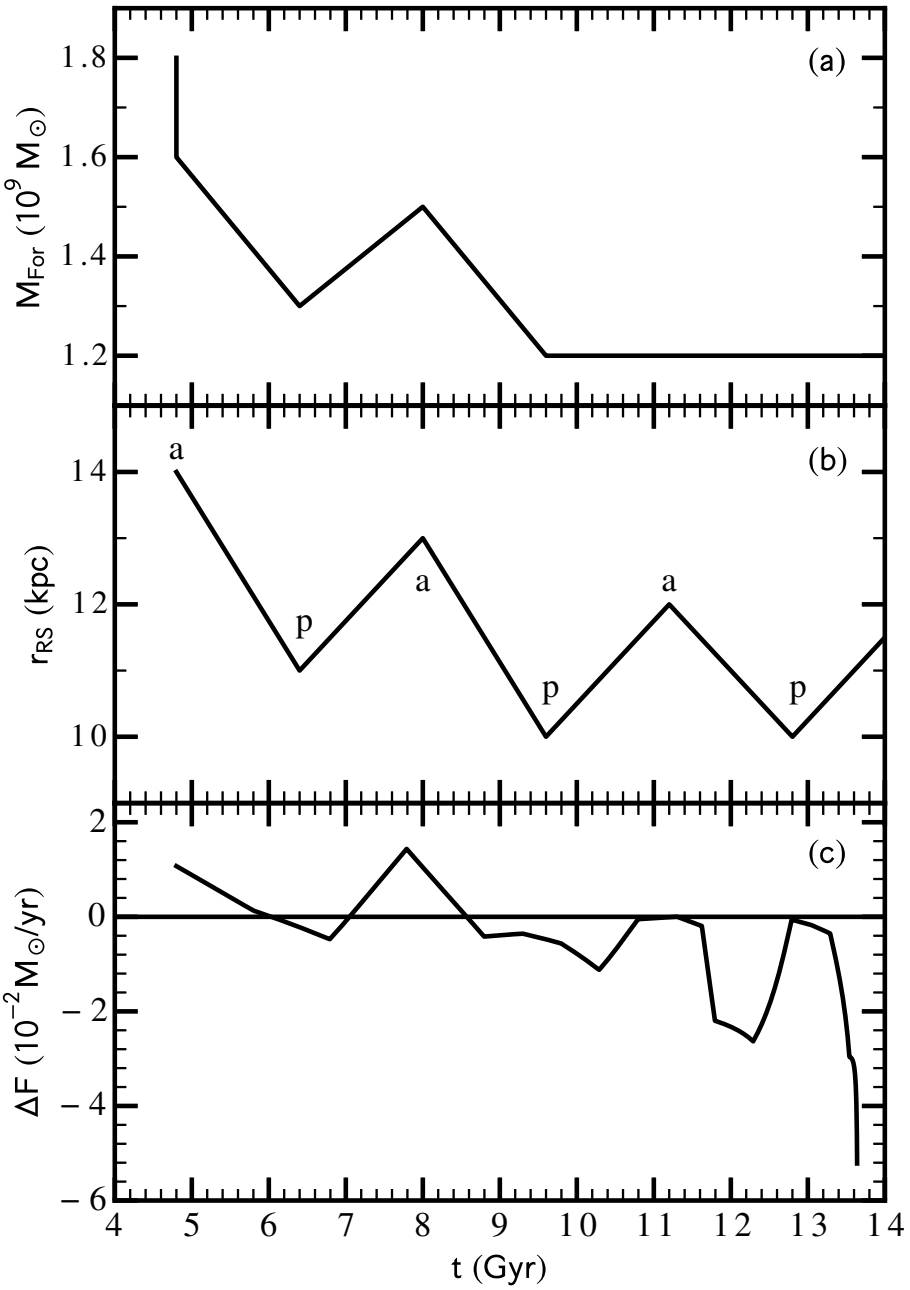


Figure 5.1: Evolution of the Fornax halo as an MW satellite at $t \gtrsim 4.8$ Gyr. Its total mass $M_{\rm For}$ (a) and Roche-sphere radius $r_{\rm RS}$ (b) are estimated at the apogalacticon (indicated by "a") and perigalacticon (indicated by "p"), and connected by line segments to guide the eye. For convenience of discussing the effects of tidal interaction, the relevant $\Delta F(t)$ for the baseline case (c) is also shown. See text for details.

# Chapter 6

# Supernovae Yields and Mixing Scenario

We already reached the first oder of understandings in the gas dynamics and halo evolution of Fornax dSph from §3,4&5. Before we are able to construct the chemical evolution model, we need to investigate how an individual SN enriches its surrounding ISM. Note that SN nucleosynthesis is the major source of heavy elements, and the only one we considered in our model. In this chapter, we showed the CCSN yields from [37] and SN Ia yields from [38] in §§6.1, which serve as the input of our model. Then we briefly summarize supernovae remnant (SNR) evolution in §§6.2 and give the estimations of mixing masses for both types of SNe. Finally, in §§6.3, we presented two examples of SN mixing implementation in dwarf galaxy simulations.

## 6.1 Supernovae Yields Study

We used the CCSNs yield table from [37] following the evolution and explosion of Population III stars with mass 10-100$M_{\odot}$. The code used to calculate stellar evolution and nucleosynthesis is KEPLER, which is a one-dimensional implicit hydrodynamics package. Due to the lack of robust explosion models, Supernova explosion is realized

by the input of a time-dependent momentum deposition, called a moving piston. And the explosion energy is defined as the kinetic energy at infinity, which is always smaller than the energy needed from the central engine. In our model, all the CCSNe within the mass range (10,30) $M_\odot$ and 20% of CCSNe within the mass range (30,100) $M_\odot$ explode successfully with different explosion energies as followings (see detail discussion of the settings in §7) ,

$$E_{cc}(m) = \begin{cases} 0.3B & , 9.6 \leq m/M_\odot \leq 10 \\ 0.6B & , 10 < m/M_\odot \leq 11.7 \\ 0.9B & , 11.7 < m/M_\odot \leq 13.3 \\ 1.2B & , 13.3 < m/M_\odot \leq 30 \\ 3.6B & , 30 < m/M_\odot \end{cases}$$

The mixing of material within a star is put into the stellar evolution code artificially, which is characterized by the mixing parameter $p_{\rm m}$. The mixing process is implemented by a running boxcar with width $\Delta M{=}p_m M_{\rm He}$ moving through a star for four times. $p_{\rm m}$ is set to be 0.01 for Population III stars, and 0.1 for all the others, with non zero initial metallicity, which is the case for the majority of stars. The setting aims to achieve the metallicity dependence of mixing process [37].

Here we first compare [$\alpha$/Fe] between SNe Ia and CCSNe yields. We set SNe Ia to have a uniform yield from W7 model from [38], which is shown as the blue dashed line. And CCSNe yields are presented in mass range 10-100$M_\odot$ with the energy and mixing dependence shown above. The black dots represent $[\alpha/{\rm Fe}]_{cc}$ of $p_m$=0.1, 0.01, respectively in Fig. 6.1 & 6.2. The IMF averaged [$\alpha$/Fe] of $p_m$=0.1 is shown as the red dotted line. In Fig. 6.1 all the $\alpha$ elements have large scatters of [$\alpha$/Fe] in mass range of 10-30 $M_\odot$ except for Ti. And as the stellar mass increases, [Si/Fe] and [Mg/Fe] also increase significantly in the mass range of 30-100 $M_\odot$. The increase of [Ca/Fe] is quite mild. Whereas [Ti/Fe] remains to be almost flat in the entire mass range. In Fig. 6.2, scatters of [$\alpha$/Fe] are generally larger in the mass range of 10-50 $M_\odot$, since low mixing brings less Fe to outer layers. It is the same reason why [$\alpha$/Fe] shoots over the upper

limit $\sim$ 2.0, in the mass range of 50-100 $M_{\odot}$. Basically, there is negligible amount of Fe produced in those stars as shown in Fig. 6.3, which represents the relative ratio of yields between two mixing scenario as $\rho_{cc} = Y_{cc}(p_m = 0.01)/Y_{cc}(p_m = 0.1)$. We may able to see stars with extremely high [$\alpha$/Fe]$\gtrsim$ 2, if they were born out of Population III star remnants without touching by other SNe and the extreme low [Fe/H]$\lesssim$ -8 can be measured. Combining these criterion makes the observations almost impossible, thus we only see stars with the highest [$\alpha$/Fe]$\sim$0.5 in local group including Fornax dSph (see Fig. 7.3). In Fig. 6.4, we compare the absolute Yields of SNe Ia and CCSNe of $p_m = 0.1$. The blue dashed line and the red dotted line represents SN Ia yields and IMF averaged CCSNe yields, respectively. We can see clearly for an individual SN event, the absolute amounts of $\alpha$ elements produced by SN Ia are about the same with those by CCSN within several factors $\lesssim$ 10. And SN Ia produced Fe is about 10 times larger than that from CCSN. However, SNe Ia explosions are universally rarer events, and the contributions from these two sources need to be evaluated in individual system considering the relative frequency ratio, as we will show in Fig. 7.2 from §7.

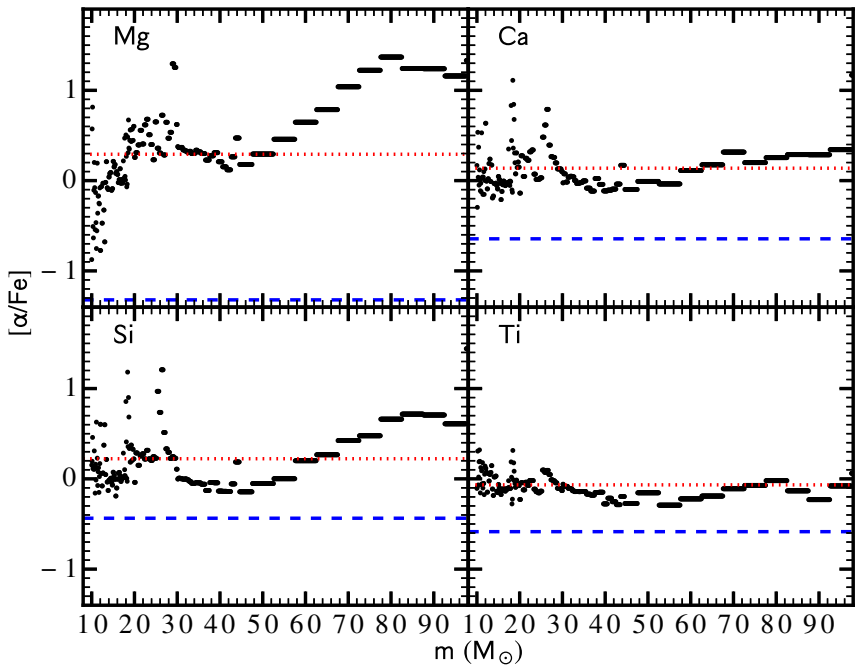


Figure 6.1: [$\alpha$/Fe] vs. [Fe/H] from SN Ia yields and CCSN yields of high mixing case ($p_m$=0.1). The black dots represent the yields from CCSNe in the mass range 10-100 $M_\odot$. And the blue dashed line indicates the yields of SNe Ia. The red dotted line represents the IMF averaged CCSNe yields.

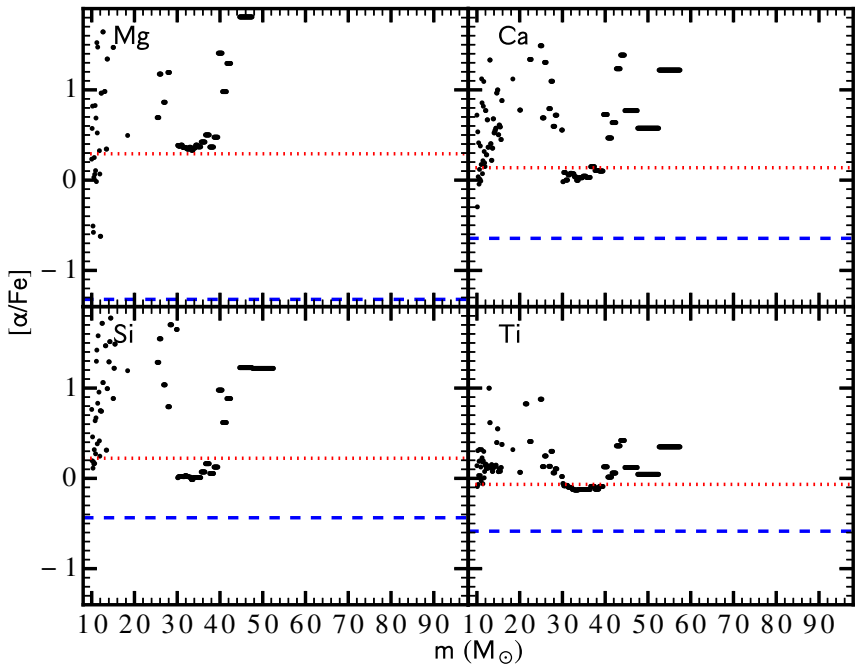


Figure 6.2: [$\alpha$/Fe] vs. [Fe/H] from SN Ia yields and CCSN yields of low mixing case ($p_m$=0.01), with the same notation as Fig. 6.1

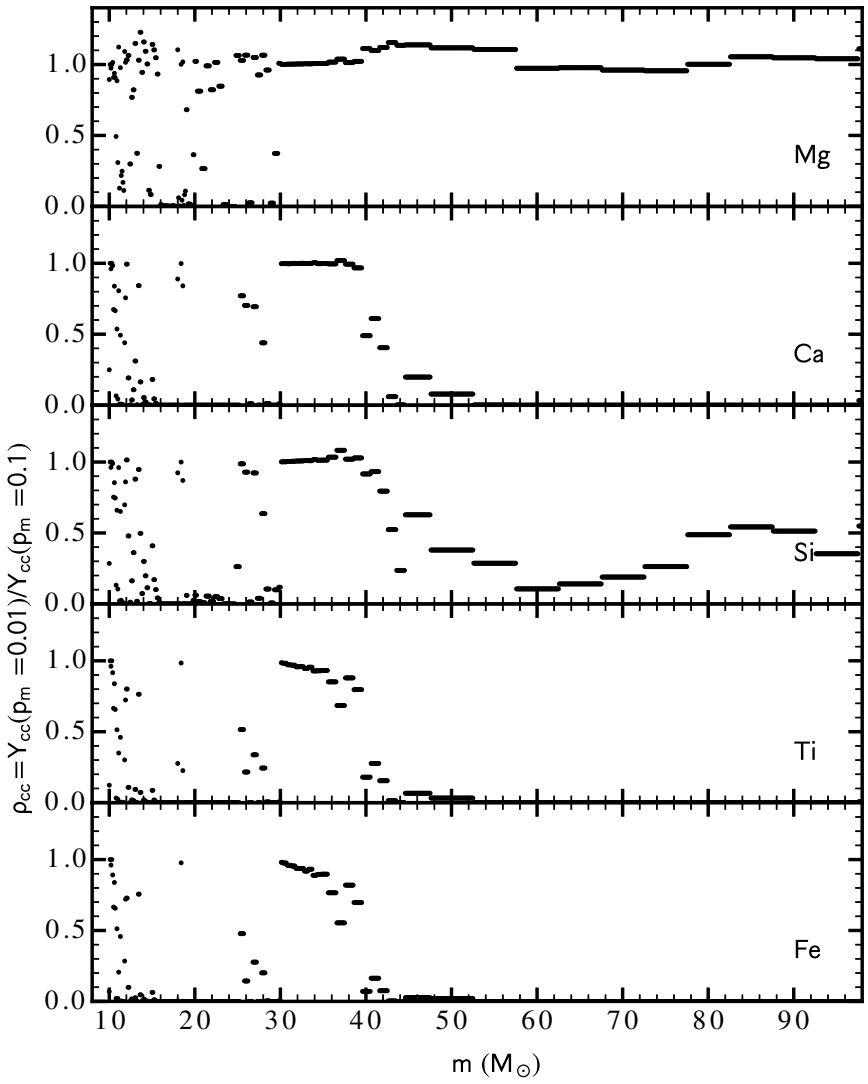


Figure 6.3: The relative ratio of CCSN yields between low mixing ($p_m$=0.01) and high mixing case ($p_m$=0.1)

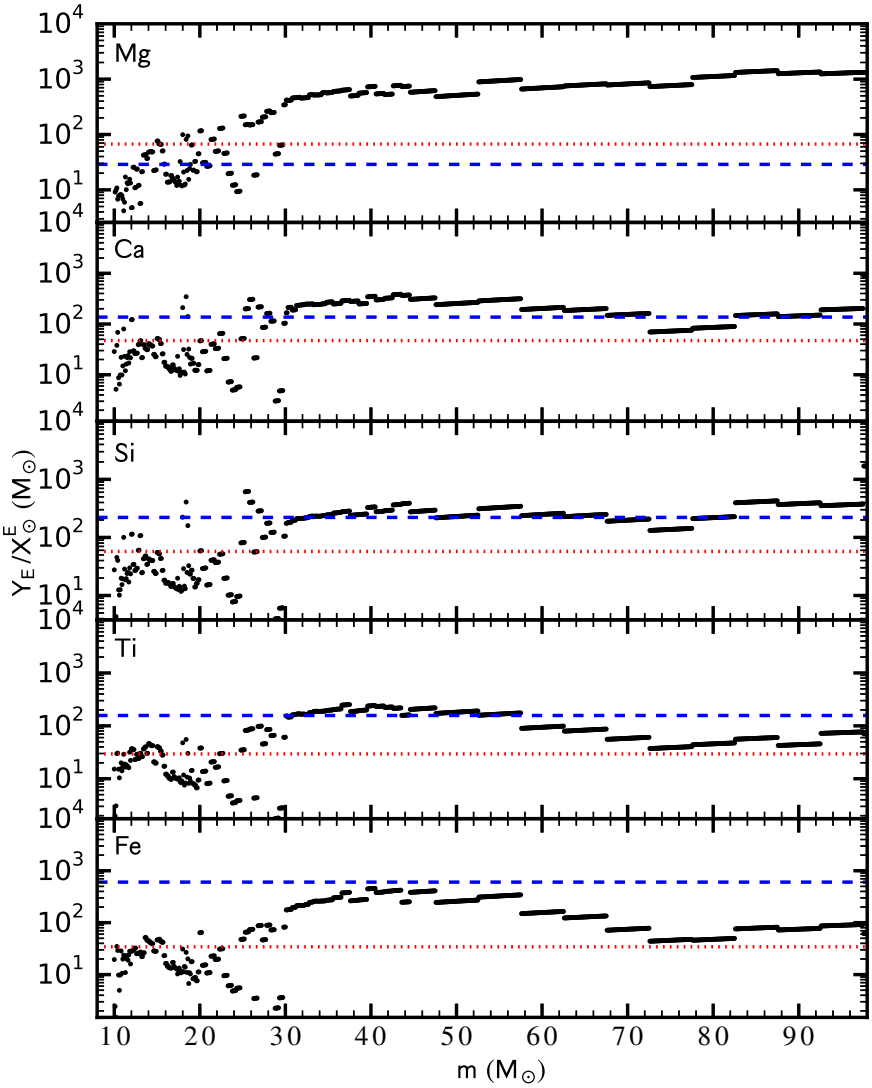


Figure 6.4: Comparison between SN Ia yields and CCSN yields of high mixing case ($p_m$=0.1), with the same notation as Fig. 6.1

## 6.2 Supernovae Remnants Evolution

Thornton et al [39] did numerical studies on how supernovae remnant evolves in the ISM. After SN explosion energy is injected locally, a hot SN bubble forms and adiabatically expands initially. As the temperature of the bubble drops, the shock front gradually slows down. Cooling at the shock front becomes very efficient, and a thin shell begins to form. As gas density increases and the shell gets thicker, cooling is enhanced, which produces the catastrophic cooling. In this stage, the kinetic energy of the hot bubble converts into thermal energy and gets radiated away right away. As supernovae remnant evolves, shell cooling becomes less efficient as the shell becomes thicker and density decreases. Eventually, supernova remnant will become part of the ISM.

Recalling the standard picture of ISM discussed in §2, gas collapses into molecular clouds with several layers of different temperatures. Each cloud is about the mass scale of $10^3 M_\odot$. As a SN shock front expands, it encounters the clouds nearby. those clouds get evaporated in supernova remnant where metal mixing take place throughly in the hot interior. And in Myr timescale, the next generation of clouds form out of the supernova remnant, which becomes more metal enriched compared with the last generation. The detail simulation of mixing process is beyond our paper. Instead, we take a simple empirical prescription of mixing in our model.

As one SN explodes, it dumps heavy elements of mass $Y_E$ as representative of different species, and injects energy $E_{\rm sn}$ into the surrounding ISM. We assume that all the metals including the newly synthesized and original stuff, are mixed up within mixing mass $M_x$, which correlates to the hot bubble mass directly. And the mass of different regions of a SN bubble can be calculated from the following empirical equations [39]. For $[E/H] < -2$,

$$M_r = 5.23 \times 10^4 E_{51}^{6/7} n_0^{-0.24} M_\odot \tag{6.1}$$

$$M_s = 4.89 \times 10^4 E_{51}^{6/7} n_0^{-0.24} M_\odot \tag{6.2}$$

$$M_b = 0.34 \times 10^4 E_{51}^{6/7} n_0^{-0.24} M_\odot. \tag{6.3}$$

$M_r$, $M_s$ and $M_b$ represents the remnant, shell and hot bubble mass, respectively. As we can see that about 90% of the remnant mass is within the cold and dense shell. For $[E/H] > -2$,

$$M_r = 1.44 \times 10^4 E_{51}^{6/7} n_0^{-0.24} Z^{-0.28} M_\odot \tag{6.4}$$

$$M_s = 1.41 \times 10^4 E_{51}^{6/7} n_0^{-0.24} Z^{-0.27} M_\odot \tag{6.5}$$

$$M_b = (1.44 \times 10^4 Z^{-0.28} - 1.41 \times 10^4 Z^{-0.27}) E_{51}^{6/7} n_0^{-0.24} M_\odot. \tag{6.6}$$

SN ejecta is dumped into the hot bubble and metal is well mixed within it at first. Eventually, the bubble loses its structure and mixes with the surrounding cold ISM. However, we have little idea how far the ejecta can travel before cooling down completely. Rough estimation gives $M_b = 10^3 \sim 10^4 M_\odot$ and $M_s = 2.6 \times 10^4 \sim 2.3 \times 10^5 M_\odot$, for $Z = 0.1$, $n_0$=1 cm$^{-3}$ $\sim 10^{-4}$ cm$^{-3}$. Since the bubble mass also depends on the gas density, the different explosion sites also brings different mixing masses. CCSNe almost explode instantaneously ($\lesssim$ Myr) after their progenitor stars are born. So explosions usually happen in a star forming region with high gas density. Whereas SNe Ia take $\sim$ 1 Gyr to evolve. When they explode, typically, the original GMCs they resided have been disrupted by more frequent CCSNe explosions. Thus their explosion sites are mostly in secluded place with low gas density. It leads to $n_{\rm ISM,Ia} \ll n_{\rm ISM,cc}$ and thus $M_{\rm x,Ia} \gg M_{\rm x,cc}$. Thus we set $M_{\rm x,cc}$ and $M_{\rm x,Ia}$ differently in our model. When the system is dominated by outflow, SNe bubbles can not survive for long, which suggests inefficient mixing. We set $M_x \sim M_b$ as the mixing case in the satellite phase of our model. When the system keeps accreting inflow in the pre-satellite phase, the cold high density gas collapse from the outer skirts. At the same time, SN bubbles keep forming from the star formation region. Both mechanisms work on the system, which would

drive significant galactic scale turbulents [40]. Thus in this case, the mixing process is much more thouroughly. The evaluation of metal mixing in these two scenarios needs galaxy evolution code with GMC scale resolution. In this paper, motivated by the observations signatures, we empirically set the mixing mass as discussed in §7.

## 6.3 Simulations of SN enrichment in Dwarf Galaxies

As we already discussed, how to mix SN products in ISM is a complicated problem. Without high resolution simulations, it is usually implemented empirically in galaxy evolution model. Here we summarize two papers [36] [41] which simulated field dwarf galaxies in MW-like system and studied their chemical evolution history.

From the study on the satellites propertities in galaxy formation simulations [36], if SN explodes in one particle (Each particle represents a simple stellar population, $m_* \sim 10^5 M_\odot$), the energy, metal and mass is evenly distributed amongst its 32-128 neighbouring gas particles. The fraction of each quantity received by a particle is $m_i/\Sigma_j m_j$, where $m_i$ is the mass of the particle where SN takes place, and the subscript $j$ runs over all neighbours. In this case $m_{\rm mix} \sim 10^6 - 10^7 M_\odot$. They only compare the averaged values of [O/Fe] vs. [Fe/H] in different halo models compared with MW satellites without considering the scatter pattern. And the efficient SN mixing mass they chose is large enough to make the system in a homogeneous state quite easily. Whereas in our case, in order to match the abundance pattern in a individual dSph, more careful assessment of SN mixing is needed.

Following the same approach, [41] implement the mixing process using a more sophisticated subroutine, which is called a simple diffusion model. Each gas particle in their model has mass $m_* = 6000 M_\odot$. The newly produced metal are distributed within 32 neighboring particles. However, the metallicity of newly-formed star particle is obtained by averaging the metallicity over 128 neighborng gas particles, which is about

$6 \times 10^5 M_\odot$. This procedure can solve the problem of large scatter of [$\alpha$/Fe] from simulations compared to observations at the early stage of chemical evolution. It is equivalent to the enhanced mixing in the first phase of our model ( see §7). Their model can reproduce the data in Milky Way thin disk, thick disk and halo stars. We suggest that most galaxies went through the inflow dominated phase at its early evolution when DMHs were in the fast-growing phase [19], and during that epoch, the enhanced SN mixing is a universal phenomenon.

# Chapter 7

# Chemical Evolution Model for Fornax dSph

Fornax dSph is about 1000 times smaller than MW, and it has prolonged SFH, which just ends million years ago. It maybe counter intuitive to see that it is much more inhomogeneous than MW, after both systems evolve about the same amount of time. Similar situations can be seen in other dwarf spheroidal in local group from [42]. Here, we use a simple argument to explain the relation between the scale and homogeneity of a gaseous system. In any Schmidt SFL $\Psi \propto M_g^{\alpha}$, $\alpha$ is almost always larger than 1 from observations. Let us assume that, the number of SNe from unit stellar mass $f_{\rm sn}$ and SN mixing mass $M_x$ are universal constants in different systems. And we define the rate of gas mass fraction enriched by SNe as $f_p$,

$$f_p = f_{\rm sn}\Psi M_x/M_g \propto f_{\rm sn} M_x M_g^{\alpha-1}, \tag{7.1}$$

where $f_{\rm sn}$ is the number of SNe per unit mass. As long as $\alpha > 1$, we always get $f_p \propto M_g$, which leads to the conclusion that the larger the system is, the quicker it would reach homogeneous. And if we substitute $M_x$ with averaged SN yield $Y_{\rm sn}^E$ of element $E$, we

get the enrichment rate of the system as

$$f_e = f_{\rm sn}\Psi Y^E_{\rm sn}/M_g \propto f_{\rm sn}Y^E_{\rm sn}M_g^{\alpha-1}. \tag{7.2}$$

Similarly, $f_e \propto M_g$, which explains why MW is more metal enriched than Fornax and other dwarfs [42]. Starting from this relation, we build a chemical evolution model for Fornax dSph and compare with the observational data in several aspects, the element abundance pattern [$\alpha$/Fe] vs. [Fe/H], metallicity distribution function (MDF) of Fe, Ca, Mg and their metallicity evolution as a function of time. As we have already seen, the key free parameter in our model is $M_x$, which is estimated from §6. The organization of this chapter is as followings: The general setup of our model is presented in §§7.1. Then, we list the parameter settings in §§7.2 and show the setup of time and space in detail in §§7.3 & §§7.4. In §§7.5, we discussed the observational motivations and physics pictures of the key parameters. Finally, we show the comparisons between the results of our model in different settings and the observational data in the last section §§7.6.

## 7.1 2-D Mass Grid Model

The simulation is performed on a 2-D, $n = 1000^2$ mass grid. The motivation of this setup comes from the fact that the star formation region of dwarf galaxy is disky originally, before tidal disruption. The number of gas boxes on the grid changes, as the gas mass of the system. During each timestep $\delta t$=0.2 Gyr, I randomly pick a certain number of boxes as SNe sites, according to the number of SNe exploded in $i$ th timestep ($n_{cc,i}$ & $n_{Ia,i}$). $n_{cc,i}$ can be calculated by the universal IMF from [43] based on the SFH. Each CCSN is characterized with progenitor mass, explosion energy and mixing parameter [37], shown in §6. For SN Ia, we use a standard delay time distribution (DTD) [44]. And the equivalent rate ratio between SN Ia to CCSN $k$ is adjusted to fit the data. Both types of SNe would inject their products of heavy elements into the surrounding gas boxes. The mixing process is carried out empirically. SN mixing mass $M_x$ is set artificially within estimated range, which is discussed in §6.

We assume all the inflow gas is metal free in Phase I (pre-satellite phase), which comes into the system as fresh gas boxes. In Phase II (satellite phase), Inflow is purely metal free before it touches zero around $t$ =6 Gyr. Whereas after the first episode of outflow, the system regains some gas which has come to the system earlier. These gas would be already touched by SN, but the enrichment is marginal since it has only stayed for a brief period. Thus when these gas come to the system again as the last episode of inflow, it is metal poor instead of metal free, the metallicity of which is calculated automatically in our model. As for the outflow, we simply drop the gas boxes. This implementation is modified to an enhanced metal loss version in Phase II, guided by the hints from elemental abundances data.

After the treatment of gas flow is done. I again randomly sample $n_{s,i}$ boxes, which is the number of stars surviving today in the $i$th timestep, calculated from the SFH. Stars born out of these boxes record their local metallicity in that timestep. The same procedure is done for the entire SFH. The metallicity information of the whole system is taken as a snapshot at the end of each timestep. We can easily plot the metallicity evolution as a function of time, by combining all the snapshots. MDFs are generated by summing up all the stars surviving until today. Similarly, these stars with birth time and elemental abundance information are put in the [$\alpha$/Fe] vs. [Fe/H] plot. By the comparisons between the generated data and the observations, we fix the parameter settings shown in the next section §§7.2.

## 7.2 Parameter Settings

Here we listed the key parameters of this model. The choices are guided by the comparisons between observations and simulations, which is discussed in detail in §§7.5.

(i) We use the SFL of a growing star forming disk, $\Psi = \lambda_*(t) M_g^{1.5}$, where $\lambda_* \sim 1/r_{\rm vir}$ (see the halo model in 4) and $\lambda_*(t_{\rm sat}) = 0.8 \times 10^{-14} M_\odot/yr$. The choice of $\lambda_*(t_{\rm sat})$ gives us the right amount of gas mass to carry out chemical enrichment. For a system with

known SFH, the total amount of heavy element put into the system is fixed, whereas the total gas amount is varied by $\lambda_*$, as we already discussed in §3, . Thus it is the key parameter of determining the average metallicity of the system, such as the peak position of $\mathrm{MDF}_E$ and [E/H] vs. t.

(ii) We assume all the CCSNe have mixing parameter 0.1, except that those born from metal free material (Z=0) have mixing parameter 0.01. CCSNe within the mass range (10,30) $M_\odot$ explode successfully with explosion energy from 0.3B to 1.2B. And 20% of CCSNe within the mass range (30,100) $M_\odot$ explode with explosion energy $E = 3.6B$. (see detail in §6)

$$R_{cc}(t) = \int_{10}^{30} \phi(m)\psi(t)\mathrm{d}m + 0.2\int_{30}^{100} \phi(m)\psi(t)\mathrm{d}m, \tag{7.3}$$

where $\phi(m)$ represents the universal IMF from [43].

$$\phi(m) \propto m^{-\alpha} \tag{7.4}$$

where

$$\alpha = \begin{cases} 1.3 & , 0.08 \leq m/M_\odot \leq 0.5 \\ 2.3 & , 0.5 \leq m/M_\odot \end{cases}$$

(iii) SN Ia physics comes with two key parameters. One is the characteristic delay timescale $\tau_{Ia}$, taking $\mathcal{D}(\tau)$ from [44] as DTD.

$$\mathcal{D}(\tau) = \begin{cases} 0 & , \tau < \tau_{Ia} \\ \propto \tau^{-1.1} & , \tau \geq \tau_{Ia} \end{cases}$$

$\tau_{Ia}$ varies between 0.42 Gyr to 2.4 Gyr [44], and we take $\tau_{Ia} = 1Gyr$ in our model. Another SN Ia parameter is the equivalent rate ratio of SN Ia to CCSN, $k$, which controls the relative contributions from SN Ia compared to CCSN through the following relation

$$R_{Ia}(t) = k\int_{\tau_{Ia}}^{t} R_{cc}(t-\tau)\mathcal{D}(\tau)\mathrm{d}\tau. \tag{7.5}$$

The main effect of $k$ is determining the slope of scatter in [$\alpha$/Fe] vs. [Fe/H] plots in the pre-satellite phase (see detail discussion in §§7.5). We set k=1/5 in this model.

(iv) As we already discussed in §6, The distinct environments would result in the different mixing mass, as $M_x \propto n^{-0.24}$ from Eq.6.3. We set the mixing mass ratio of SN Ia to CCSN as $M_{x,Ia}/M_{x,cc}$ ∼5 throughout the history, corresponding to the ratio of gas density between the two environments roughly as $n_{Ia}/n_{cc}$ ∼1/1000, which is about the ratio of $n_{\rm warm}/n_{\rm hot}$. As the system transits from a inflow dominated phase to a outflow dominated phase, SN mixing mass also changes. We set $M_{x,Ia} = 10^5 M_\odot$, $M_{x,cc} = 2 \times 10^4 M_\odot$ in the pre-satellite phase, and $M_{x,Ia} = 5 \times 10^3 M_\odot$, $M_{x,cc} = 10^3 M_\odot$ in the satellite phase (see detail discussion in §§7.5).

(v) Enhanced metal loss in outflow is achieved by introducing the efficient enrichment factor $\eta$ for both type of SNe. After Fornax becomes the satellite of MW,

$$p_{cc}(t) = \eta_{cc} Y_{cc} R_{cc}(t) \tag{7.6}$$

$$p_{Ia}(t) = \eta_{Ia} Y_{Ia} R_{Ia}(t) \tag{7.7}$$

where $\eta_{Ia} = 1/4$ and $\eta_{cc} = 1/2$. We assume that metals from SNe Ia get lost more due to the same enviromental reason as (iv). Without the modification, the elemental abundances will be over estimated in the satellite. The careful comparison is shown in §§7.6.

## 7.3 Time setup

In order to numerically implement the chemical enrichment process, we need to discretize time and space. Let's focus the discretization of time in this section. SFH begins at $t_s = 0.29 Gyr$ as the first bin in SFH and the timestep is chosen to be $\delta t = 0.2 Gyr$. The gas mass in each timestep is defined to be the value at the end of it.

$$M_{g,i} = M_g(t_i), \tag{7.8}$$

The numbers of SN and newly born stars are calculated by integrating over each timestep. We only select the stars surviving today as the output of the model.

$$n_{s,i} = \int_{t_i}^{t_i+\delta t} \Psi(t)\mathrm{d}t \int_{0.1}^{m_{max}} \frac{\phi(m_\tau)}{N_m}\mathrm{d}m, \tag{7.9}$$

where the normalization factor is calculated as below,

$$N_m = \int_{0.1}^{0.5} m^{-0.3}\mathrm{d}m + 0.5\int_{0.5}^{100} m^{-1.3}\mathrm{d}m. \tag{7.10}$$

And $m_{max}$ is obtained from empirical equation [45]. Since the SFH ends before 0.04 Gyr ago,

$$m_{max} = 10^{7.764-\frac{1.790-(0.334-0.1116\log\tau_m)^2}{0.2232}}, \tag{7.11}$$

when $\tau_m = t_0 - t > 0.04Gyr$. The number of CCSN explosions $n_{cc,i}$ as well as SN Ia explosions $n_{Ia,i}$ can be obtained from

$$n_{sn,i} = \int_{t_i}^{t_i+\delta t} R_{sn}(t)\mathrm{d}t. \tag{7.12}$$

The amount of gas inflow and gas outflow is calculated similarly

$$m_{in,i} = \int_{t_i}^{t_i+\delta t} F_{in}(t)\mathrm{d}t, \qquad m_{out,i} = \int_{t_i}^{t_i+\delta t} F_{out}(t)\mathrm{d}t. \tag{7.13}$$

## 7.4 Space Setup

The discretization of space is done in this way. We assume each gas box contains a constant mass $m_0$, defined by the maximum gas mass amount.

$$m_0 = M_{g,max}/n \tag{7.14}$$

It means when the system reaches its peak amount, the gas occupies the entire grid with $n = 1000^2$ boxes. Thus, in $i$th timestep, the number of gas box is

$$n_i = M_{g,i}/m_0 \tag{7.15}$$

In our model, the gaseous region would be a square with side length $l_i = \mathrm{int}(\sqrt{\mathrm{n_i}})$. As the system expands, $l_i$ increases as the new boxes are added to the outskirt of the grid, which contains metal free gas by default. And when the system shrinks, $l_i$ decreases as boxes are dropped out of the grid. The difference between $\sqrt{n_i}$ and $\mathrm{int}(\sqrt{\mathrm{n_i}})$ is negligible when the mass resolution is fine enough, which is determined by the box number of the grid. When a SN explode in a random cell, metallicity of the neighboring cells within $n_e = M_x/m_0$ would change as

$$Z'_{E,i} = \frac{m_0 \sum_{i}^{n_e} Z_{E,i} + Y^E_{sn}/X^E_{\odot}}{M_x} \tag{7.16}$$

where $i$ runs over $n_e$ closest cells to the explosion cell.

## 7.5 Discussion

In this section, we explicitly show the motivation of the choice of the key parameters from §§7.2 and how to build the chemical evolution model consistently with the gas physics. All setup is based on the underlying picture of gas dynamics and guided by its imprint in the generated metallicity abundances data.

Phase $I$ (pre-satellite phase): $t_s < t < t_{sat}$, the system grows rapidly as more and more gas boxes added to it. Since SN explosion is the only mechanism of metal mixing in our model, the newly accreted gas remains to be metal poor before sufficient number of explosions happened nearby. Stars born from the newly accreted gas have much lower metallicity than the stars born from the earlier accreted gas. It comes out as the large scatter on the metal poor side in [E/H] vs. t plot when the system grows. This feature is clearly observed at least for the best measured element Fe (see Fig. 7.4). On the other hand, SN mixing needs to be quite efficient to make the correlations between $\alpha$ elements and Fe converged in this phase, shown in Fig. 7.3. Since SN Ia has larger mixing mass than CCSN, as we assumed, it is the major mixer of the system. Thus we set $M_{x,Ia} = 10^5 M_{\odot}$ to create the converging tip at the end of this phase. We also notice

that the oldest generation of stars ([Fe/H]$\lesssim$ -2) with blue shades in Fig. 7.3 have the largest scatter of [$\alpha$/Fe] ( $\sim$ 0.8 dex). It can be easily understood because the system starts from the most inhomogeneous state at the beginning of SFH. And the scatter scale is determined by both the intrinsic CCSNe yields table from §6 and $M_{x,cc}$. We notice that the upper bound of [$\alpha$/Fe] $\sim$ 0.6 is well within the upper limit [$\alpha$/Fe] $\sim$ 1.0 from CCSNe yields pattern in mass range (10 - 30 $M_{\odot}$). It should be straightforward to achieve the observed scatter pattern by the adjustment of $M_{x,cc}$, which we set to be $2{\times}10^4 M_{\odot}$.

SN mixing mass here refers to the efficient mixing mass instead of the exact hot bubble $M_b$ or shell mass $M_s$ in each SN bubble. However, the estimations of both $M_b$ and $M_s$ give us a reasonable range to tune $M_x$ [39] (see detail calculations in §6). Due to the continuous inflow during this period, pressure is exerted on the hot gas phase by the piled up cold gas from outskirts. Although CCSNe keep exploding at the center star forming region, there is little chance for the hot gas to escape from the high pressure on the top. The explosions deposit both energy and momentum to the ISM, which heats up the gas and drives significant turbulence in the entire system. The first feedback mechanism makes cooling less efficient when the hot gas accumulates and the average density decreases in the system. The second process disrupts SN bubble structure and suppress GMC collapsing. Overall, both processes lead to the enhanced SN mixing. Thus large mixing mass motivated by the observational data is consistent with the gas dynamics in this phase. The turbulence driven by the mass transportation of gas at the outskirts of the discs and the consequent metal mixing scenario has been studied numerically by [40].

We see strong declining trend in [$\alpha$/Fe] vs. [Fe/H] (Fig. 7.3) in the pre-satellite phase. The slope of this trend, shown clearly as the upper envelope of the scatter, is determined by the relative frequency ratio of SNe Ia to CCSNe, $k$. A significant amount of Fe enrichment from SN Ia would drag down the mean value of [$\alpha$/Fe] from $\sim$ 0.5 to $\sim -0.2$. Note that the choice of $t_{Ia}$ and $k$ is not unique. Here, we adopt the common

choice of $t_{Ia} = 1Gyr$, and tune $k$ by the comparisons between generated scatter pattern with the observed data.

Phase $II$ (satellite phase): $t > t_{sat}$, the inflow gradually drops all the way to 0 around $t = 6$ Gyr, and outflow comes up. There is a brief inflow episode from 7 to 9 Gyr, after the first outflow episode. And the system is dominated by outflow for the rest of the time. As inflow diminishes, the pressure exerted on the system gradually loses its power and the outflow finally gets the outlet. As the hot gas is able to escape from the system, and SN explosion energy is mostly used to drive the outflow (see outflow wind model in §5). Consequently, SN mixing happens more briefly, which is much less efficient compared to the first phase. The imprint of shrinking of mixing mass in data file is a large cluster of stars right after the converging tip in Fig. 7.3. The shades of the cluster transit from cyan (older) to red (younger), as [Fe/H] increases. It indicates that the local inhomogeneity by SN mixing manifest itself for the entire phase. We set $M_{x,cc} = 10^3 M_\odot$, and $M_{x,Ia} = 5 \times 10^3 M_\odot$, which is about the same as the hot bubble mass estimated by [39].

The reductions of SN enrichment are necessary in this phase. If we keep the same parameter set as Phase $I$, all the elements would be over produced, shown in Fig. 7.6 & 7.9. It suggests that the parameter sets should be different for these two phases. Such modification would probably get closer to the reality, since metals from supernovae remnant are easier to escape in outflow dominated environment. SN explosion heats up, pushes and enriches its surrounding ISM. The neighboring patches of gas are the receiver of both ejecta and explosion energy. Therefore, they have higher metallicity than the average ISM of the system and they are easier to escape. Thus the outflow is generally more metal enriched than the dropped gas boxes in our model, which have no relation to SN explosion sites. However, it is impossible to estimate the enhanced metal loss without detail hydrodynamics simulations. But we are able to reach this scenario empirically by the reduction of SN enrichment for CCSN as $\eta_{cc} = 1/2$. The contribution from SNe Ia would need extra reduction, simply because their explosion

sites are usually in diluted gas region. It takes longer for SNe Ia enriched gas to cool, which means that it has larger chance to be expelled. These gas gets heated by SNe Ia may never return to the cold ISM, and therefore does not get the opportunity to enrich the star forming gas region. Thus we compensate the extra loss by the reduction of SN Ia rates as $\eta_{Ia} = 1/4$.

## 7.6 Results

According to the parameter settings in §§7.2, we first compare the rate and enrichment contributions from two types of SNe. The solid line in Fig. 7.1 represents CCSN rate, which is always $\gtrsim 10$ times larger than SN Ia rate shown as the dashed line, except for the last 2 Gyr, when both rates diminish. Then we compare the SN production rate $p_{cc}$ and $p_{Ia}$, after taking account in the enhanced metal loss in Phase $II$, shown in Fig. 7.2 with the same notation as Fig. 7.1. $\alpha$ elements are mainly produced by CCSNe whereas Fe is made approximately equally from both. As we can see from the upper four panel of Fig. 7.2, the amount of Mg from SNe Ia is negligible. And SNe Ia contribution to Ca and Si is a little bit larger than that to Mg. The production percentage from SNe Ia is the largest for Ti, which weights approximately 1/3 of the total.

The comparisons between the results of our standard case (with parameter settings shown in §§7.2) and observations are shown in 7.3, 7.4 & 7.5. In Fig. 7.3, the space of center white, light grey and dark grey denotes $1\sigma$, $2\sigma$ and $3\sigma$ confidence region respectively for Mg, Ca and Si. We can see that the boundary between light and dark grey space (95% confidence region) includes most of the stars and outlines the overall shape of the scatter for these three $\alpha$ elements. For Ti, the mean trend is below most of the data points. And the confidence regions of $1\sigma$ is too narrow to show, thus we plot $2\sigma$ region as the white space and $3\sigma$ region as the dark grey band. This prolem may be due to both the average and variance of intrinsic Ti yield is underestimated. The upper envelope in 7.3 shows a clear declining trend and it converges around $[Fe/H] \lesssim -1.4$,

as the observational data in Phase $I$ suggests. The scatter regrows after the convergent tip, consistent with the shape of grey regions. The light grey region can cover almost all the stars in Mg plot, which is the best measured $\alpha$ element. Some stars sits in the dark grey region in Ca and Si plots, whereas these data points have quite large scatter $\gtrsim 0.3$ dex. The black solid line denotes $\langle[\alpha/\mathrm{Fe}]\rangle_{fe}$ of all the stars having close [Fe/H] within 0.1 dex interval. It directly reflects the simulation results, going through the middle of the white space. We can also get $\langle[\alpha/\mathrm{Fe}]\rangle_{t_i}$ of all the stars born at the same timestep, from $[\mathrm{E/H}](t_i)$. At any given time $t_i$, we plot $\langle[\alpha/\mathrm{Fe}](t_i)\rangle$ vs. $\langle[\mathrm{Fe/H}](t_i)\rangle$ as the dashed line in Fig. 7.3, which differs from $\langle[\alpha/\mathrm{Fe}]\rangle_{fe}$ vs. $\langle[\mathrm{Fe/H}]\rangle_{fe}$ clearly. The metallicity evolution of Ca, Mg and Fe is shown in Fig. 7.4. The solid line represents the mean of stellar metallicity at any given time as $\langle[\mathrm{E/H}]\rangle(t_i)$. The dashed lines show the upper and lower limits, which include 95% of stars. As we can see that the mean trend of all three elements go through the middle part of the data. For the best measured element Fe, low [Fe/H] stars $\lesssim$ -2 exist for the entire history, and at least they are within the 95% confidence region until $t \sim$8 Gyr. As we have discussed in §§7.5, the low metallicity boundary of our model is produced by the newly added boxes as inflow coming to the system, which perfectly explains the observational data. Finally, we show MDF for Mg, Ca and Fe in Fig. 7.5. All the peak position and the width of the generated MDF can match with that from observations very well.

We also present the results of different parameter settings, using the same model for comparisons. In Fig. 7.6, 7.7 and 7.8. We show the case without enhanced metal loss in Phase $II$. In 7.6, the scatter pattern for old stars mostly born in Phase $I$ can be matched similarly as the standard case. Whereas the lower boundary of [$\alpha$/Fe] is higher, which left some stars out of dark grey region, especially for Ca and Si. It is clearer to see that all the elements are over produced in Fig. 7.7 and 7.8. Then we show the case with metal loss for both $\eta = 1/2$, but without extra SN Ia rate reduction. Similarly, the over production of Fe is clearly shown in Fig. 7.11. In the last case, we present the results without adding the 20% CCSN in mass range (30,100) $\mathrm{M}_{\odot}$, and the

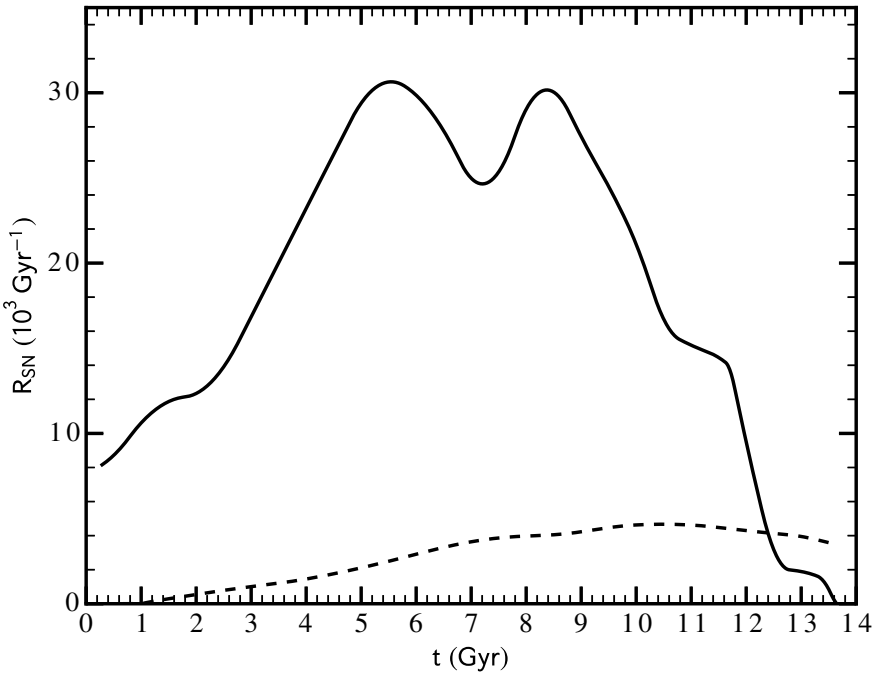


Figure 7.1: The comparison between CCSN rate (solid line) and SN Ia rate (dashed line) of our model. Note that the SN Ia rate here is not reduced in the satellite phase.

major effect is on Mg abundances. In Fig. 7.12, the scatter pattern of data is closer to the upper boundary, which suggests that Mg is under produced. And [Mg/H]($t$) as the solid mean curve is lower than most of the stars, shown in Fig. 7.13. More clearly in Fig. 7.14, the peak position of $\mathrm{MDF_{Mg}}$ is shifted to the left by 0.2 dex compared with the data. We notice that the absence of high mass CCSNe only has major effect on Mg. It is because these CCSNe would produce about 10 times of the IMF averaged amount in the entire mass range of (30-100) $M_{\odot}$, as shown in Fig. 6.4. Whereas the difference between high mass and regular CCSNe is much less for all the other elements.

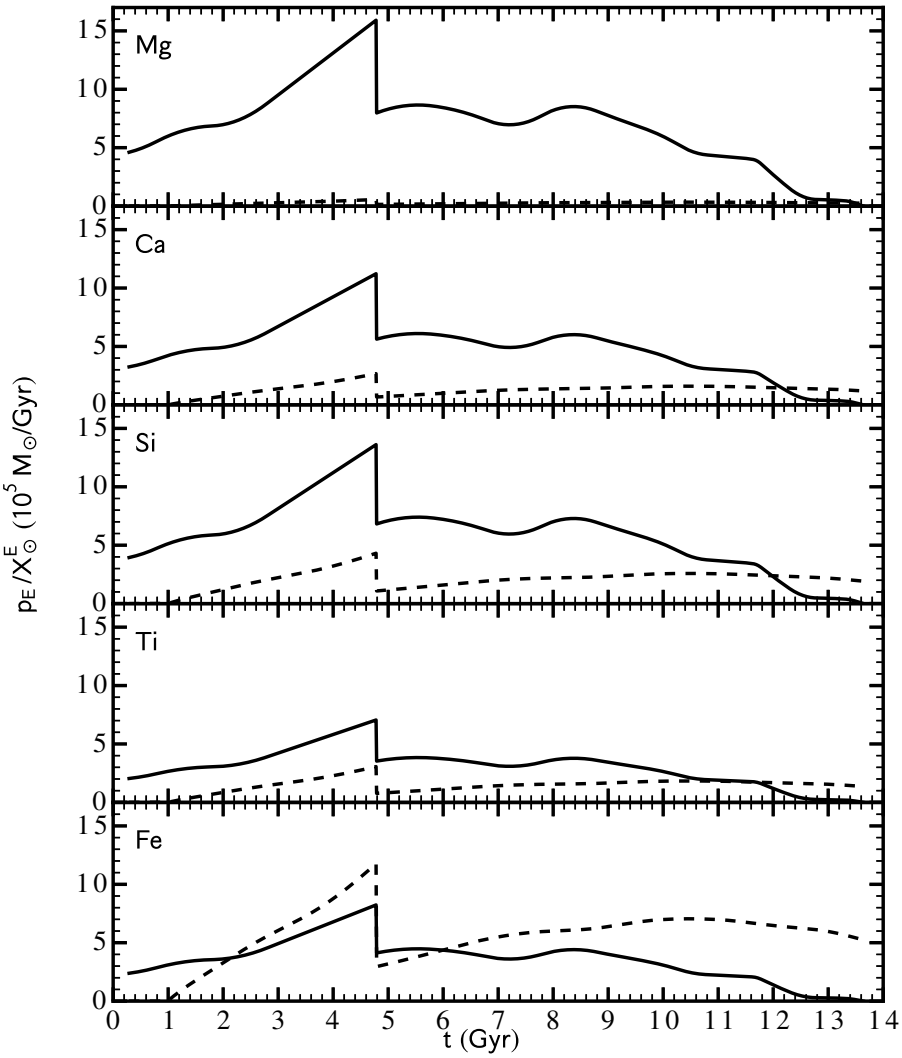


Figure 7.2: The comparison of heavy element production rate between CCSNe (solid line) and SNe Ia (dashed line) for Mg, Ca, Si, Ti and Fe. Note that the metal loss enhancement in the satellite phase is set as the standard case of our model.

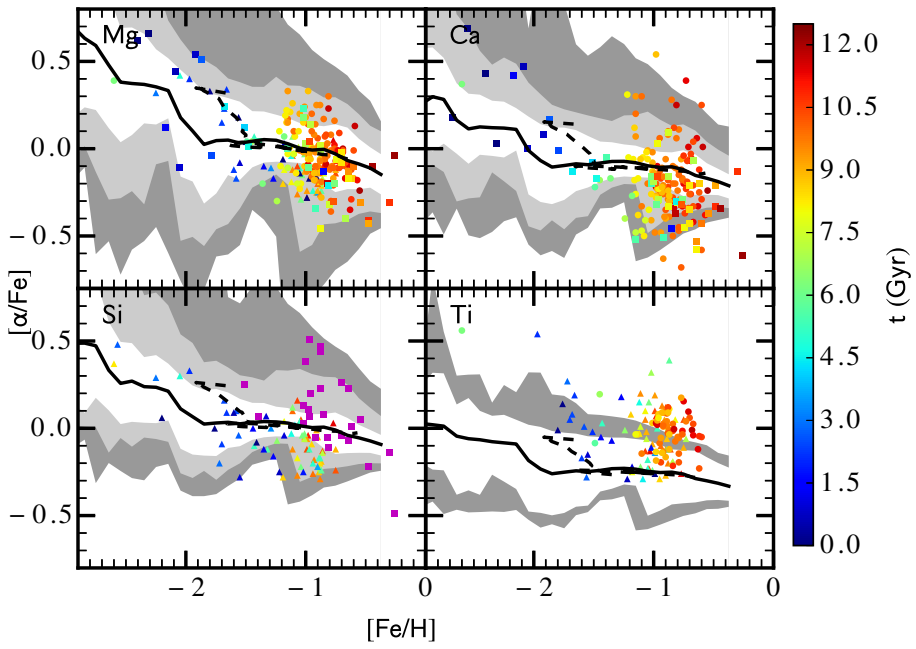


Figure 7.3: Comparisons of $[\alpha/Fe]$ vs. $[Fe/H]$ between observations and the standard case of our model. Data from different groups are shown as different symbols: [9] (circle), [46] (thin diamond), [47] (square), and [48] (up triangle). Colors represent the age information of stars. the space of center white, light grey and dark grey denotes $1\sigma$, $2\sigma$ and $3\sigma$ confidence region respectively from simulation results. $\langle[\alpha/Fe]\rangle_{fe}$ vs. $\langle[Fe/H]\rangle_{fe}$, $\langle[\alpha/Fe]\rangle_t$ vs. $\langle[Fe/H]\rangle_t$ is shown as solid and dashed line, respectively. (see text for definitions)

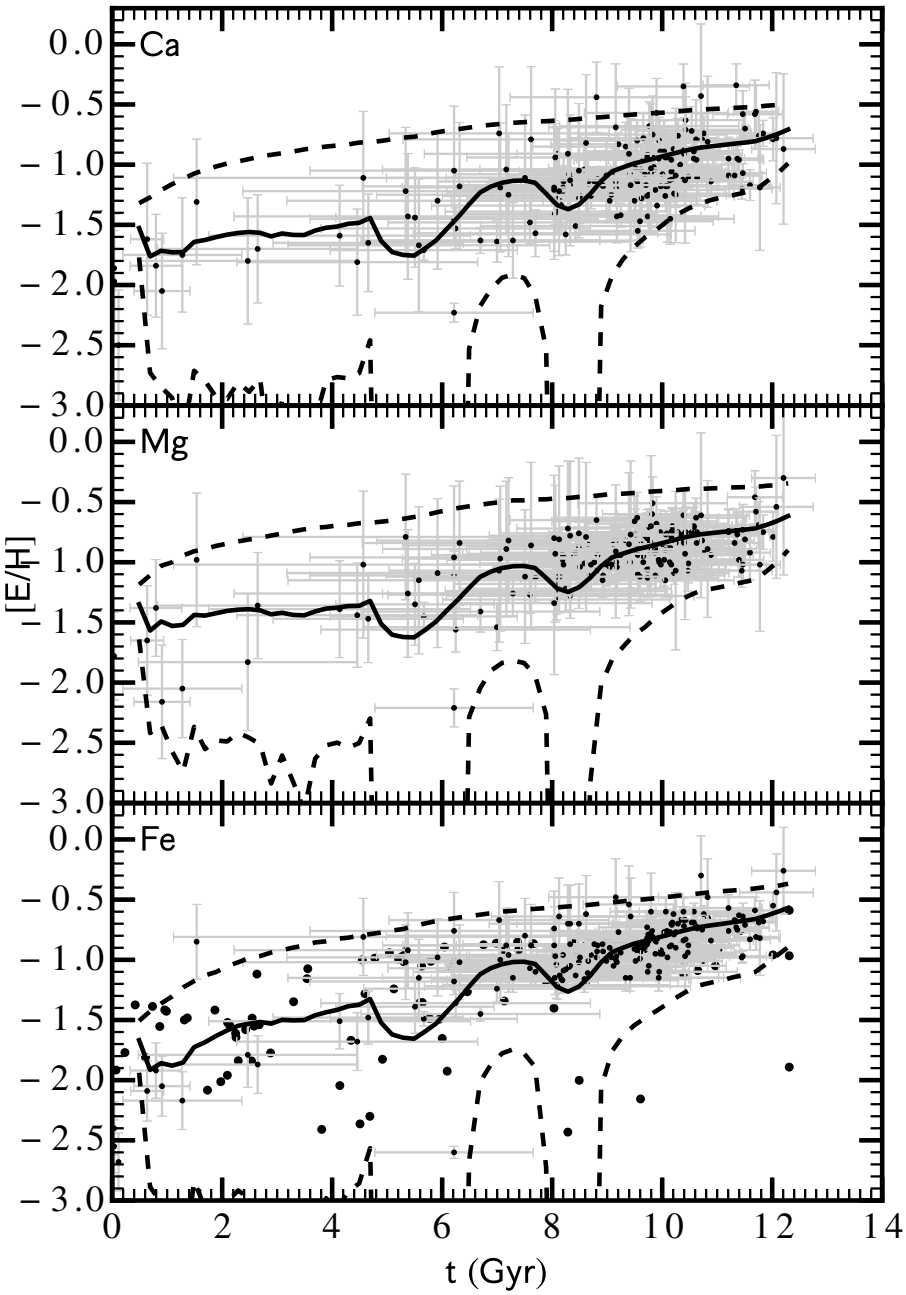


Figure 7.4: The time evolution of Mg, Ca and Fe for the entire history. The black solid line denotes $\langle [E/H] \rangle$ as a function of time from the standard case of our model. And the dashed lines represent 95% confidence level limit.

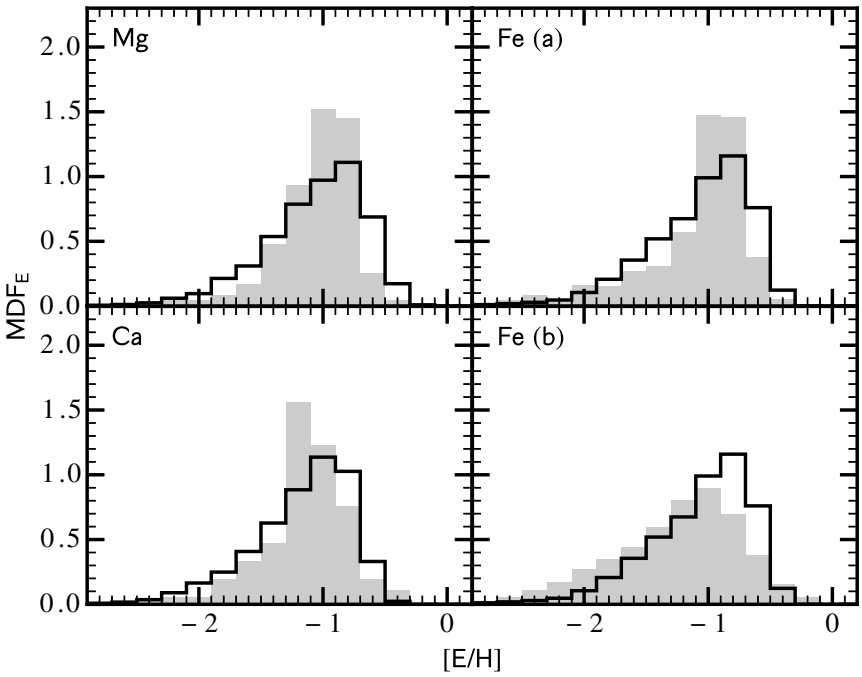


Figure 7.5: left: $MDF_{mg}$ and $MDF_{ca}$ from HR and MR spectroscopy [46], [9], [47] is shown as grey histogram. Note that all the Kirby's data presented in this paper is re-selected by de Boer. right: $MDF_{fe}$ from (a) HR and MR spectroscopy [46], [9], [47] [48] and (b) Ca II triplet line measurement [9] are shown as grey histogram. The solid histogram represents the results from the standard case of our model.

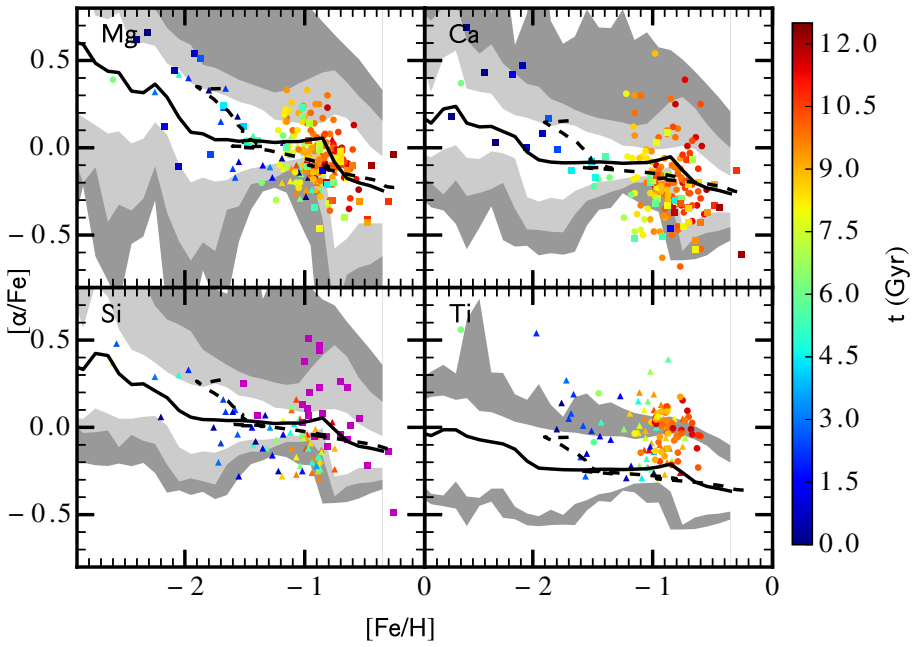


Figure 7.6: The same notation as Fig. 7.3. The simulation results show the case without metal loss enhancement.

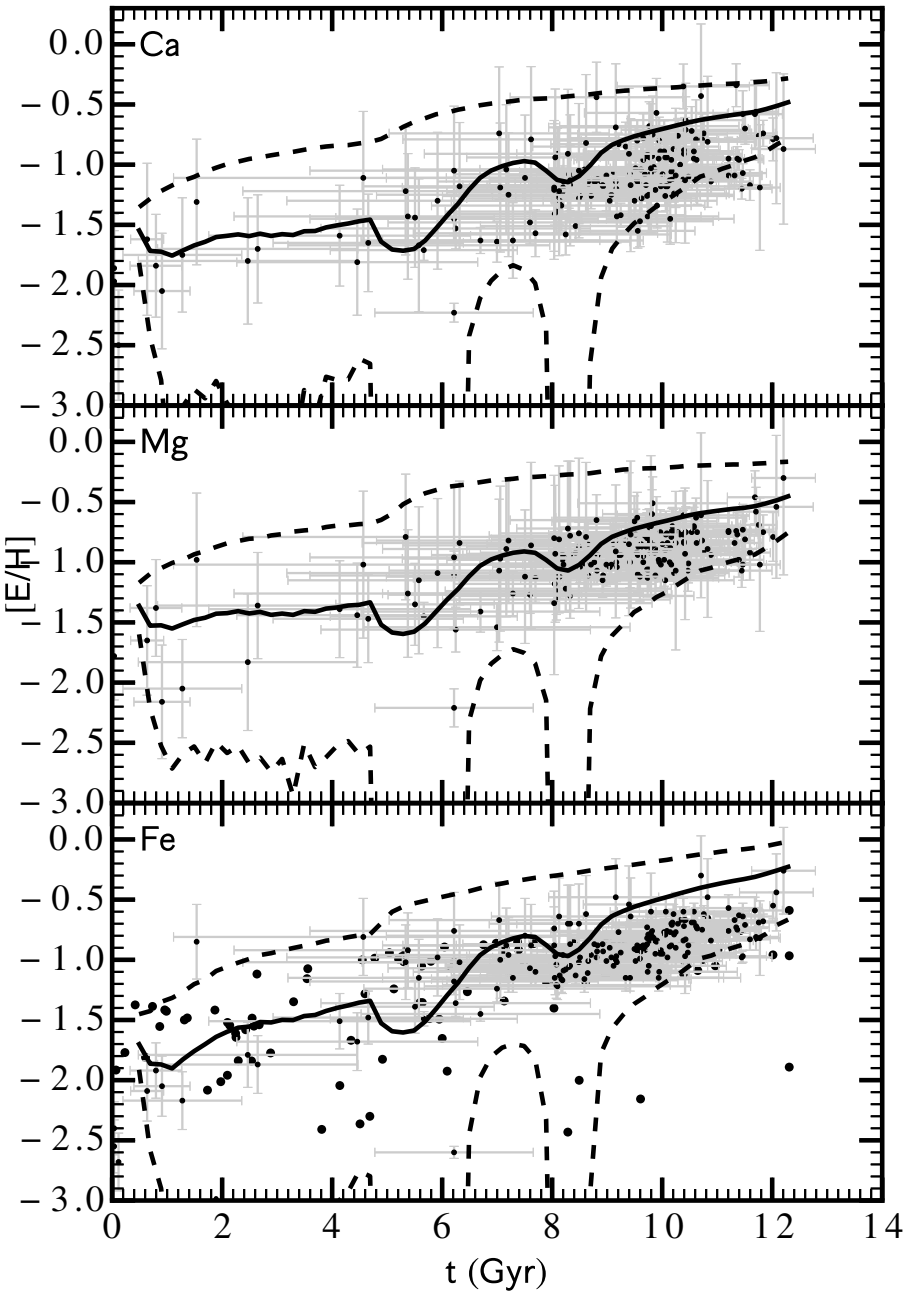


Figure 7.7: the same notation as Fig. 7.4. The simulation results show the case without metal loss enhancement.

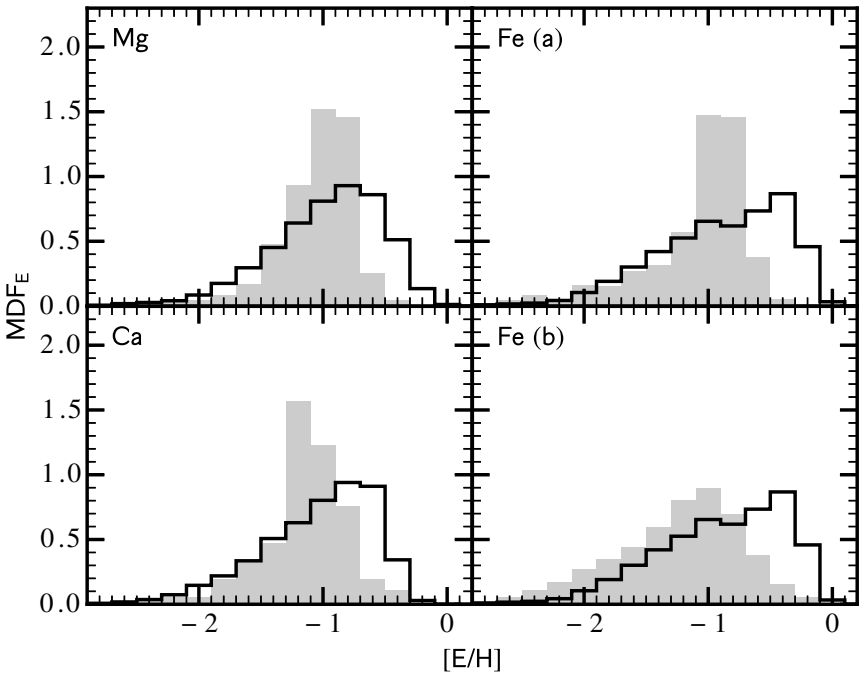


Figure 7.8: the same notation as Fig. 7.5. The simulation results show the case without metal loss enhancement.

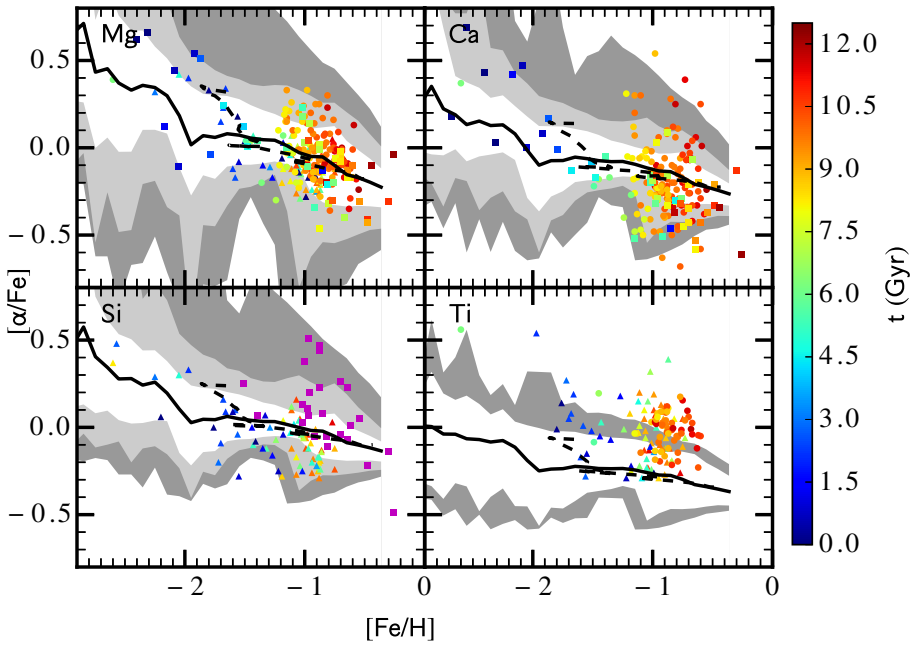


Figure 7.9: The same notation as Fig. 7.3. The simulation results show the case without SN Ia rate reduction.

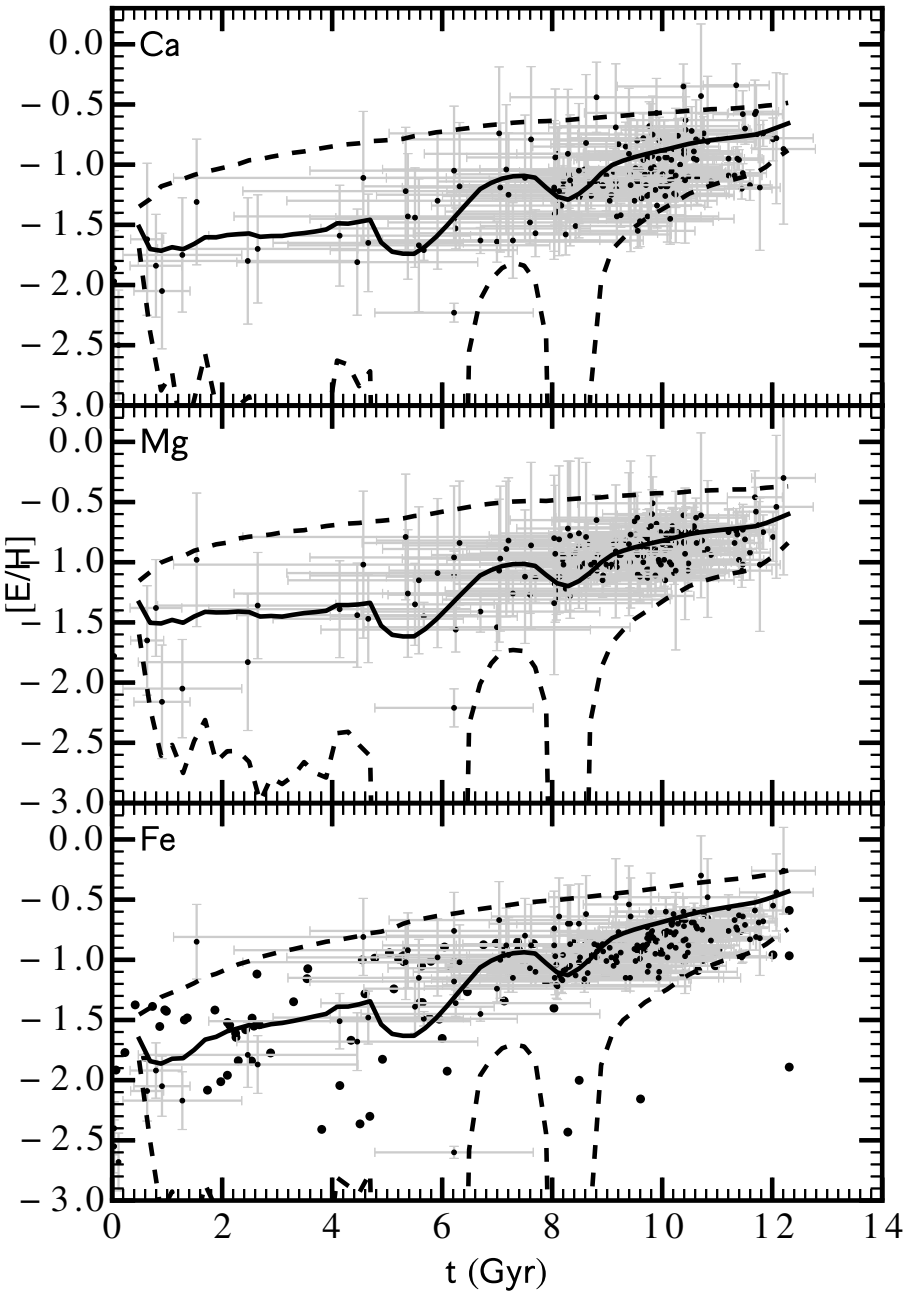


Figure 7.10: The same notation as Fig. 7.4. The simulation results show the case without SN Ia rate reduction.

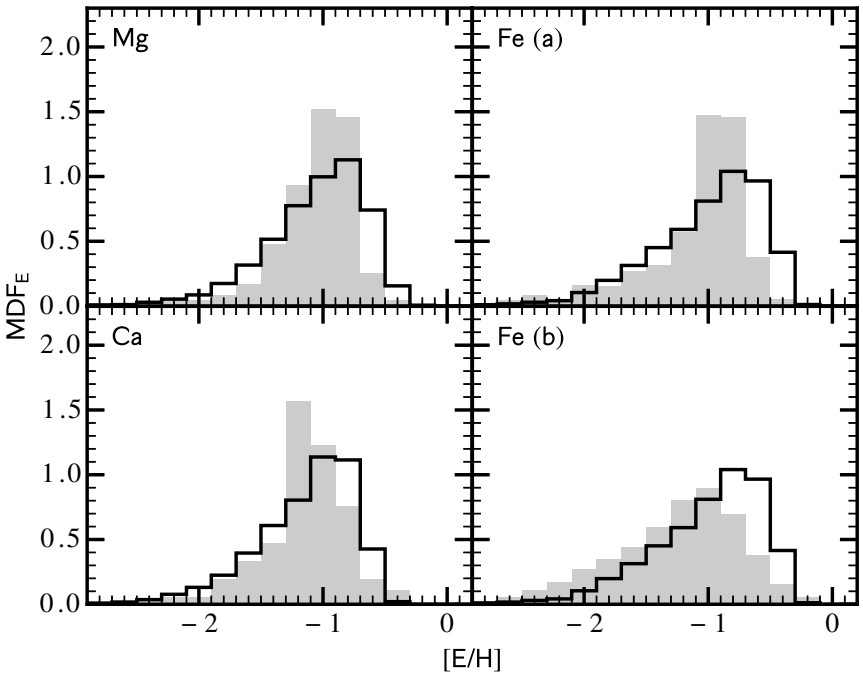


Figure 7.11: The same notation as Fig. 7.5. The simulation results show the case without SN Ia rate reduction.

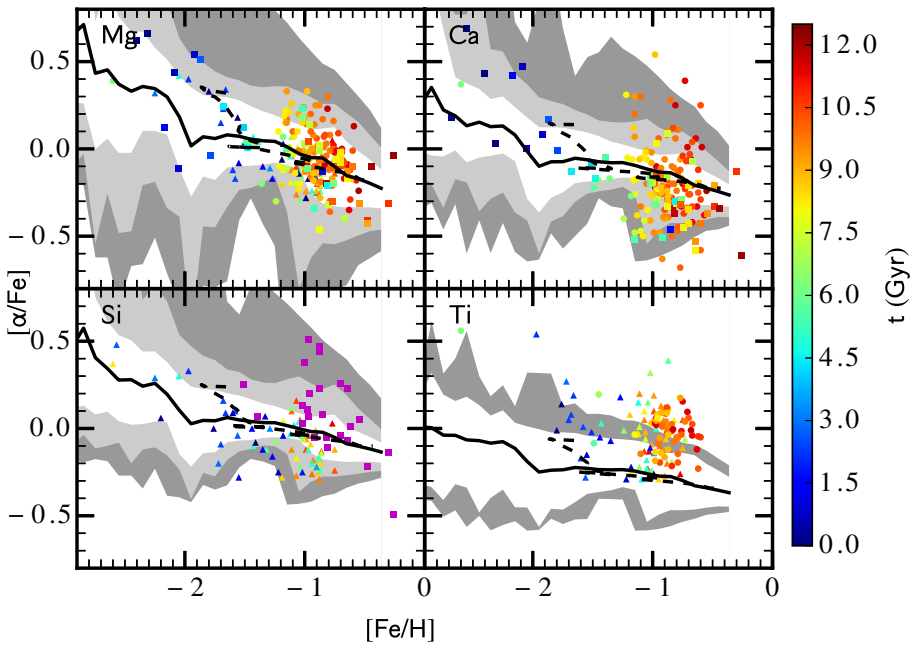


Figure 7.12: The same notation as Fig. 7.3. The simulation results show the case without high mass CCSNe.

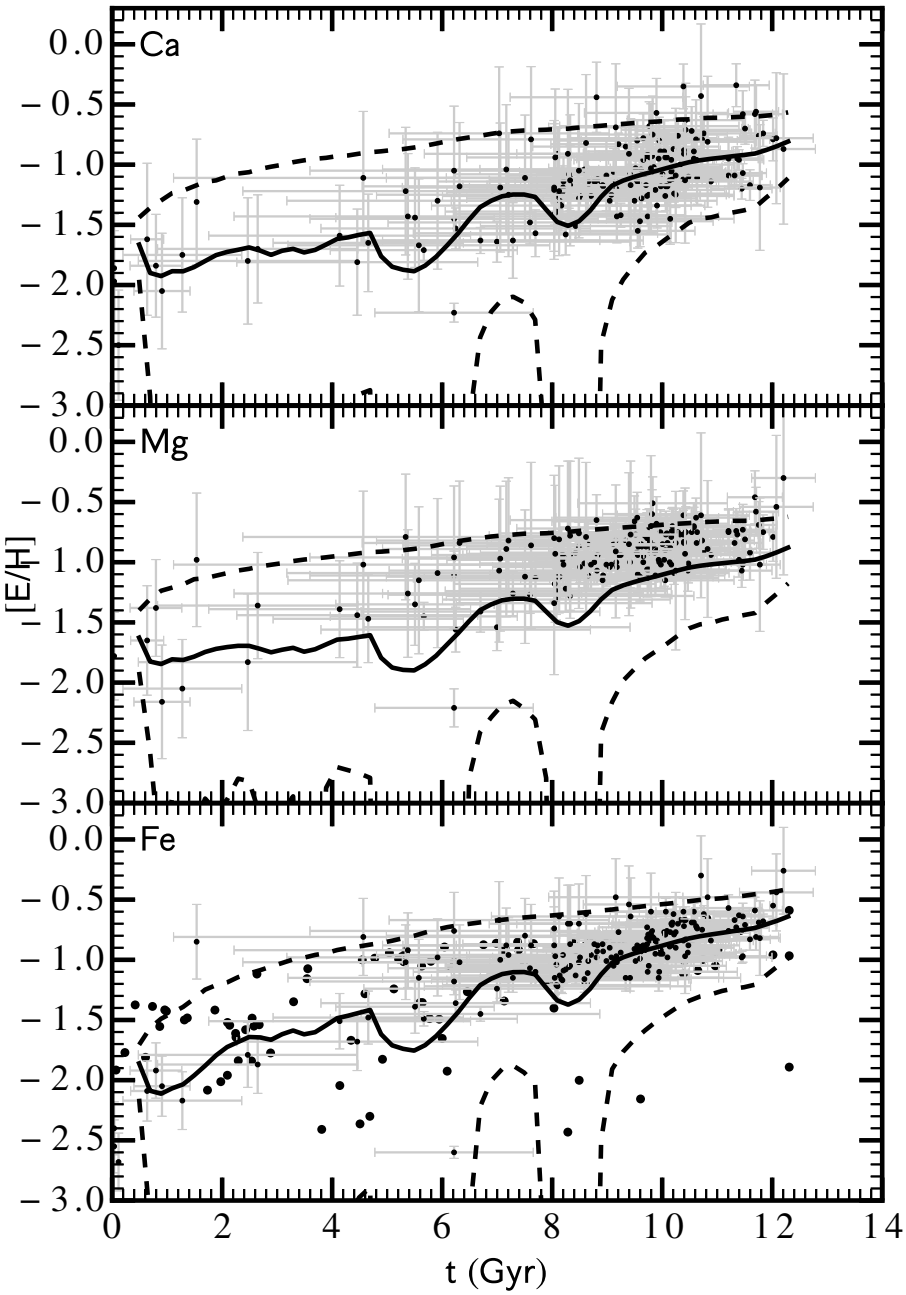


Figure 7.13: The same notation as Fig. 7.4. The simulation results show the case without high mass CCSNe.

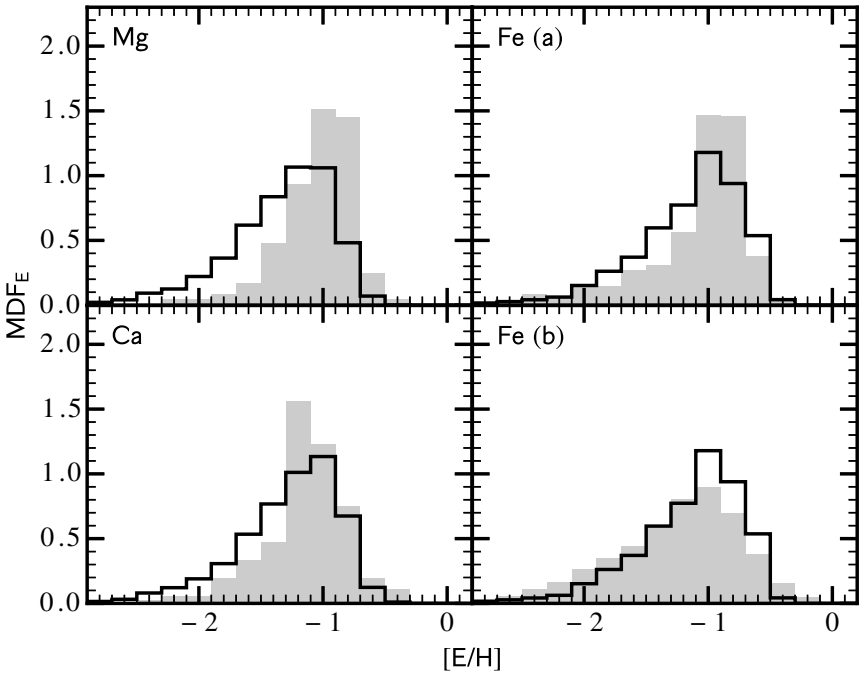


Figure 7.14: The same notation as Fig. 7.5. The simulation results show the case without high mass CCSNe.

# Chapter 8

# Conclusions

Galaxy formation and evolution is entangled with variety of physics processes in vastly different scales, which makes it one of the most challenging problems in astrophysics. Our approach to attack the problem is to estimate the gas dynamics of the simplest system based on the recent observed SFH, from an phenomenological point of view. The age and elemental abundances pattern from stellar spectroscopy opens another door for us to look into the snapshots of these small systems throughout the history. These data can be understood by the chemical evolution model based on its gas dynamics. On the other hand, the model gives us some insights into the understandings of the galaxy formation history.

Guided by data on star formation, especially those reported by [8] for nearby galaxies, we have assumed a global SFR $\psi(t) = \lambda_*[M_g(t)/M_\odot]^\alpha$ that is dependent on the total mass $M_g(t)$ for cold gas in the star-forming disk. We have examined three different cases of $\alpha = 1$, 1.5, and 2, and chosen the corresponding $\lambda_*$ in agreement with the empirical SFLs. For each case, we have used the data on Fornax's $\psi(t)$ provided by [9] to derive $M_g(t)$ and estimate the rate of net gas flow $\Delta F(t)$ to or from Fornax's star-forming disk. We have identified the onset of the transition in $\Delta F(t)$ from a net inflow to a net outflow as the time $t_{\rm sat}$ at which Fornax ceased evolving independently

and became an MW satellite. We have determined the mass $M_h(t_{\rm sat})$ of the Fornax halo at this time by using the median halo growth history in the model of [19] and requiring that the corresponding density profile give the mass enclosed within the half-light radius as derived from observations. We have further justified our chosen $\lambda_*$ by comparing the gas mass fraction $f_g(t) = M_g(t)/M_h(t)$ at $t < t_{\rm sat}$ with the results from cosmological simulations of [20] on gas accretion by halos in a reionized universe. Finally, based on all the above justification, we take account in the growth of star forming disk, and set $\lambda_*$ as a time variable, which depends on the disk size. In this more realistic picture, the gas mass at pre-satellite phase is reduced, which makes the baryonic to dark matter ratio closer to the simulation results.

Using the results for growing disk case and the present orbital parameters of Fornax, we have related $\Delta F(t)$ at $t > t_{\rm sat}$ to its orbital motion as an MW satellite and estimated the effects of ram pressure and tidal interaction with the MW. The Fornax halo lost $\sim 1/3$ of its CDM through tidal interaction but reaccreted some of the lost CDM near the end of its first orbital period. This reaccretion was responsible for the last episode of significant net gas inflow. Otherwise, gas was removed from the star-forming disk as hot gas created by SN heating escaped and was then lost from Fornax through ram-pressure stripping and tidal interaction. This lasted a few orbital periods and eventually terminated star formation in Fornax.

After we obtained a reasonable picture for the halo evolution and global gas dynamics of Fornax, we constructed the chemical evolution model on a 2D mass grid. We change the number of gas boxes according to the change of gas amount as a function time. And SN enrichment is implemented empirically with the key parameter as the mixing mass $M_x$. First of all, we distinguish two types of SN due to their distinct explosion environment and set $M_x$ differently. Then, considering the change of the gaseous system in the two epochs before and after $t_{\rm sat}$, we choose two sets of SN mixing mass, respectively. In the inflow dominated pre-satellite phase, SN mixing is enhanced by the gas turbulence in the system. Whereas in the satellite phase, the mixing mass is set as

the normal hot bubble mass, estimated by [39]. The motivation behind the choices is to match the scatter pattern in all [$\alpha$/Fe] vs. [Fe/H] plots, as well as the metallicity evolution history of [E/H] vs. t and the metallicity distribution $\mathrm{MDF}_E$ for Ca, Mg and Fe. We assess the basic model with different parameter settings, and demonstrated that the standard case generates the closest data sample to the observations.

# References


[1] R. C. Kennicutt and N. J. Evans. Star Formation in the Milky Way and Nearby Galaxies. *ARA&A*, 50:531–608, September 2012.

[2] M. R. Krumholz. The Big Problems in Star Formation: the Star Formation Rate, Stellar Clustering, and the Initial Mass Function. *ArXiv e-prints*, February 2014.

[3] Y. Gao and P. M. Solomon. The Star Formation Rate and Dense Molecular Gas in Galaxies. *APJ*, 606:271–290, May 2004.

[4] M. R. Krumholz and T. A. Thompson. The Relationship between Molecular Gas Tracers and Kennicutt-Schmidt Laws. *APJ*, 669:289–298, November 2007.

[5] R. C. Kennicutt, Jr. The Global Schmidt Law in Star-forming Galaxies. *APJ*, 498:541–552, May 1998.

[6] M. R. Krumholz and J. C. Tan. Slow Star Formation in Dense Gas: Evidence and Implications. *APJ*, 654:304–315, January 2007.

[7] M. R. Krumholz and C. F. McKee. A General Theory of Turbulence-regulated Star Formation, from Spirals to Ultraluminous Infrared Galaxies. *APJ*, 630:250–268, September 2005.

[8] F. Bigiel, A. Leroy, F. Walter, E. Brinks, W. J. G. de Blok, B. Madore, and M. D. Thornley. The Star Formation Law in Nearby Galaxies on Sub-Kpc Scales. *AJ*, 136:2846–2871, December 2008.

[9] T. J. L. de Boer, E. Tolstoy, V. Hill, A. Saha, E. W. Olszewski, M. Mateo, E. Starkenburg, G. Battaglia, and M. G. Walker. The star formation and chemical evolution history of the Fornax dwarf spheroidal galaxy. *A&A*, 544:A73, August 2012.

[10] M. R. Krumholz, C. F. McKee, and J. Tumlinson. The Star Formation Law in Atomic and Molecular Gas. *APJ*, 699:850–856, July 2009.

[11] M. R. Krumholz. The star formation law in molecule-poor galaxies. *MNRAS*, 436:2747–2762, December 2013.

[12] R. S. Somerville and R. Davé. Physical Models of Galaxy Formation in a Cosmological Framework. *ArXiv e-prints*, December 2014.

[13] G. S. Stinson, J. J. Dalcanton, T. Quinn, T. Kaufmann, and J. Wadsley. Breathing in Low-Mass Galaxies: A Study of Episodic Star Formation. *APJ*, 667:170–175, September 2007.

[14] S. Shen, P. Madau, C. Conroy, F. Governato, and L. Mayer. The Baryon Cycle of Dwarf Galaxies: Dark, Bursty, Gas-rich Polluters. *APJ*, 792:99, September 2014.

[15] P. F. Hopkins, E. Quataert, and N. Murray. Self-regulated star formation in galaxies via momentum input from massive stars. *MNRAS*, 417:950–973, October 2011.

[16] P. F. Hopkins, E. Quataert, and N. Murray. The structure of the interstellar medium of star-forming galaxies. *MNRAS*, 421:3488–3521, April 2012.

[17] P. F. Hopkins, E. Quataert, and N. Murray. Stellar feedback in galaxies and the origin of galaxy-scale winds. *MNRAS*, 421:3522–3537, April 2012.

[18] L. Mayer, C. Mastropietro, J. Wadsley, J. Stadel, and B. Moore. Simultaneous ram pressure and tidal stripping; how dwarf spheroidals lost their gas. *MNRAS*, 369:1021–1038, July 2006.

[19] D. H. Zhao, Y. P. Jing, H. J. Mo, and G. Börner. Accurate Universal Models for the Mass Accretion Histories and Concentrations of Dark Matter Halos. *APJ*, 707:354–369, December 2009.

[20] T. Okamoto, L. Gao, and T. Theuns. Mass loss of galaxies due to an ultraviolet background. *MNRAS*, 390:920–928, November 2008.

[21] J. Wolf, G. D. Martinez, J. S. Bullock, M. Kaplinghat, M. Geha, R. R. Muñoz, J. D. Simon, and F. F. Avedo. Accurate masses for dispersion-supported galaxies. *MNRAS*, 406:1220–1237, August 2010.

[22] D. J. Eisenstein and W. Hu. Baryonic Features in the Matter Transfer Function. *APJ*, 496:605–614, March 1998.

[23] G. Hinshaw, D. Larson, E. Komatsu, D. N. Spergel, C. L. Bennett, J. Dunkley, M. R. Nolta, M. Halpern, R. S. Hill, N. Odegard, L. Page, K. M. Smith, J. L. Weiland, B. Gold, N. Jarosik, A. Kogut, M. Limon, S. S. Meyer, G. S. Tucker, E. Wollack, and E. L. Wright. Nine-year Wilkinson Microwave Anisotropy Probe (WMAP) Observations: Cosmological Parameter Results. *ApJS*, 208:19, October 2013.

[24] M. T. Busha, M. A. Alvarez, R. H. Wechsler, T. Abel, and L. E. Strigari. The Impact of Inhomogeneous Reionization on the Satellite Galaxy Population of the Milky Way. *APJ*, 710:408–420, February 2010.

[25] S. Mao, H. J. Mo, and S. D. M. White. The evolution of galactic discs. *MNRAS*, 297:L71–L75, July 1998.

[26] S. Piatek, C. Pryor, P. Bristow, E. W. Olszewski, H. C. Harris, M. Mateo, D. Minniti, and C. G. Tinney. Proper Motions of Dwarf Spheroidal Galaxies from Hubble Space Telescope Imaging. V. Final Measurement for Fornax. *AJ*, 133:818–844, March 2007, astro-ph/0612705.

[27] I. King. The structure of star clusters. I. an empirical density law. *AJ*, 67:471, October 1962.

[28] J. Han, Y. P. Jing, H. Wang, and W. Wang. Resolving subhaloes' lives with the Hierarchical Bound-Tracing algorithm. *MNRAS*, 427:2437–2449, December 2012.

[29] M. Nichols, D. Lin, and J. Bland-Hawthorn. Episodic Starbursts in Dwarf Spheroidal Galaxies: A Simple Model. *APJ*, 748:149, April 2012.

[30] C. F. McKee and J. P. Ostriker. A theory of the interstellar medium - Three components regulated by supernova explosions in an inhomogeneous substrate. *APJ*, 218:148–169, November 1977.

[31] T. Kaufmann, J. S. Bullock, A. H. Maller, T. Fang, and J. Wadsley. Redistributing hot gas around galaxies: do cool clouds signal a solution to the overcooling problem? *MNRAS*, 396:191–202, June 2009.

[32] W.-H. Hsu, M. E. Putman, F. Heitsch, S. Stanimirović, J. E. G. Peek, and S. E. Clark. Physical Properties of Complex C Halo Clouds. *AJ*, 141:57, February 2011.

[33] C. Murali. The Magellanic Stream and the Density of Coronal Gas in the Galactic Halo. *APJL*, 529:L81–L84, February 2000.

[34] M. Nichols and J. Bland-Hawthorn. Gas Depletion in Local Group Dwarfs on ˜250 kpc Scales: Ram Pressure Stripping Assisted by Internal Heating at Early Times. *APJ*, 732:17, May 2011.

[35] B. D. Oppenheimer and R. Davé. Cosmological simulations of intergalactic medium enrichment from galactic outflows. *MNRAS*, 373:1265–1292, December 2006.

[36] T. Okamoto, C. S. Frenk, A. Jenkins, and T. Theuns. The properties of satellite galaxies in simulations of galaxy formation. *MNRAS*, 406:208–222, July 2010.

[37] A. Heger and S. E. Woosley. Nucleosynthesis and Evolution of Massive Metal-free Stars. *APJ*, 724:341–373, November 2010.

[38] K. Maeda, F. K. Röpke, M. Fink, W. Hillebrandt, C. Travaglio, and F.-K. Thielemann. Nucleosynthesis in Two-Dimensional Delayed Detonation Models of Type Ia Supernova Explosions. *APJ*, 712:624–638, March 2010.

[39] K. Thornton, M. Gaudlitz, H.-T. Janka, and M. Steinmetz. Energy Input and Mass Redistribution by Supernovae in the Interstellar Medium. *APJ*, 500:95–119, June 1998.

[40] A. C. Petit, M. R. Krumholz, N. J. Goldbaum, and J. C. Forbes. Mixing and transport of metals by gravitational instability-driven turbulence in galactic discs. *MNRAS*, 449:2588–2597, May 2015.

[41] S. Shen, R. J. Cooke, E. Ramirez-Ruiz, P. Madau, L. Mayer, and J. Guedes. The History of R-Process Enrichment in the Milky Way. *APJ*, 807:115, July 2015.

[42] E. Tolstoy, V. Hill, and M. Tosi. Star-Formation Histories, Abundances, and Kinematics of Dwarf Galaxies in the Local Group. *ARA&A*, 47:371–425, September 2009.

[43] P. Kroupa. On the variation of the initial mass function. *MNRAS*, 322:231–246, April 2001.

[44] D. Maoz, F. Mannucci, and T. D. Brandt. The delay-time distribution of Type Ia supernovae from Sloan II. *MNRAS*, 426:3282–3294, November 2012.

[45] D. Romano, C. Chiappini, F. Matteucci, and M. Tosi. Quantifying the uncertainties of chemical evolution studies. I. Stellar lifetimes and initial mass function. *A&A*, 430:491–505, February 2005.

[46] E. N. Kirby, G. A. Lanfranchi, J. D. Simon, J. G. Cohen, and P. Guhathakurta. Multi-element Abundance Measurements from Medium-resolution Spectra. III.

Metallicity Distributions of Milky Way Dwarf Satellite Galaxies. *APJ*, 727:78, February 2011.

[47] B. Lemasle, T. J. L. de Boer, V. Hill, E. Tolstoy, M. J. Irwin, P. Jablonka, K. Venn, G. Battaglia, E. Starkenburg, M. Shetrone, B. Letarte, P. François, A. Helmi, F. Primas, A. Kaufer, and T. Szeifert. VLT/FLAMES spectroscopy of red giant branch stars in the Fornax dwarf spheroidal galaxy. *A&A*, 572:A88, December 2014.

[48] B. Hendricks, A. Koch, M. Walker, C. I. Johnson, J. Peñarrubia, and G. Gilmore. Insights from the outskirts: Chemical and dynamical properties in the outer parts of the Fornax dwarf spheroidal galaxy. *A&A*, 572:A82, December 2014.

[49] T. J. L. de Boer, E. Tolstoy, V. Hill, A. Saha, K. Olsen, E. Starkenburg, B. Lemasle, M. J. Irwin, and G. Battaglia. The star formation and chemical evolution history of the sculptor dwarf spheroidal galaxyâ. *A&A*, 539:A103, March 2012.

# Appendix A

# CMD Fitting Method

The underlying principle of CMD fitting method is that SFH is derived by linear combination of several simple populations, which allows a SFH derivation free from initial assumptions. We gives a short summary on how to carry out this method (see detail review in [49]).

## A.1 Methodology

First of all, let us summarize the general routine of CMD fittings in three steps.

(i) Generating of sCMD (synthetic CMD) from a simple star formation rate $\Psi(t, Z)$ with time and metallicity dependence. (The simplest case is a constant distribution). These synthetic stars are projected on age and metallicity space, constituting the vector-basis of any arbitrary stellar populations as $N_i$.

(ii) A set of boxes is defined in observed CMD through Hess diagrams. stars in box $j$ can be written as the linear combination of $N_i^j$.

$$N^j = \Sigma_i \alpha_i N_i^j \tag{A.1}$$

(iii) The technique used to determine the best SFH is to minimize the difference between observed and synthetic CMDs. Specifically, the best solution as a set of $\alpha_i$ is

obtained by minimizing $\chi^2$.

$$\chi^2 = 2\Sigma_j N_j - M_j + M_j \ln \frac{M_j}{N_j}, \tag{A.2}$$

where $M_j$ and $N_j$ is the total number of stars in a observed and synthetic Hess bin, respectively ($N_j = \Sigma SFR_i \times CMD_{j,i}$ in the photometric part, and $N_j = \Sigma SFR_i \times MDF_{j,i}$ in the spectroscopic part). The solution SFH can be written as

$$\Psi(t, Z) = \Sigma_i \alpha_i \psi_i \tag{A.3}$$

where $\psi_i$ refers to model $i$, which takes from 1 to $n \times m$.

## A.2 SFH Uncertainties

### A.2.1 Internal Errors

The internal errors of CMD fittings have two sources. The first one is data sampling, which can be calculated assuming that the number of stars in each CMD box behaves according to Poison statistics. Once the best solution has been found, noted as $\alpha_i$, the number of stars in each grid box from observational input, are randomly modified according to Poisson statistics. The procedure is repeated for $n_r$ times. The solution of each time is represented as $\alpha_{r,i}$. Then

$$\sigma_{\alpha_i} = \left( \frac{\Sigma_r (\alpha_{r,i} - \alpha_i)^2}{n_r - 1} \right)^{1/2} \tag{A.4}$$

can be used as an estimate of the errors from data sampling.

The other major source of error is parameter sampling. It comes from the fact that the choice of CMD griddings, age bins and metallicity bins will affect the final SFH. Thus one can evaluate this kind of uncertainties by using different bin sizes and distributions. Specifically, one apply three different shifts in the parameter space of age and metallicity: a shift of half a bin size in age and in metallicity and also a shift in both age and metallicity simultaneously. For the photometric binning two different bin

sizes are used, with the different shifts applied to each. The SFH is determined for all these different griddings, after which the results are returned to a common grid.

### A.2.2 Observational Effects

Besides of the internal errors, another crucial aspect is the observational biases. We want to obtain a look-up table, which can be used to accurately model the effects of observational conditions. It is done by carrying out a large number of simulations, in which a number of artificial stars with known brightness are placed on the observed images. These images are then re-reduced in exactly the same way as the original images, after which the artificial stars are recovered from the photometry. Then the lookup-table can be generated and it can be used to assign an individual artificial star with similar colors and magnitudes to each star in an ideal synthetic CMD.

## A.3 Spectroscopic Data

The determination of SFH includes the spectroscopic data, which contributes less to the overall goodness of fit than the photometry, but significantly restricts the possible solutions. Thus the spectroscopic MDF serves as an extra constrain. And the photometric and spectroscopic components weight differently, with the enhancement of the latter one.

In order to include the spectroscopic MDF at the same time as the photometry, an equivalent of a Hess diagram for [Fe/H] is used. Basically, synthetic CMDs of different stellar populations is generated and stars are binned in metallicity. The spectroscopic observations only come from a fraction of the RGB, which constitutes a small fraction of stars present in the CMD. To make sure that the synthetic CMDs fully sample the RGB, synthetic MDF populations are generated with an artificially increased initial SFR, which is later corrected in the MDF models. The observed spectroscopic uncertainties on the metallicities are simulated by considering each individual synthetic star to have

a Gaussian profile with a width determined by the average observational uncertainty on $[Fe/H]$. The metallicities of these individual stars are then combined to form a synthetic MDF which takes into account observed uncertainties.

## A.4 Determining Ages of Individual Stars

The determination of ages of individual stars is done in this way. For each observed star with spectroscopic abundances we find all the stars in a synthetic CMD made with the SFH of that galaxy, with the same magnitude in all filters and metallicity within the observed uncertainties. The age of the observed star is set as the mean age of the matched sample. The advantage of using the SFH results to obtain ages for individual RGB stars is a more constrained AMR (age metallicity relation) because the age of a single observed star information is constrained from the entire CMD. Compared with the standard simple isochrone fitting technique, one uses a fine grid of [Fe/H], age and [$\alpha$/Fe] to obtain the age and uncertainty for an observed star. The AMR determined using isochrone fitting has bigger age uncertainties and allows younger ages for each star. This is because the age for simple isochrone fitting depends only on the color of the RGB and the measured [Fe/H], which allows a wide range in ages.

# Appendix B

# Area conserved Quadratic Fitting

We use a smooth SFR $\psi(t)$ from a quadratic-spline fit to the data that conserves the total number of stars formed in each SF bin from observations, and guarantees the continuity of $\psi(t)$ and $\psi'(t) \equiv \mathrm{d}\psi/\mathrm{d}t$. Specifically, the SFR in the $i$th timebin $[t_{i-1}, t_i]$ is given by

$$\psi(t) = \psi(t_{i-1}) + p_i(t - t_{i-1}) + q_i(t - t_{i-1})^2, \tag{B.1}$$

which automatically satisfies the first continuity condition. $p_i$ and $q_i$ are the coefficients defined in this timebin. After taking the derivative of the above eq at the boundaries, we obtain

$$\psi'(t_{i-1}) = p_i, \quad \psi'(t_i) = p_i + 2q_i\Delta_i, \quad \Delta_i = t_i - t_{i-1}. \tag{B.2}$$

Thus the coefficients can be represented as

$$p_i = \psi'(t_{i-1}), \quad q_i = \frac{\psi'(t_i) - \psi'(t_{i-1})}{2\Delta_i} \tag{B.3}$$

Following the same recipe, in the $i+1$ th timebin, we assume SFR is defined as $\phi(t)$, then

$$p_{i+1} = \phi'(t_i), \quad q_{i+1} = \frac{\phi'(t_{i+1}) - \phi'(t_i)}{2\Delta_{i+1}} \tag{B.4}$$

According to the second continuity condition, $\phi'(t_i) = \psi'(t_i)$. And we use the smooth $\psi(t)$ for the entire history, thus $\phi'(t_{i+1}) = \psi'(t_{i+1})$. The coefficients can be written as

$$p_{i+1} = \psi'(t_i), \quad q_{i+1} = \frac{\psi'(t_{i+1}) - \psi'(t_i)}{2\Delta_{i+1}} \tag{B.5}$$

Similarly, the coefficients in each timebin can be described with the first derivatives of SFR in that bin. Now, we convert the problem to solving the equations of $\psi'(t_i)$, which have $n+1$ unknowns. The conservation of area in this timebin requires

$$\begin{aligned} \bar{\psi_i}\Delta_i &= \int_{t_{i-1}}^{t_i} \psi(t)\mathrm{d}t \\ &= \psi(t_{i-1})\Delta_i + \frac{1}{2}p_i\Delta_i^2 + \frac{1}{3}q_i\Delta_i^3, \end{aligned} \tag{B.6}$$

where $\bar{\psi_i}$ and $\Delta_i$ come from the data. Simplify the above equation gives

$$\bar{\psi_i} = \psi(t_{i-1}) + \frac{1}{2}p_i\Delta_i + \frac{1}{3}q_i\Delta_i^2, \tag{B.7}$$

where

$$\psi(t_{i-1}) = \psi(t_i) - p_i\Delta_i - q_i\Delta_i^2 \tag{B.8}$$

from Eq. (A1), thus Eq. (A5) can be rewritten as

$$\bar{\psi_i} = \psi(t_i) - \frac{1}{2}p_i\Delta_i - \frac{2}{3}q_i\Delta_i^2, \tag{B.9}$$

We can also write the similar equation for the $i+1$ th bin

$$\bar{\psi_{i+1}} = \psi(t_i) + \frac{1}{2}p_{i+1}\Delta_{i+1} + \frac{1}{3}q_{i+1}\Delta_{i+1}^2. \tag{B.10}$$

Subtracting Eq. (A8) from Eq. (A9) gives

$$\bar{\psi}_{i+1} - \bar{\psi}_i = \frac{1}{2}(p_{i+1}\Delta_{i+1} + p_i\Delta_i) + \frac{1}{3}(q_{i+1}\Delta_{i+1}^2 + 2q_i\Delta_i^2) \tag{B.11}$$

Substitute $p_i, q_i$ in the above equation,

$$\begin{aligned} \bar{\psi}_{i+1} - \bar{\psi}_i &= \frac{1}{2}(\psi'(t_i)\Delta_{i+1} + \psi'(t_{i-1})\Delta_i) + \frac{1}{3}\left(\frac{\psi'(t_{i+1}) - \psi'(t_i)}{2\Delta_{i+1}}\Delta_{i+1}^2 + \frac{\psi'(t_i) - \psi'(t_{i-1})}{\Delta_i}\Delta_i^2\right) \\ &= \frac{\Delta_i}{6}\psi'(t_{i-1}) + \frac{\Delta_i + \Delta_{i+1}}{3}\psi'(t_i) + \frac{\Delta_{i+1}}{6}\psi'(t_{i+1}) \end{aligned} \tag{B.12}$$

There are $n-1$ equations as Eq. (A11) And we set $\psi'(t_0) = \psi'(t_n) = 0$, which give us $n+1$ equations in total.

# Appendix C

# Cosmology

## C.1 Friedmann Equation

According to Friedmann equation, the scale factor $a$ is determined by

$$\frac{1}{a}\frac{\mathrm{d}a}{\mathrm{d}t} = H = \sqrt{\frac{8\pi G\rho_{cr}(z)}{3}}, \quad \rho_{cr}(z) = \rho_{cr}(0)\left[\frac{\Omega_m}{a^3} + \Omega_\Lambda\right] \tag{C.1}$$

is the critical density at redshift $z$, $\rho_{cr}(0) = 3H_0^2/8\pi G$ is the critical density at present. $H_0 = 100hkms^{-1}Mpc^{-1}$ is the Hubble constant. In this paper, we adopt $h = 0.69$, $\Omega_m = 0.29$ ($\Omega_{CDM} = 0.243$, $\Omega_b = 0.047$), and $\Omega_\Lambda = 0.71$. In calculating the halo growth history, we use a primodial power spectrum with a spectral index $n_s = 0.96$ and the transfer function with a present temperature of $2.726K$ for the cosmic microwave background to obtain the linear power spectrum, the amplitude of which is fixed by $\sigma_8 = 0.82$. And redshift $z$ is defined as

$$1 + z = \frac{1}{a}, \tag{C.2}$$

The conversion between $z$ and $t$ is done in the following way,

$$\frac{\mathrm{d}a}{\mathrm{d}t} = aH$$

$$t = \int_0^t \mathrm{d}t = \int_{a(0)}^{a(t)} \frac{\mathrm{d}a}{aH} = \frac{1}{H_0}\int_{a(0)}^{a(t)} \frac{\mathrm{d}a}{\sqrt{\frac{\Omega_m}{a} + \Omega_\Lambda a^2}}$$

The integral is dimensionless, we need to convert the unit of $1/H_0$ into Gyr.

$$\frac{1}{\mathrm{km}\cdot\mathrm{s}^{-1}\mathrm{Mpc}^{-1}} = \frac{\mathrm{Mpc}}{\mathrm{km}}\mathrm{s} = \frac{3.085\times10^{19}}{3600\times24\times365}\mathrm{Gyr} = 978\mathrm{Gyr} \tag{C.3}$$

## C.2 Paramters of Dark Matter Halo

Define $r_{vir}$ as the radius of a spherical volume within which the mean density is $\Delta_c$ times the critical density at that redshift, thus

$$M_h = \frac{4\pi}{3} r_{vir}^3 \rho_{cr}(z)\Delta_c, \tag{C.4}$$

where $\Delta_c$ is taken from the solution to the collapse of a spherical top-hat perturbation through fitting method,

$$\Delta_c = 18\pi^2 + 82(\Omega_z - 1) - 39(\Omega_z - 1)^2, \quad \Omega_z \equiv \frac{\rho_m}{\rho_{cr}} = \frac{\Omega_m(1+z)^3}{\Omega_m(1+z)^3 + \Omega_\Lambda} \tag{C.5}$$

The mass distribution of a halo can be described approximately by the Navarro-Frenk-White (NFW) density profile

$$\rho(r) = \frac{\rho_0}{(r/r_s)[1+(r/r_s)]^2} \tag{C.6}$$

Thus the dark matter within radius $r$ can be calculated by

$$\begin{aligned} M(r) &= \int_0^r 4\pi r^2 \rho(r)\mathrm{d}r \\ &= 4\pi\rho_0 r_s^3 \int_0^x \frac{\mathrm{d}x}{x(1+x)^2}, \quad x = \frac{r}{r_s} \\ &= 4\pi\rho_0 r_s^3 f(x), \quad f(x) = \ln(1+x) + \frac{x}{1+x} \end{aligned} \tag{C.7}$$

Thus the total mass of a dark matter halo is

$$M_h = 4\pi\rho_0 r_s^3 f(c), \tag{C.8}$$

where $c \equiv r_{vir}/r_s$ is defined as the concentration parameter for that halo. The dark matter mass within half light radius $r_{1/2}$ is

$$\begin{aligned} M_{1/2} &= 4\pi\rho_0 r_s^3 f(r/r_s) \\ &= M_h \frac{f(cr_{1/2}/r_{vir})}{f(c)} \end{aligned} \tag{C.9}$$

From Eq. (B.4), $r_{vir}$ can be calculated as

$$r_{vir} = \left(\frac{3}{4\pi}\right)^{1/3} M_h^{1/3} \Delta_c^{-1/3} \rho_{cr}^{-1/3}(z), \tag{C.10}$$

where $\rho_{cr}(z)$ is obtained from Eq. (B5)

$$\rho_{cr}(z) = \frac{\rho_m(z)}{\Omega_z} = \frac{\rho_{cr,0}\Omega_m(1+z)^3}{\Omega_z}, \quad \rho_{cr,0} = \frac{3H_0^2}{8\pi G} = 128\mathrm{M}_\odot/\mathrm{kpc}^3. \tag{C.11}$$

Thus

$$r_{vir} = C \left(\frac{M}{10^8 h^{-1} M_\odot}\right)^{1/3} \left(\frac{\Omega_m}{\Omega_z}\frac{\Delta_c}{18\pi^2}\right)^{-1/3} \left(\frac{1+z}{10}\right)^{-1} h^{-1}\mathrm{kpc}, \tag{C.12}$$

where the coefficent $C$ is calculated as

$$C = \left(\frac{3}{4\pi}\right)^{1/3} (10^8 h^{-1})^{1/3} (18\pi^2)^{-1/3} \cdot 0.1 \cdot h \cdot \rho_{cr,0}^{-1/3} = 0.79 \tag{C.13}$$

Its circular velocity is

$$v_{circ} = \sqrt{\frac{GM_h}{r_{vir}}} = 23.7 \left(\frac{M_h}{10^8 h^{-1}}\right)^{1/3} \left(\frac{\Omega_m}{\Omega_z}\frac{\Delta_c}{18\pi^2}\right)^{1/6} \left(\frac{1+z}{10}\right)^{1/2} \mathrm{km/s}^{-1} \tag{C.14}$$

and its virial temperature is

$$T_{vir} = \frac{\mu m_p v_{circ}^2}{2k} = 3.35 \times 10^4 \mu \left(\frac{M_h}{10^8 h^{-1}}\right)^{2/3} \left(\frac{\Omega_m}{\Omega_z}\frac{\Delta_c}{18\pi^2}\right)^{1/3} \left(\frac{1+z}{10}\right) \mathrm{K} \tag{C.15}$$

where $\mu$ is the mean molecular weight of gas molecule, and $m_p$ is the proton mass. The value of $\mu$ depends on the ionization fraction of the gas; The primordial mass fractions of protons and $^4$He is 0.75 and 0.25, thus $\mu = 1/(0.75/m_p + 0.25/4m_p)/m_p = 1.23$ for neutral primordial gas, $\mu = 1/(2 \cdot 0.75/m_p + 3 \cdot 0.25/4m_p)/m_p = 0.59$ for a fully ionized primodial gas, and $\mu = 1/(2 \cdot 0.75/m_p + 2 \cdot 0.25/4m_p)/m_p = 0.62$ for a gas with ionized hydrogen but only singly-ionized helium. We take $\mu = 1.23$ for $T_{vir} < 1.5 \times 10^4$ K and $\mu = 0.59$ for $T_{vir} \leq 1.5 \times 10^4$ K.

## C.3 Formation of Galactic Discs

### C.3.1 Singular Isothermal Sphere

In singular isothermal sphere model, the system is in hydrostatic equilibrium with constant temperature, and the thermal pressure support balances gravitational potential.

$$\frac{\mathrm{d}p}{\mathrm{d}r} = -\rho\frac{\mathrm{d}\phi}{\mathrm{d}r}, \tag{C.16}$$

where $p = \rho\sigma^2$, and $\sigma^2 = kT/m$ is independent of radius. Integrating C.16 on both sides gives

$$\int \frac{\mathrm{d}\rho}{\rho} = -\int \frac{\mathrm{d}\phi}{\sigma^2}, \tag{C.17}$$

thus

$$\rho = \rho_c \exp\left(-\frac{\phi}{\sigma^2}\right), \qquad \phi = -\sigma^2 \ln\left(\frac{\rho}{\rho_c}\right) \tag{C.18}$$

Inserting C.18 in the Poisson's equation $\nabla^2\phi = 4\pi G\rho$, we get

$$\frac{1}{r^2}\frac{\mathrm{d}}{\mathrm{d}r}\left(r^2\frac{\mathrm{d}}{\mathrm{d}r}(\ln\rho)\right) = -\frac{4\pi G\rho}{\sigma^2} \tag{C.19}$$

Supposing $\rho(r) = \eta r^{-\alpha}$, we can solve the above differential equation as

$$\rho(r) = \frac{\sigma^2}{2\pi G r^2} \tag{C.20}$$

The limiting radius of a DMH is defined to the radius $r_{200}$ at which the mean mass density is $200\rho_{\mathrm{crit}}$. Thus

$$r_{200} = \frac{\sigma}{10H(z)}, \qquad M_h = \frac{\sigma^2 r_{200}}{G} = \frac{\sigma^3}{10GH(z)} \tag{C.21}$$

Mao et al [25] assume that the disc mass fraction is fixed as $m_d$, thus the disc mass is

$$M_d = \frac{m_d\sigma^3}{10GH(z)} \tag{C.22}$$

They also assume that the disc has exponential surface density profiles,

$$\Sigma(r) = \Sigma_0 \exp(-r/r_d) \tag{C.23}$$

And the disk radius and central surface density is defined as

$$M_d = 2\pi\Sigma_0 r_d^2 \tag{C.24}$$

They assume that the angular momentum of the disc is a fraction of $j_d$ of that of the halo

$$J_d = j_d J \tag{C.25}$$

where J is the total angular momentum and it can be characterized by the spin parameter $\lambda$ of a halo

$$\lambda = J|E|^{1/2}G^{-1}M^{-5/2} \tag{C.26}$$

$$J_d = 2\pi \int \sigma\Sigma(r) r^2 \mathrm{d}r = 4\pi\Sigma_0\sigma r_d^3 = 2M_d r_d \sigma \tag{C.27}$$

Thus the disc size can be interpreted as

$$r_d = \frac{\lambda G M^{3/2}}{2\sigma|E|^{1/2}} \left(\frac{j_d}{m_d}\right) \tag{C.28}$$

For a specific halo with fixed $\lambda$, $m_d$ and $j_d$, the disc size scales as the viral radius.

### C.3.2 NFW Profile

In the NFW profile, we follow the same approach to calculate the disc size.

$$J_d = \int_0^{r_{200}} V_c(r) r \Sigma(r) 2\pi R \mathrm{d}r = M_d r_d V_{200} \int_0^{r_{200}/r_d} \mathrm{e}^{-u} u^2 \frac{V_c(r_d u)}{V_{200}} \mathrm{d}u \tag{C.29}$$

$$r_{\mathrm{d}} = \frac{1}{\sqrt{2}} \left(\frac{j_{\mathrm{d}}}{m_{\mathrm{d}}}\right) \lambda r_{\mathrm{h}} f_{\mathrm{c}}^{-1/2} f_{\mathrm{R}}(\lambda, c, m_{\mathrm{d}}, j_{\mathrm{d}}) \tag{C.30}$$

where

$$f_R(\lambda, c, m_d, j_d) = 2\left[\int_0^{\infty} \mathrm{e}^{-u} u^2 \frac{V_c(r_d u)}{V_{200}} \mathrm{d}u\right]^{-1} \tag{C.31}$$

## C.4 Collapse Time for a Molecular Cloud

We assume that the molecular cloud has constant density $\rho_0$. Initially, the sphere is at rest and has radius of $r_0$. During the collapsing, we also assume that the cloud does not suffer from the pressure from inside, thus

$$\frac{\mathrm{d}^2 r}{\mathrm{d}t^2} = -\frac{GM}{r^2}, \tag{C.32}$$

where $M = \frac{4\pi\rho_0 r_0^3}{3}$, since the total mass of the cloud is covserved. Then the above equation gives us

$$\frac{\mathrm{d}^2 r}{\mathrm{d}t^2} = -\frac{4\pi G\rho_0 r_0^3}{r^2}. \tag{C.33}$$

As from some mathmatical trick, we know that

$$\frac{\mathrm{d}}{\mathrm{d}t}\left[\left(\frac{\mathrm{d}r}{\mathrm{d}t}\right)^2\right] = 2\frac{\mathrm{d}r}{\mathrm{d}t}\frac{\mathrm{d}^2 r}{\mathrm{d}t^2} \tag{C.34}$$

After plugging it back into Eq. (C.33), we obtain

$$2\frac{\mathrm{d}r}{\mathrm{d}t}\frac{\mathrm{d}^2 r}{\mathrm{d}t^2} = -\frac{\mathrm{d}r}{\mathrm{d}t}\frac{8\pi G\rho_0 r_0^3}{3r^2}. \tag{C.35}$$

Then, we integrate both sides by $\mathrm{d}t$ and get

$$\left(\frac{\mathrm{d}r}{\mathrm{d}t}\right)^2\Bigg|_{r_0}^{r} = \frac{8\pi G\rho_0 r_0^3}{3}\frac{1}{r}\Bigg|_{r_0}^{r} \tag{C.36}$$

which is

$$\frac{\mathrm{d}(r/r_0)}{\mathrm{d}t} = -\left(\frac{8\pi G\rho_0}{3}\right)^{1/2}\left(\frac{r_0}{r}-1\right)^{1/2} \tag{C.37}$$

Let us set $r/r_0 = \cos^2\beta$, thus the above equation can be rewritten as

$$2\cos\beta\sin\beta\frac{\mathrm{d}\beta}{\mathrm{d}t} = \left(\frac{8\pi G\rho_0}{3}\right)^{1/2}\frac{\sin\beta}{\cos\beta} \tag{C.38}$$

Integrating the above equation from t=0 to $t_{\mathrm{ff}}$, which coresponds to $\beta = 0$ to $\pi/2$

$$\beta + \frac{1}{2}\sin(2\beta)\Bigg|_0^{\pi/2} = \left(\frac{8\pi G\rho_0}{3}\right)^{1/2} t\Bigg|_0^{t_{\mathrm{ff}}} \tag{C.39}$$

Thus, we get the solution:

$$t_{\mathrm{ff}} = \left(\frac{3\pi}{32G\rho_0}\right)^{1/2} \tag{C.40}$$

# Appendix D

# Roche Lobe Radius of Satellite Galaxy

## D.1 Ellipse in Polar Coordinates

Let's assume that $F_1$ is at the origin and $F_2$ is on the positive axis at the point $(2c, 0)$. Then $r$ is the polar vector to the point $P$.

$$|PF_1| + |PF_2| = 2a$$

$$|r| + |r - 2ci| = 2a$$

$$(r - 2a)^2 = (r\cos\theta - 2c)^2 + (r\sin\theta)^2$$

$$r^2 - 4ar + 4a^2 = r^2\cos^2\theta - 4rc\cos\theta + 4c^2 + r^2\sin^2\theta$$

$$-ar + rc\cos\theta = -a^2 + c^2$$

$$r = \frac{a^2 - c^2}{a - c\cos\theta} = \frac{a(1 - e^2)}{1 - e\cos\theta}, \quad e = \frac{c}{a}$$

or

$$\frac{1}{r} = \frac{1}{a}\frac{1 - e\cos\theta}{1 - e^2} \tag{D.1}$$

$$\theta = 0, R_a = a(1+e), \quad \text{apogalacticon},$$
$$\theta = \pi, R_p = a(1-e), \quad \text{prigalacticon}.$$

## D.2 Equation of Orbit

Energy and angular momentum are conserved under the central force,

$$E = \frac{1}{2}m\dot{R}^2 + \frac{l^2}{2mR^2} - \frac{k}{R}, \quad k = GMm$$
$$l = mR^2\frac{\mathrm{d}\theta}{\mathrm{d}t}, \quad \mathrm{d}t = \frac{mR^2}{l}\mathrm{d}\theta$$

Thus we can get

$$\frac{\mathrm{d}R}{\mathrm{d}t} = \left[\frac{2}{m}\left(E + \frac{k}{R} - \frac{l^2}{2mR^2}\right)\right]^{1/2}$$
$$\mathrm{d}\theta = \frac{l}{mR^2}\frac{\mathrm{d}R}{\left[\frac{2}{m}\left(E + \frac{k}{R} - \frac{l^2}{2mR^2}\right)\right]^{1/2}}$$

Integrate on both sides, we obtain

$$\theta = \theta_0 + \int_{R_0}^{R} \frac{\mathrm{d}R}{R^2\left[\frac{2mE}{l^2} + \frac{2mk}{l^2R} - \frac{1}{R^2}\right]^{1/2}}$$

Now let's define $u = 1/R$, thus $\mathrm{d}R = -R^2\mathrm{d}u$,

$$\theta = \theta_0 - \int_{u_0}^{u} \frac{\mathrm{d}u}{\left(\frac{2mE}{l^2} + \frac{2mk}{l^2}u - u^2\right)^{1/2}}$$

Let's define the denominator in the integral as $I^{1/2}$, thus

$$I = \frac{2mE}{l^2} + \frac{2mk}{l^2}u - u^2$$
$$= -(u - \frac{mk}{l^2})^2 + \frac{m^2k^2}{l^4} + \frac{2mE}{l^2}$$
$$= \alpha^2\left[1 - \frac{(u - mk/l^2)^2}{\alpha^2}\right], \quad \alpha^2 = \frac{m^2k^2}{l^4} + \frac{2mE}{l^2}$$

We set $\cos t = \frac{u-mk/l^2}{\alpha}$, $\mathrm{d}u = -\alpha \sin\theta \mathrm{d}t$, thus $I = \alpha^2 \sin^2 t$,

$$\theta = \theta_0 + arccos\left(\frac{u - mk/l^2}{\alpha}\right)$$
$$\cos(\theta - \theta_0) = \frac{u - mk/l^2}{\alpha}$$
$$\frac{1}{R} = \frac{mk}{l^2}\left[1 + \frac{\alpha}{mk/l^2}\cos(\theta - \theta_0)\right]$$

We define $e = \frac{\alpha}{mk/l^2}$, thus

$$a(1-e^2) = \frac{l^2}{mk}, \quad e^2 = \frac{\alpha^2}{m^2k^2/l^4} = 1 + \frac{2El^2}{mk^2}$$

which gives,

$$e = \sqrt{1 + \frac{2El^2}{mk^2}}, \quad a = -\frac{k}{2E} \tag{D.2}$$

## D.3 Roch Lobe Radius

$R$ is the distance of the cluster from the galactic center, and $m$ is the mass of the cluster. The acceleration of the cluster with respect to the galactic center is

$$\frac{\mathrm{d}^2R}{\mathrm{d}^2t} = R\omega^2 - \frac{\mathrm{d}V}{\mathrm{d}R}, \tag{D.3}$$

The acceleration of the star at the same moment is

$$\frac{\mathrm{d}^2R_s}{\mathrm{d}^2t} = R_s\omega^2 - \left(\frac{\mathrm{d}V}{\mathrm{d}R}\right)_{R_s} - \frac{Gm(R_s - R)}{|R_s - R|^3},$$
$$\frac{\mathrm{d}^2(R_s - R)}{\mathrm{d}^2t} = (R_s - R)\omega^2 - \left(\frac{\mathrm{d}V}{\mathrm{d}R}\right)_{R_s} + \left(\frac{\mathrm{d}V}{\mathrm{d}R}\right)_{R} - \frac{Gm(R_s - R)}{|R_s - R|^3}$$
$$\simeq \left(\omega^2 - \frac{\mathrm{d}^2V}{\mathrm{d}^2R} - \frac{Gm}{|R_s - R|^3}\right)(R_s - R)$$

the RHS is the roche lobe radius of this system. It reaches zero when

$$r_{RS}^3 = (R_s - R)^3 = \frac{Gm}{\omega^2 - \mathrm{d}^2V/\mathrm{d}^2R}. \tag{D.4}$$

We use $M$ to represent the gas mass of the galaxy, thus

$$\frac{\mathrm{d}^2V}{\mathrm{d}^2R} = -\frac{2GM}{R^3} \tag{D.5}$$

The cluster's orbit about the galactic center will be an ellipse, with the angular velocity at any point can be obtained from the followings. The 2nd Kepler's Law, or the conservation of angular momentum gives

$$l = mR^2\omega \tag{D.6}$$

And the energy $E$ is also conserved,

$$E = \frac{1}{2}m\dot{R}^2 + \frac{l^2}{2mR^2} - \frac{k}{R}, \quad k = GMm. \tag{D.7}$$

The semimajor axis is one-half the sum of the two apsidal distances $R_1$ and $R_2$. By definition, the radial velocity is zero at these points, and the conservation of energy implies that the apsidal distances are therefore the roots of the equation

$$E - \frac{l^2}{2mR^2} + \frac{k}{R} = 0 \tag{D.8}$$

$$a = \frac{R_1 + R_2}{2} = -\frac{k}{2E} \tag{D.9}$$

The eccentricity of the orbit can be represented as

$$e = \sqrt{1 + \frac{2El^2}{mk^2}} = \sqrt{1 - \frac{l^2}{mka}}$$

$$\frac{l^2}{mk} = a(1 - e^2)$$
$$\frac{m^2R^4\omega^2}{mk} = a(1 - e^2), \quad k = GMm$$
$$\omega^2 = \frac{GMa(1 - e^2)}{R^4}$$

Using this result in Eq. (2), then we get the roche lobe radius at perigalacticon $R_p = (1 - e)a$ and apogalacticon $R_a = (1 + e)a$, respectively.

$$r_{RS}(R_p) = R_p\left[\frac{m}{M(3 + e)}\right]^{1/3}, \quad r_{RS}(R_a) = R_p\left[\frac{m}{M(3 - e)}\right]^{1/3}. \tag{D.10}$$